Doctoral Dissertation (Shinshu University)

Dynamics of magnetic skyrmions in nanostructures and their applications

（ナノ構造中の磁気スキルミオン及びその応用）

September 2018

Xichao Zhang

This dissertation is dedicated to my fiancée, Jing,
and to my parents for their endless love and support

ABSTRACT

The information storage and processing are fundamental and essential to all information and communications technologies, which are also indispensable to our fast-paced information-driven modern society. The revolution of information storage and processing is usually associated with the discovery and development of new information carriers and media. Recently, skyrmions in magnetic materials with chiral or competing exchange interactions are found to be promising building blocks for next-generation information storage and processing applications, such as advanced magnetic memories and novel spintronic computing devices. The magnetic skyrmions are quasiparticle-like nanoscale magnetic spin configurations, which have several promising properties including the topologically non-trivial structure, unique topology-dependent dynamics, reasonably good stability and mobility, and low energy consumption. The understanding of dynamic behaviors of magnetic skyrmions is important and necessary for developing practical information-related applications based on magnetic skyrmions.

In this dissertation, we theoretically and numerically study the dynamics of magnetic skyrmions in confined nanostructures driven by spin-polarized currents or spin waves, as well as the possible advanced applications based on the manipulation of magnetic skyrmions, mainly in the framework of micromagnetics. The dissertation can be divided into three major parts as described below.

In the first part, we focus on the motion dynamics of an isolated magnetic skyrmion driven by spin-polarized currents in both thin films, monolayer and multilayer nanotracks. Both the Slonczewski-like and Zhang-Li spin-transfer torques are considered as the driving forces. We study the magnetic skyrmion-hosting material systems with either chiral exchange interactions or frustrated exchange interactions. The chiral exchange interactions considered are the interface-induced Dzyaloshinskii-Moriya interactions. The frustrated exchange interactions considered are the ferromagnetic nearest and antiferromagnetic

next-nearest Heisenberg exchange interactions. This work shows that the current-induced dynamics of an isolated magnetic skyrmion depends on both the geometric and material properties of skyrmion-hosting nanostructures. We also show that the Slonczewski-like spin-transfer torques are more efficient than the Zhang-Li spin transfer torques for driving the skyrmion motion.

Besides, we reveal that the magnetic skyrmions driven by spin-polarized currents in conventional ferromagnetic materials may show the skyrmion Hall effect due to their special topological structures, namely, the magnetic skyrmions move at an angle with respect to the driving force direction. We demonstrate that the skyrmion Hall effect can either be controlled by locally modifying the magnetic parameters or totally eliminated by fabricating the synthetic antiferromagnetic nanotracks. Especially, the perfect elimination of the skyrmion Hall effect is found to be beneficial for the high-speed transport of information-carrying magnetic skyrmions in narrow channels. Moreover, we reveal that the magnetic skyrmions driven by spin-polarized currents in frustrated ferromagnetic films show novel dynamic behaviors, which can drastically change from the translational motion to the circular motion by triggering the helicity locking-unlocking transition. Namely, the skyrmion helicity is found to be coupled to the center-of-mass skyrmion dynamics, which is a unique property for the magnetic skyrmions in the frustrated magnetic system.

In the second part, we focus on the motion dynamics of an isolated magnetic skyrmion driven by spin waves in both thin films and confined nanostructures with different damping coefficients, where the excited spin waves are propagating either in the longitudinal or transverse direction. This work demonstrates the feasibility and method to drive magnetic skyrmions in complex nanostructures, such as L-corners, T-junctions, and Y-junctions, which are important components for building future spintronic circuits. By investigating the skyrmion velocity versus driving force relation in nanotracks, we reveal that there are different scenarios of the skyrmion dynamics driven by transverse spin waves. At low driving force, the magnetic skyrmion smoothly moves along the nanotrack and does not suffer any significant deformations. At large driving force, the internal modes of the magnetic skyrmion can be excited, resulting in the emission of spin waves by the magnetic skyrmion itself. The magnetic skyrmion may also be destroyed at large driving force. We also reveal that the transverse driving scheme is more efficient than the longitudinal driving scheme for controlling and delivering magnetic skyrmions in narrow

channels due to the damping of spin waves. We further show that motion direction of an isolated magnetic skyrmion in complex nanostructures can be controlled by multiple spin wave sources placed at different positions.

In the third part, we numerically demonstrate that the magnetic skyrmions can be used as the information carriers in a number of advanced spintronic applications, which include the racetrack-type memories, logic computing gates, and transistor-like functional devices. We first point out possible skyrmion candidates for carrying information in different magnetic material systems. We show that the merging of two isolated magnetic skyrmions as well as the duplication of an isolated magnetic skyrmion can be flexibly realized by utilizing the current-driven skyrmion-domain wall conversion mechanism in a Y-junction. We demonstrate that basic binary logic computing operations can be implemented based on the merging and duplication of magnetic skyrmions. In addition, we show that the transport of magnetic skyrmions in narrow channels can be controlled by voltage gates, which can be used for building transistor-like functional devices. This work not only provides guidelines for designing novel electronic and spintronic devices based on magnetic skyrmions, but also highlights the importance of magnetic skyrmions in practical and industrial applications.

Finally, at the end of the dissertation, we point out future research directions on magnetic skyrmions in terms of skyrmion-hosting materials, skyrmion structures, and skyrmion driving forces. We suggest the exploration of magnetic skyrmions and antiskyrmions in antiferromagnetic and ferrimagnetic materials driven by spin-polarized currents, spin waves, and electric fields.

ACKNOWLEDGMENTS

During my PhD study in Japan and China, I think I was helped and supported by many people in a number of ways. Here I would like to thank all of them, although it is hard to express all my thanks in words.

First, I would like to sincerely thank my supervisor Prof. Xiaoxi Liu for giving me the opportunity to perform my research in his group at Nagano. When I was a bachelor student several years ago, I read Prof. Liu's papers on TbFeCo and contacted him as I was very interested in those results. Since that time, Prof. Liu always patiently provide me with very useful guidance on my research and career. I am feeling so lucky to meet him and finally join his group as a PhD student, where I also made some new friends; most are Prof. Liu's students. I have learned a lot from Prof. Liu during these years, both personally and professionally.

I would also like to sincerely thank my co-supervisor Prof. Yan Zhou for his valuable and inspiring advice, guidance and support on my research. Prof. Zhou is a passionate researcher as well as an energetic team leader. He supervised me on a number of projects and all of which lead to remarkable outcomes. For me, Prof. Zhou is a good friend as well. He introduced me to many domestic and international colleagues working in the field of spintronics, and helped me to get familiar with the community quickly.

I am very grateful to Prof. Motohiko Ezawa for insightful discussions and, especially, for giving me many valuable knowledge beyond my own research topics. Prof. Ezawa is the most productive researcher I have ever met. We have collaborated on many works and we are happy to see our research outputs are really significant and making an impact in the field. Without Prof. Ezawa's theoretical contributions and guidance, it would be impossible for me to obtain these achievements.

Special thanks also give to my first academic mentor Prof. G. P. Zhao for introducing me to the beautiful and mysterious world of magnetism. Prof. Zhao taught me some fundamental theories of magnetism and magnetic materials. Even when I was a freshman, he gave me the opportunity and confidence to work with his friendly graduate students: Dr. Guanfeng Zhang, Mr. Hong Tang, Dr. Xiaoyong Wang.

I would like to express many thanks to my awesome collaborators for their tremendous support and their contributions to my PhD study. Especially, I enjoyed the collaboration with Prof. Yongbing Xu and Mr. Junlin Wang on the study of magnetic domain walls; the collaboration with Prof. Weisheng Zhao and the Beihang team Dr. Wang Kang, Dr. Na Lei, Dr. Xueying Zhang, Mr. Yangqi Huang, Ms. Sai Li, Ms. Chengtian Zheng, Mr. Daoqian Zhu, Ms. Xing Chen, Mr. Zhi Li on the skyrmion-based applications; the collaboration with Prof. Wanjun Jiang and the Argonne team Dr. Axel Hoffmann, Dr. Suzanne G. E. te Velthuis, Dr. Olle Heinonen on the experimental observation of the skyrmion Hall effect; the collaboration with Prof. Yaowen Liu and Dr. Dun Xiao on the spin wave-driven skyrmions; the collaboration with Prof. Zhaosen Liu on the magnetic vortices; the collaboration with Prof. Hans Fangohr on the skyrmion-based racetrack memory; the collaboration with Dr. Seonghoon Woo on the ferrimagnetic skyrmion dynamics; the collaboration with Dr. Markus Garst and Dr. Jan Müller on the magnon-driven skyrmions; and the collaboration with Prof. C. I. L. de Araujo and Dr. Renan Loreto on the magnetic skyrmions.

I would also like to express special thanks to my professors and colleagues in Prof. Xiaoxi Liu's group: Prof. Akimitsu Morisako, Mr. Chuang Ma, Mr. Yusei Yamada; as well as my colleagues in Prof. Yan Zhou's group: Dr. Daowei Wang, Dr. Xiangjun Xing, Dr. Yan Liu, Dr. Xu Li, Dr. Siu Kong Koo, Dr. Yongze Cao, Dr. Li Li, Dr. Xiaoguang Li, Mr. Hilary Mak, Mr. Hong Xia, Mr. C. P. Chui, and Ms. Jing Xia.

I appreciate all the fruitful face-to-face or email discussions with Dr. Chaoliang Zhang, Dr. Fusheng Ma, Dr. Guoqiang Yu, Dr. Haifeng Du, Dr. Han Zhang, Dr. Hans Benjamin Braun, Dr. Huaiyang Yuan, Dr. Indra Purnama, Dr. Jianbo Wang, Dr. Junichi Iwasaki, Dr. Marijan Beg, Dr. Ming Yue, Dr. Minghua Guo, Dr. Oleg Tretiakov, Dr. Pen Yan, Dr. Qi Wang, Dr. Qingfang Liu, Dr. S. N. Piramanayagam, Ms. Shasha Wang, Dr. Shengyuan Yang, Dr. Shizeng Lin, Dr. Teruo Ono, Dr. Wei Zhang, Dr. Weiwei Wang, Dr. Wenhong Wang, Dr. Xiansi Wang, Dr. Yan Liu, Ms. Yi Peng, Dr. Zhe Yuan, Dr. Zhipeng Hou, and Dr. Zidong Wang.

Last but not least, I would like to give my deepest and most heartfelt thanks to my parents Yi and Hong, and to my fiancée Jing. I usually blame myself for being far away from my parents during these years. No matter where I go, their love for me is always deeper than the ocean. I dedicate this dissertation to them.

My PhD study was financially supported by the Japan Society for the Promotion of Science (JSPS).

LIST OF SELECTED PUBLICATIONS

1. **X. Zhang**, J. Xia, Y. Zhou, X. Liu, H. Zhang, and M. Ezawa, "Skyrmion dynamics in a frustrated ferromagnetic film and current-induced helicity locking-unlocking transition", *Nature Communications* **8**, 1717 (2017).
2. **X. Zhang**, J. Xia, G. P. Zhao, X. Liu, and Y. Zhou, "Magnetic skyrmion transport in a nanotrack with spatially varying damping and non-adiab atic torque", *IEEE Transactions on Magnetics* **53**(3), 1500206 (2017).
3. **X. Zhang**, J. Xia, Y. Zhou, D. Wang, X. Liu, W. Zhao, and M. Ezawa, "Control and manipulation of a magnetic skyrmionium in nanostructures", *Physical Review B* **94**, 094420 (2016).
4. **X. Zhang**, M. Ezawa, and Y. Zhou, "Thermally stable magnetic skyrmions in multilayer synthetic antiferromagnetic racetracks", *Physical Review B* **94**, 064406 (2016).
5. **X. Zhang**, Y. Zhou, and M. Ezawa, "High-topological-number skyrmion and topologically protected dissipative structure", *Physical Review B* **93**, 024415 (2016).
6. **X. Zhang**, Y. Zhou, and M. Ezawa, "Magnetic bilayer-skyrmions without skyrmion Hall effect", *Nature Communications* **7**, 10293 (2016).
7. **X. Zhang**, Y. Zhou, and M. Ezawa, "Antiferromagnetic skyrmion: stability, creation and manipulation", *Scientific Reports* **6**, 24795 (2016).
8. **X. Zhang**, Y. Zhou, M. Ezawa, G. P. Zhao, and W. Zhao, "Magnetic skyrmion transistor: skyrmion motion in a voltage-gated nanotrack", *Scientific Reports* **5**, 11369 (2015).
9. **X. Zhang**, M. Ezawa, and Y. Zhou, "Magnetic skyrmion logic gates: conversion, duplication and merging of skyrmions", *Scientific Reports* **5**, 9400 (2015).
10. **X. Zhang**, M. Ezawa, D. Xiao, G. P. Zhao, Y. Liu, and Y. Zhou, "All-magnetic control of skyrmions in nanowires by a spin wave", *Nanotechnology* **26**, 225701 (2015).

CONTENTS

LIST OF FIGURES

LIST OF TABLES

CHAPTER 1

Introduction

In this chapter, we introduce the basics of the magnetic skyrmion and its importance in topological magnetism and spintronic applications. We then outline the structure of this dissertation and briefly summarize the contributions of each chapter.

1.1 Background and motivation

Magnetism is an old field of study, which has been studied for over two thousand years [1]. However, the magnetism continues to face new challenges as it plays an essential role in our industrial production and daily life. The most important and intriguing aspect of magnetism is its application in the information storage. The information storage is fundamental to all information and communications technologies, which is also indispensable to the establishment of the advanced information-driven society. Therefore, for the purpose of realizing the high-performance magnetic information storage and processing applications, it is becoming more and more important to study magnetic phenomena that can be utilized to store information and perform computing.

Traditional researches on magnetism related to the information storage and processing have been focused on the manipulation of magnetization and magnetic spin textures at nanoscale. Recently, due to the significant advancements in the thin-film growth and deposition, nanostructure fabrication, and high-resolution microscopy technologies, the focus on magnetism research has been shifted to a new cross area of magnetism and topology, which is called the *topological magnetism* or *chiral magnetism*. For example, the broken inversion symmetry in a magnetic multilayer nanostructure with strong spin-orbit couplings gives rise to the interfacial asymmetric exchange interaction, i.e., the Dzyaloshinskii-Moriya interaction (DMI) [2, 3], which can stabilize topological spin textures [4, 5, 6, 7, 8].

Topological spin textures can be used to carry digital information. However, the physics behind the statics and dynamics of topological spin textures still remains elusive, which

must be investigated and understood in order to build novel magnetic and spintronic devices based on the manipulation of topological spin textures. A key subject in the study of topological magnetism and topological spin textures is the *magnetic skyrmion* [4, 5, 7, 6, 8].

The concept of skyrmion was firstly proposed by British nuclear physicist Tony Skyrme to describe the interactions of pions in the context of nuclear physics [9]. Later, it is generalized to various subjects in condensed matter physics including quantum Hall magnets [10], Bose-Einstein condensate [11], and so on. A skyrmion is a topological quasiparticle-like excitation in classical continuum field theory, which is robust as long as the field is continuous and the edge effect is negligible. Topological considerations are of considerable use in describing and understanding the extraordinary topological stability of a skyrmion. The topological stability is the fact that a significant amount of energy is required in order to transform a certain object into another with different topology [12]. For example, both a coffee mug and a donut can be deformed into a torus by a continuous and invertible mapping, indicating the same nature of topology for the coffee mug and donut, i.e., they are homeomorphic [13]. On the contrary, a coffee mug (or a donut) cannot morph into a sphere without introducing rupture, because that they are of different topology. In a similar way, the magnetic skyrmion cannot be continuously transformed into other magnetic textures such as the ferromagnetic (FM) state, without surpassing the topological energy barrier. Therefore, the magnetic skyrmion is topologically protected and relatively more stable than other types of magnetic textures such as the magnetic vortex and magnetic bubble, making it very promising for realistic applications in the information processing and ultra-high density information storage [14, 15].

In the context of magnetism, the magnetic skyrmion is a quasiparticle-like nanometer-scale magnetic domain wall structure of which the spin configuration is swirling in the planar space and would wrap a unit three-dimensional (3D) spherical surface with spins pointing in all directions in the compactification of the planar space [16]. The magnetic skyrmion was first theoretically predicted to exist in magnetic metals [5, 17] and magnetic thin films [4] having the asymmetric exchange coupling interaction, namely, the DMI [2, 3]. Then, it was first experimentally identified in chiral magnetic materials just after the turn of the twenty-first century [6]. Since then, the magnetic skyrmion has emerged as an active research topic in the fields of magnetism and spintronics, which has also been experimentally observed, created, and manipulated in a wide variety of material systems, including the FM materials [18, 19, 20, 21] and other materials [22, 23, 24]. Experiments also show the manipulation of magnetic skyrmions in different nanostructures, such as the bulk materials [25], magnetic ultra-thin films [26, 27, 28], and magnetic multilayers (heterostructures) [24, 29, 30]. Experiments on magnetic skyrmions are mainly focusing on the

FM materials, for example, most of the experimental observations on magnetic skyrmions are reported in the non-centrosymmetric B20-type ferromagnets, such as MnSi [6, 31], FeGe [32, 33], and FeCoSi [18, 34]. More recently, isolated magnetic skyrmions have also been successfully realized in thin films of similar materials lacking inverse symmetry or with asymmetric interfaces in proximity of non-magnetic heavy-metal substrate with strong spin-orbit interaction inducing sizable DMI [26, 27, 28, 35]. At the same time, numerous theoretical and numerical studies have revealed various potential applications of magnetic skyrmions toward the skyrmion-based electronics as well as the skyrmion-based spintronics, of which the research field is usually referred to as *skyrmionics* [14, 15, 36].

However, although the magnetic skyrmion has many advantages for practical applications, it also comes with some drawbacks. There is a significant obstacle to the transport of magnetic skyrmions in nanostructures, especially in the high-speed operation. The reason is that the magnetic skyrmion experiences the skyrmion Hall effect (SkHE) [37, 38, 35, 39], which means the magnetic skyrmion moves at an angle with respect to the direction of the external driving force. As a consequence, in the high-speed operation, the transverse motion or deflection of a magnetic skyrmion may result in its destruction at the edge of the nanostructure [38, 40, 41], which leads to drastically reduced reliable distance of the skyrmion transport [41]. The SkHE was first predicted theoretically [37] and has recently been observed in two independent room-temperature experiments [35, 39]. On the road to realize the skyrmion-based ultra-dense and ultra-fast information storage and processing devices, the SkHE is generally a detrimental effect because it can result in the undesired loss of the encoded information carried by the magnetic skyrmions [35, 37]. Therefore, a natural and interesting problem is then to find the methods to eliminate or reduce the detrimental SkHE. Theoretical, numerical, and experimental works have proposed several effective methods to eliminate or reduce the detrimental SkHE. For example, one could build a skyrmion transport channel where material parameters are locally modified so that the skyrmion motion can be effectively controlled [42]. An alternative method is to construct the antiferromagnetic (AFM) skyrmion [43, 44], synthetic AFM skyrmion [38], and magnetic skyrmionium [45, 46]. These skyrmion-like structures have the same function of the common magnetic skyrmion, while they are totally immune from the SkHE and thus can perfectly move along the driving force direction. Another challenging problem is the thermal fluctuation as a magnetic skyrmion can be largely deformed and might be easily destroyed by the thermal fluctuation [32, 47, 48, 49]. Hence, the thermal effect is one of the important factors to realize the skyrmion-based room-temperature device applications. Fortunately, recent experimental investigations have demonstrated the increased thermal stability of magnetic skyrmions in magnetic multilayers, which make magnetic skyrmions

more applicable to practical applications [24, 29, 30].

On the other hand, a more important and more fundamental problem in the topological magnetism is to find all useable skyrmion-hosting materials. Apart from conventional FM materials with DMIs, the frustrated magnets with competing exchange interactions serve as a promising candidate to host magnetic skyrmions and other topological spin textures [50, 51, 52]. It has been discovered that the magnetic skyrmions can be stabilized in the triangular spin model with competing interactions [53]. A rich phase diagram of an anisotropic frustrated magnet [54] and dynamic properties of frustrated skyrmions [51, 52] were also reported. More remarkable physics and novel potential applications of magnetic skyrmions in the frustrated magnets need to be studied further and more extensively.

In this dissertation, under the framework of micromagnetics, we mainly study the dynamics of isolated magnetic skyrmions (including several skyrmion-like structures) in confined nanostructures for different material systems, including FM system, synthetic AFM system, and frustrated magnetic system. Some key numerical results are supported by experimental observations. Besides, we focus on the manipulation mechanisms of a single isolated magnetic skyrmion in nanostructures, aiming for the information delivery and computing. In addition, we propose and demonstrate that several possible information storage and logic computing applications can be realized based on the manipulation of magnetic skyrmions.

1.2 Structure of this dissertation

This dissertation focuses on the study of dynamics of magnetic skyrmions in nanostructures driven by different types of external forces, and their future applications in the fields of applied spintronics. Therefore, the remainder of this dissertation is organized as follows.

- Chapter 2 provides a short introduction about the framework of micromagnetics, and briefly reviews fundamental concepts in micromagnetics, including the typical micromagnetic energy terms, spin dynamics equations, spin torques, and spin textures.
- Chapter 3 gives a detailed review on the magnetic skyrmion and presents a numerical and experimental study on the SkHE.
- Chapter 4 focuses on the investigation on the dynamics of isolated magnetic skyrmions driven by Slonczewski-like and Zhang-Li-like spin-transfer torques.
- Chapter 5 presents a study on the dynamics of isolated magnetic skyrmions in thin films, nanotracks, and junctions driven by spin waves.

- Chapter 6 is devoted to the study of possible future applications of magnetic skyrmions, such as racetrack-type memories, logic computing devices, and voltage-gated transistor-like functional devices.
- Chapter 7 summarizes the key findings and major conclusions of this dissertation and discusses the future outlook on magnetic skyrmions in terms of materials, skyrmion structures, and external driving forces.
- Appendix A provides a detailed derivation of the Thiele motion equation, which is used for the analysis of center-of-mass dynamics of rigid isolated magnetic skyrmions.

BIBLIOGRAPHY

[1] J. Coey, and T. N. Mhíocháin, *History of Magnetism* (Elsevier, 2016).

[2] I. Dzyaloshinsky, A thermodynamic theory of "weak" ferromagnetism of antiferromagnetics. J. Phys. Chem. Solids **4**, 241–255 (1958).

[3] T. Moriya, Anisotropic superexchange interaction and weak ferromagnetism. Phys. Rev. **120**, 91–98 (1960).

[4] A. N. Bogdanov, and U. K. Rößler, Chiral symmetry breaking in magnetic thin films and multilayers. Phys. Rev. Lett. **87**, 037203 (2001).

[5] U. K. Rößler, A. N. Bogdanov, and C. Pfleiderer, Spontaneous skyrmion ground states in magnetic metals. Nature **442**, 797–801 (2006).

[6] S. Mühlbauer, B. Binz, F. Jonietz, C. Pfleiderer, A. Rosch, A. Neubauer, R. Georgii, and P. Böni, Skyrmion lattice in a chiral magnet. Science **323**, 915–919 (2009).

[7] B. Dupé, M. Hoffmann, C. Paillard, and S. Heinze, Tailoring magnetic skyrmions in ultra-thin transition metal films. Nat. Commun. **5**, 4030 (2014).

[8] N. Romming, C. Hanneken, M. Menzel, J. E. Bickel, B. Wolter, K. Bergmannvon, A. Kubetzka, and R. Wiesendanger, Writing and deleting single magnetic skyrmions. Science **341**, 636–639 (2013).

[9] T. H. R. Skyrme, A non-linear field theory. Proc. Royal Soc. A **260**, 127–138 (1961).

[10] L. Brey, H. A. Fertig, R. Côté, and A. H. MacDonald, Skyrme crystal in a two-dimensional electron gas. Phys. Rev. Lett. **75**, 2562–2565 (1995).

[11] U. Al Khawaja, and H. Stoof, Skyrmions in a ferromagnetic Bose-Einstein condensate. Nature **411**, 918 (2001).

[12] H.-B. Braun, Topological effects in nanomagnetism: from superparamagnetism to chiral quantum solitons. Adv. Phys. **61**, 1–116 (2012).

[13] J. E. Moore, The birth of topological insulators. Nature **464**, 194 (2010).

[14] A. Fert, V. Cros, and J. Sampaio, Skyrmions on the track. Nat. Nanotechnol. **8**, 152–156 (2013).

[15] N. Nagaosa, and Y. Tokura, Topological properties and dynamics of magnetic skyrmions. Nat. Nanotechnol. **8**, 899–911 (2013).

[16] K. Everschor-Sitte, and M. Sitte, Real-space Berry phases: Skyrmion soccer (invited). J. Appl. Phys. **115**, 172602 (2014).

[17] A. Bogdanov, and A. Hubert, Thermodynamically stable magnetic vortex states in magnetic crystals. J. Magn. Magn. Mater. **138**, 255–269 (1994).

[18] X. Z. Yu, Y. Onose, N. Kanazawa, J. H. Park, J. H. Han, Y. Matsui, N. Nagaosa, and Y. Tokura, Real-space observation of a two-dimensional skyrmion crystal. Nature **465**, 901–904 (2010).

[19] S. Heinze, K. Bergmannvon, M. Menzel, J. Brede, A. Kubetzka, R. Wiesendanger, G. Bihlmayer, and S. Blugel, Spontaneous atomic-scale magnetic skyrmion lattice in two dimensions. Nat. Phys. **7**, 713–718 (2011).

[20] N. Romming, A. Kubetzka, C. Hanneken, K. Bergmannvon, and R. Wiesendanger, Field-dependent size and shape of single magnetic skyrmions. Phys. Rev. Lett. **114**, 177203 (2015).

[21] G. Chen, A. Mascaraque, A. T. N'Diaye, and A. K. Schmid, Room temperature skyrmion ground state stabilized through interlayer exchange coupling. Appl. Phys. Lett. **106**, 242404 (2015).

[22] S. Seki, X. Z. Yu, S. Ishiwata, and Y. Tokura, Observation of skyrmions in a multiferroic material. Science **336**, 198-201 (2012).

[23] Y. Nahas, S. Prokhorenko, L. Louis, Z. Gui, I. Kornev, and L. Bellaiche, Discovery of stable skyrmionic state in ferroelectric nanocomposites. Nat. Commun. **6**, 8542 (2015).

[24] B. Dupé, G. Bihlmayer, M. Böttcher, S. Blügel, and S. Heinze, Engineering skyrmions in transition-metal multilayers for spintronics. Nat. Commun. **7**, 11779 (2016).

[25] F. Jonietz, S. Mühlbauer, C. Pfleiderer, A. Neubauer, W. Münzer, A. Bauer, T. Adams, R. Georgii, P. Böni, R. A. Duine, K. Everschor, M. Garst, and A. Rosch, Spin transfer torques in MnSi at ultralow current densities. Science **330**, 1648–1651 (2010).

[26] W. Jiang, P. Upadhyaya, W. Zhang, G. Yu, M. B. Jungfleisch, F. Y. Fradin, J. E. Pearson, Y. Tserkovnyak, K. L. Wang, O. Heinonen, S. G. E. Velthuiste, and A. Hoffmann, Blowing magnetic skyrmion bubbles. Science **349**, 283–286 (2015).

[27] O. Boulle, J. Vogel, H. Yang, S. Pizzini, D. Souza Chavesde, A. Locatelli, T. O. Mentes, A. Sala, L. D. Buda-Prejbeanu, O. Klein, M. Belmeguenai, Y. Roussigne, A. Stashkevich, S. M. Cherif, L. Aballe, M. Foerster, M. Chshiev, S. Auffret, I. M. Miron, and G. Gaudin, Room-temperature chiral magnetic skyrmions in ultrathin magnetic nanostructures. Nat. Nanotechnol. **11**, 449–454 (2016).

[28] S. Woo, K. Litzius, B. Kruger, M.-Y. Im, L. Caretta, K. Richter, M. Mann, A. Krone, R. M. Reeve, M. Weigand, P. Agrawal, I. Lemesh, M.-A. Mawass, P. Fischer, M. Klaui, and G. S. D. Beach, Observation of room-temperature magnetic skyrmions and their current-driven dynamics in ultrathin metallic ferromagnets. Nat. Mater. **15**, 501–506 (2016).

[29] C. Moreau-Luchaire, C. Moutafis, N. Reyren, J. Sampaio, C. A. F. Vaz, N. Van Horne, K. Bouzehouane, K. Garcia, C. Deranlot, P. Warnicke, P. Wohlhüter, J.-M. George, M. Weigand, J. Raabe, V. Cros, and A. Fert, Additive interfacial chiral interaction in multilayers for stabilization of small individual skyrmions at room temperature. Nat. Nanotechnol. **11**, 444–448 (2016).

[30] A. Soumyanarayanan, M. Raju, A. L. Gonzalez Oyarce, A. K. C. Tan, M.-Y. Im, A. P. Petrović, P. Ho, K. H. Khoo, M. Tran, C. K. Gan, F. Ernult, and C. Panagopoulos, Tunable room-temperature magnetic skyrmions in Ir/Fe/Co/Pt multilayers. Nat. Mater. **16**, 898 (2017).

[31] H. Du, J. P. DeGrave, F. Xue, D. Liang, W. Ning, J. Yang, M. Tian, Y. Zhang, and S. Jin, Highly stable skyrmion state in helimagnetic MnSi nanowires. Nano Lett. **14**, 2026-2032 (2014).

[32] X. Z. Yu, N. Kanazawa, Y. Onose, K. Kimoto, W. Z. Zhang, S. Ishiwata, Y. Matsui, and Y. Tokura, Near room-temperature formation of a skyrmion crystal in thin-films of the helimagnet FeGe. Nat. Mater. **10**, 106–109 (2011).

[33] T. Matsumoto, Y.-G. So, Y. Kohno, H. Sawada, Y. Ikuhara, and N. Shibata, Direct observation of $\Sigma 7$ domain boundary core structure in magnetic skyrmion lattice. Sci. Adv. **2**, e1501280 (2016).

[34] W. Münzer, A. Neubauer, T. Adams, S. Mühlbauer, C. Franz, F. Jonietz, R. Georgii, P. Böni, B. Pedersen, M. Schmidt, A. Rosch, and C. Pfleiderer, Skyrmion lattice in the doped semiconductor $Fe_{1-x}Co_xSi$. Phys. Rev. B **81**, 041203 (2010).

[35] W. Jiang, X. Zhang, G. Yu, W. Zhang, X. Wang, M. Benjamin Jungfleisch, J. E. Pearson, X. Cheng, O. Heinonen, K. L. Wang, Y. Zhou, A. Hoffmann, and S. G. E. Velthuiste, Direct observation of the skyrmion Hall effect. Nat. Phys. **13**, 162–169 (2017).

[36] R. Wiesendanger, Nanoscale magnetic skyrmions in metallic films and multilayers: a new twist for spintronics. Nat. Rev. Mater. **1**, 16044 (2016).

[37] J. Zang, M. Mostovoy, J. H. Han, and N. Nagaosa, Dynamics of skyrmion crystals in metallic thin films. Phys. Rev. Lett. **107**, 136804 (2011).

[38] X. Zhang, Y. Zhou, and M. Ezawa, Magnetic bilayer-skyrmions without skyrmion Hall effect. Nat. Commun. **7**, 10293 (2016).

[39] K. Litzius, I. Lemesh, B. Kruger, P. Bassirian, L. Caretta, K. Richter, F. Buttner, K. Sato, O. A. Tretiakov, J. Forster, R. M. Reeve, M. Weigand, I. Bykova, H. Stoll, G. Schutz, G. S. D. Beach, and M. Klaui, Skyrmion Hall effect revealed by direct time-resolved X-ray microscopy. Nat. Phys. **13**, 170–175 (2017).

[40] I. Purnama, W. L. Gan, D. W. Wong, and W. S. Lew, Guided current-induced skyrmion motion in 1D potential well. Sci. Rep. **5**, 10620 (2015).

[41] X. Zhang, G. P. Zhao, H. Fangohr, J. P. Liu, W. X. Xia, J. Xia, and F. J. Morvan, Skyrmion-skyrmion and skyrmion-edge repulsions in skyrmion-based racetrack memory. Sci. Rep. **5**, 7643 (2015).

[42] X. Zhang, J. Xia, G. P. Zhao, X. Liu, and Y. Zhou, Magnetic skyrmion transport in a nanotrack with spatially varying damping and non-adiabatic torque. IEEE Trans. Magn. **53**, 1-6 (2017).

[43] J. Barker, and O. A. Tretiakov, Static and dynamical properties of antiferromagnetic skyrmions in the presence of applied current and temperature. Phys. Rev. Lett. **116**, 147203 (2016).

[44] X. Zhang, Y. Zhou, and M. Ezawa, Antiferromagnetic skyrmion: stability, creation and manipulation. Sci. Rep. **6**, 24795 (2016).

[45] A. Bogdanov, and A. Hubert, The stability of vortex-like structures in uniaxial ferromagnets. J. Magn. Magn. Mater. **195**, 182–192 (1999).

[46] X. Zhang, J. Xia, Y. Zhou, D. Wang, X. Liu, W. Zhao, and M. Ezawa, Control and manipulation of a magnetic skyrmionium in nanostructures. Phys. Rev. B **94**, 094420 (2016).

[47] X. Yu, N. Kanazawa, W. Zhang, T. Nagai, T. Hara, K. Kimoto, Y. Matsui, Y. Onose, and Y. Tokura, Skyrmion flow near room temperature in an ultralow current density. Nat. Commun. **3**, 988 (2012).

[48] T. Schulz, R. Ritz, A. Bauer, M. Halder, M. Wagner, C. Franz, C. Pfleiderer, K. Everschor, M. Garst, and A. Rosch, Emergent electrodynamics of skyrmions in a chiral magnet. Nat. Phys. **8**, 301–304 (2012).

[49] H. Oike, A. Kikkawa, N. Kanazawa, Y. Taguchi, M. Kawasaki, Y. Tokura, and F. Kagawa, Interplay between topological and thermodynamic stability in a metastable magnetic skyrmion lattice. Nat. Phys. **12**, 62–66 (2016).

[50] S.-Z. Lin, and S. Hayami, Ginzburg-Landau theory for skyrmions in inversion-symmetric magnets with competing interactions. Phys. Rev. B **93**, 064430 (2016).

[51] X. Zhang, J. Xia, Y. Zhou, X. Liu, H. Zhang, and M. Ezawa, Skyrmion dynamics in a frustrated ferromagnetic film and current-induced helicity locking-unlocking transition. Nat. Commun. **8**, 1717 (2017).

[52] A. O. Leonov, and M. Mostovoy, Edge states and skyrmion dynamics in nanostripes of frustrated magnets. Nat. Commun. **8**, 14394 (2017).

[53] T. Okubo, S. Chung, and H. Kawamura, Multiple-q states and the skyrmion lattice of the triangular-lattice Heisenberg antiferromagnet under magnetic fields. Phys. Rev. Lett. **108**, 017206 (2012).

[54] A. O. Leonov, and M. Mostovoy, Multiply periodic states and isolated skyrmions in an anisotropic frustrated magnet. Nat. Commun. **6**, 8275 (2015).

CHAPTER 2

Micromagnetics

In this chapter, we introduce the basic theory of micromagnetics. Besides, we briefly introduce and review some fundamental and important concepts related to the study of magnetic skyrmions.

2.1 Magnetization

In classical electromagnetism, the magnetic moment $\boldsymbol{\mu}$ of a current loop is defined as

$$\boldsymbol{\mu} = I \int_A \mathrm{d}\boldsymbol{A}, \tag{2.1}$$

where I is the electric current in the closed loop, A is the area of the closed loop. The direction of the magnetic moment is determined by the direction of the current. The magnetic moment of atoms exists due to the spinning of electrons, and

$$\boldsymbol{\mu} = \gamma \boldsymbol{S}, \tag{2.2}$$

where γ is the gyromagnetic ratio and $\boldsymbol{S}$ is the spin angular momentum of the electron. In the framework of micromagnetics, the magnetization $\boldsymbol{M}$ is defined as the volume density of the magnetic moment

$$\boldsymbol{M} = \frac{\sum \boldsymbol{\mu}_i}{V}. \tag{2.3}$$

It can be seen as the average magnetic moment of several atoms, thus the magnetization can be considered to change continuously in the space. The magnitude of the magnetization $M_\mathrm{S} = |\boldsymbol{M}|$ is constant and called the saturation magnetization.

2.2 Interactions

The interactions among magnetic moments as well as the interactions between magnetic moment and external magnetic field include the Heisenberg exchange interaction, DMI,

magnetic anisotropy interaction, Zeeman interaction, and dipole-dipole interaction (DDI).

2.2.1 Exchange interaction

The exchange interaction is a strong but short-range effect, where only the nearest-neighbor (NN) sites are taken into account usually [1]. According to the Heisenberg exchange model, the energy between neighboring spins, $\boldsymbol{S}_i$ and $\boldsymbol{S}_j$, can be written as

$$\mathcal{H}_{\text{ex}} = -J_{ij} \sum_{\langle i,j \rangle} \boldsymbol{S}_i \cdot \boldsymbol{S}_j, \tag{2.4}$$

where J_{ij} is the exchange integral between $\boldsymbol{S}_i$ and $\boldsymbol{S}_j$. For FM materials, $J_{ij} > 0$, and the energy reaches the minimum when $\boldsymbol{S}_i$ and $\boldsymbol{S}_j$ are aligned in a parallel manner. For AFM materials, $J_{ij} < 0$, and the energy reaches the minimum when $\boldsymbol{S}_i$ and $\boldsymbol{S}_j$ are aligned in an antiparallel manner. In the framework of micromagnetics, the average energy density of the Heisenberg exchange energy can be written as

$$\mathcal{E}_{\text{ex}} = A \left(\nabla \boldsymbol{m}\right)^2, \tag{2.5}$$

where $\boldsymbol{m} = \boldsymbol{M}/M_{\text{S}}$ is the reduced magnetization, and A is the exchange constant.

2.2.2 Dzyaloshinskii-Moriya interaction

The DMI is an antisymmetric exchange interaction, which arises from the spin-orbit coupling [2, 3]. It not only occurs at the interface between a magnetic thin film layer and a heavy-metal layer with strong spin-orbit coupling, but also exists in the bulk materials lacking inversion symmetry.

2.2.2.1 Interface-induced Dzyaloshinskii-Moriya interaction

At the atomic scale, the interface-induced DMI in the ultrathin magnetic film placed on the heavy-metal substrate with strong spin-orbit coupling (belonging to the C_{nv} symmetry group), such as Fe/Ir [4], CoFe/Pt [5], and CoFe/Ta [5] interfaces, is expressed as [6]

$$\mathcal{H}_{\text{iDM}} = d_{\text{iDM}} \sum_{\langle i,j \rangle} (\boldsymbol{u}_{ij} \times \hat{\boldsymbol{z}}) \cdot (\boldsymbol{S}_i \times \boldsymbol{S}_j), \tag{2.6}$$

where $\langle i, j \rangle$ denotes the NN sites, $\boldsymbol{S}_i$ and $\boldsymbol{S}_j$ are the classical spin vectors at sites i and j, respectively. d_{iDM} is the interface-induced DMI coupling energy (of the order of 1 meV), $\boldsymbol{u}_{ij}$ is the unit vector between $\boldsymbol{S}_i$ and $\boldsymbol{S}_j$, and $\hat{\boldsymbol{z}}$ is the normal to the interface. In the

continuous micromagnetic model, the average energy density for interface-induced DMI reads [7, 8]

$$\begin{aligned}\mathcal{E}_{\mathrm{iDM}} &= D_{\mathrm{iDM}}\left[m_z\left(\boldsymbol{m}\cdot\nabla\right)-\left(\nabla\cdot\boldsymbol{m}\right)m_z\right] \\ &= D_{\mathrm{iDM}}\left(m_z\frac{\partial m_x}{\partial x}-m_x\frac{\partial m_z}{\partial x}+m_z\frac{\partial m_y}{\partial y}-m_y\frac{\partial m_z}{\partial y}\right),\end{aligned} \tag{2.7}$$

with D_{iDM} the continuous effective interface-induced DMI constant (in J m^{-2}), b the magnetic film thickness. m_x, m_y and m_z are the Cartesian components of the reduced magnetization $\boldsymbol{m}$. The link between D_{iDM} and d_{iDM} depends on the type of lattice, but scales as $1/ab$ (a and b stand for the lattice constant and the film thickness, respectively). The $1/b$ scaling is due to the assumption of the interface-induced DMI. One obtains $D_{\mathrm{iDM}} = d_{\mathrm{iDM}}/ab = d_{\mathrm{iDM}}/Na^2$ for a simple cubic lattice oriented along the (001) direction and $D_{\mathrm{iDM}} = d_{\mathrm{iDM}}\sqrt{3}/ab = 3d_{\mathrm{iDM}}/Na^2\sqrt{2}$ for a face-centered-cubic lattice oriented along the (111) direction (N is the number of atomic planes in the film).

2.2.2.2 Bulk Dzyaloshinskii-Moriya interaction

At the atomic scale, the bulk DMI in bulk materials lacking inversion symmetry (belonging to the D_{n} symmetry group), for examples, MnSi [9], $Fe_{1-x}Co_xSi$ [10], and FeGe [11]. This interaction is homogeneous and can be expressed as

$$\mathcal{H}_{\mathrm{bDM}} = d_{\mathrm{bDM}}\sum_{\langle i,j\rangle}\boldsymbol{u}_{ij}\cdot(\boldsymbol{S}_i\times\boldsymbol{S}_j), \tag{2.8}$$

where d_{bDM} is the bulk DMI coupling energy. In the continuous micromagnetic model, the average energy density for bulk DMI reads

$$\begin{aligned}\mathcal{E}_{\mathrm{bDM}} &= D_{\mathrm{bDM}}\left[\boldsymbol{m}\cdot\left(\nabla\times\boldsymbol{m}\right)\right] \\ &= D_{\mathrm{bDM}}\left(m_z\frac{\partial m_x}{\partial y}-m_x\frac{\partial m_z}{\partial y}-m_z\frac{\partial m_y}{\partial x}+m_y\frac{\partial m_z}{\partial x}\right),\end{aligned} \tag{2.9}$$

with D_{bDM} the continuous effective bulk DMI constant (in J m^{-2}).

2.2.3 Anisotropy

In magnetic materials, the direction of magnetic moment has one or several preferred axes. These preferred axes are called easy axes. The magnetic anisotropy is defined as the energy costs to turn the magnetization from the direction of easy axis into any other direction. In the framework of micromagnetics, the average energy density of the uniaxial magnetic anisotropy is given by

$$\mathcal{E}_{\mathrm{ani}} = -K(\boldsymbol{m}\cdot\boldsymbol{n})^2, \tag{2.10}$$

where K is the anisotropy constant, and $\boldsymbol{n}$ is the easy axis.

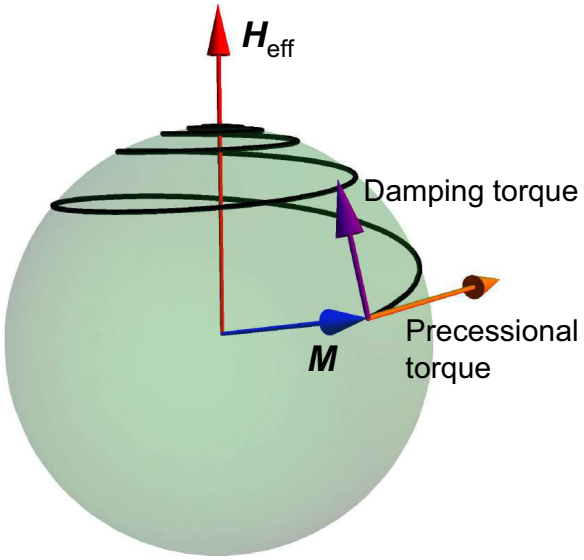

Figure 2.1: Schematic illustration of the LLG equation. The damped precession of the magnetization $\boldsymbol{M}$ under the effective field $\boldsymbol{H}_{\text{eff}}$. The solid black curve denotes the trajectory of the magnetization vector.

2.2.4 Zeeman energy

The Zeeman interaction tends to turn the magnetization to the same direction as the applied magnetic field. In the micromagnetic model, the Zeeman energy density is expressed as

$$\mathcal{E}_{\text{Zeeman}} = -\mu_0(\boldsymbol{M} \cdot \boldsymbol{H}), \tag{2.11}$$

where $\boldsymbol{H}$ is the applied magnetic field and μ_0 is the vacuum permeability constant.

2.2.5 Dipole-dipole interaction

The DDI is a long-range interaction. In FM materials, magnetic dipoles generate the demagnetization field $\boldsymbol{H}_{\text{d}}$, which has the tendency to act on the moment so as to reduce the total magnetic moment. For the continuous model, the average energy density of the DDI can be regarded as the Zeeman energy density of the demagnetization field, given as

$$\mathcal{E}_{\text{DDI}} = -\frac{\mu_0}{2}\boldsymbol{M} \cdot \boldsymbol{H}_{\text{DDI}}. \tag{2.12}$$

where the factor $1/2$ is included to avoid double counting.

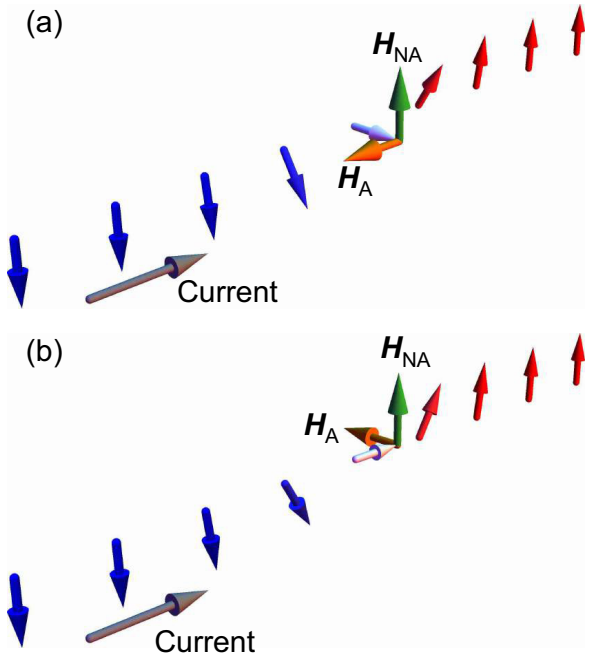

Figure 2.2: Schematic illustration of the effective fields generated by STTs for (a) Bloch-type domain wall and (b) Néel-type domain wall. The orange and green arrows represent the effective fields for adiabatic and non-adiabatic STTs, respectively. The gray arrow indicates the current direction.

2.3 Landau-Lifshitz-Gilbert equation

The Landau-Lifshitz-Gilbert (LLG) equation is an ordinary differential equation describing the precessional motion of magnetization $\boldsymbol{M}$ [12, 13, 14]

$$\frac{\mathrm{d}\boldsymbol{M}}{\mathrm{d}t} = \gamma \boldsymbol{M} \times \boldsymbol{H}_{\mathrm{eff}} + \frac{\alpha}{M_{\mathrm{S}}} \left(\boldsymbol{M} \times \frac{\mathrm{d}\boldsymbol{M}}{\mathrm{d}t} \right), \tag{2.13}$$

where α is the phenomenological damping constant and $\boldsymbol{H}_{\mathrm{eff}} = -\mu_0^{-1} \partial \mathcal{E} / \partial \boldsymbol{M}$ is the effective field. The total average energy density $\mathcal{E}$ includes the energy terms for Heisenberg exchange interaction, DMI, magnetic anisotropy, Zeeman interaction, and DDI in this dissertation, unless otherwise specified. The terms of LLG equation are illustrated in Fig. 2.1. The first term is the precessional torque resulting in the processional motion of $\boldsymbol{M}$ around $\boldsymbol{H}_{\mathrm{eff}}$. The second term is the damping torque leading to the damping motion of $\boldsymbol{M}$ toward $\boldsymbol{H}_{\mathrm{eff}}$.

2.4 Spin-transfer torques and spin-orbit torques

When the spin-polarized current is injected to a magnetic sample, the magnetization will be reoriented due to the spin-transfer torque (STT). The adiabatic and non-adiabatic STT

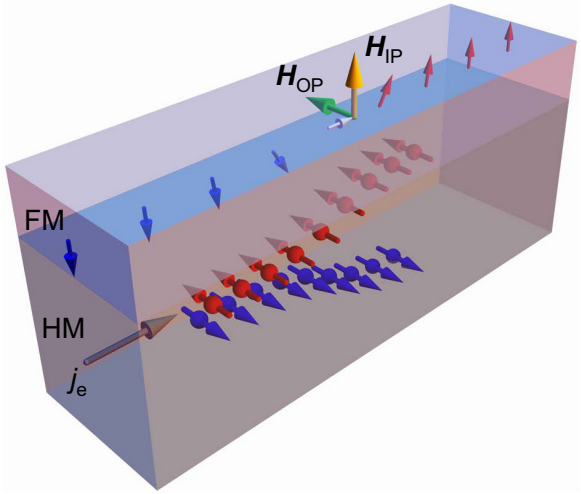

Figure 2.3: Schematic illustration of the SHE and the effective fields generated by the SOTs. The upper layer is a FM layer and the lower layer is a heavy-metal layer. The gray arrow indicates the electron flow.

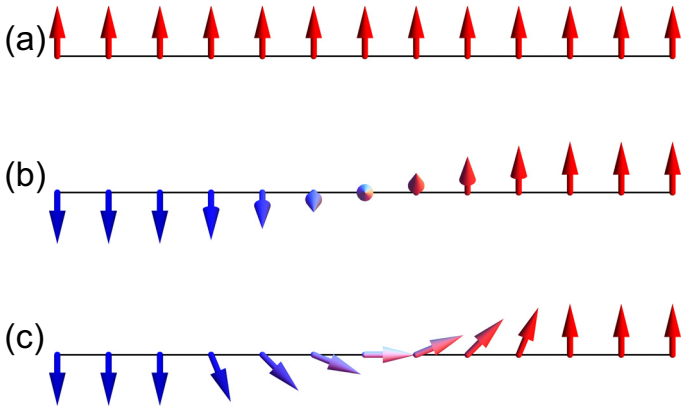

Figure 2.4: Schematic illustration of FM domain and domain walls. (a) A FM domain, (b) a Bloch-type domain wall, and (c) a Néel-type domain wall.

terms are taken as [15]

$$\begin{aligned} \boldsymbol{\tau}_{\text{adiab}} &= -u\boldsymbol{m} \times \left(\boldsymbol{m} \times \frac{\partial \boldsymbol{m}}{\partial x} \right), \\ \boldsymbol{\tau}_{\text{nonadiab}} &= -\beta u \boldsymbol{m} \times \frac{\partial \boldsymbol{m}}{\partial x}, \end{aligned} \tag{2.14}$$

where $u = |\frac{\gamma\hbar}{\mu_0 e}|\frac{jP}{2M_S}$ is the STT coefficient. $\hbar$ is the reduced Planck constant, e is the electron charge, j is the applied current density, and P is the spin polarization rate. β is the non-adiabatic STT coefficient. Figure 2.2 shows the schematic illustration of the effective fields ($\boldsymbol{H}_{\text{A}}$ and $\boldsymbol{H}_{\text{NA}}$) due to $\boldsymbol{\tau}_{\text{adiab}}$ and $\boldsymbol{\tau}_{\text{nonadiab}}$. The LLG equation (cf. Eq. 2.13)

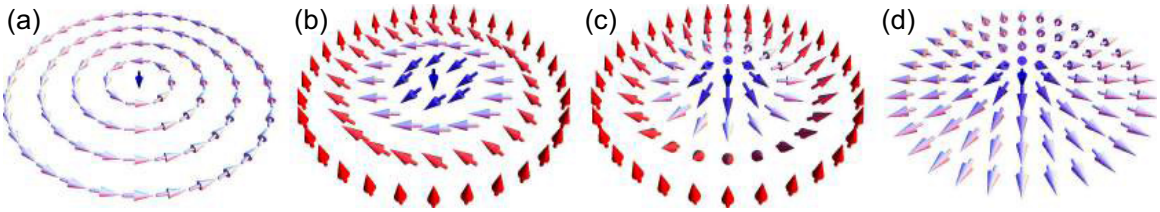

Figure 2.5: Schematic illustration of different types of magnetic structures in FM materials. (a) A vortex, (b) a bubble, (c) a skyrmion, and (d) a meron. Arrows denote the magnetization vectors.

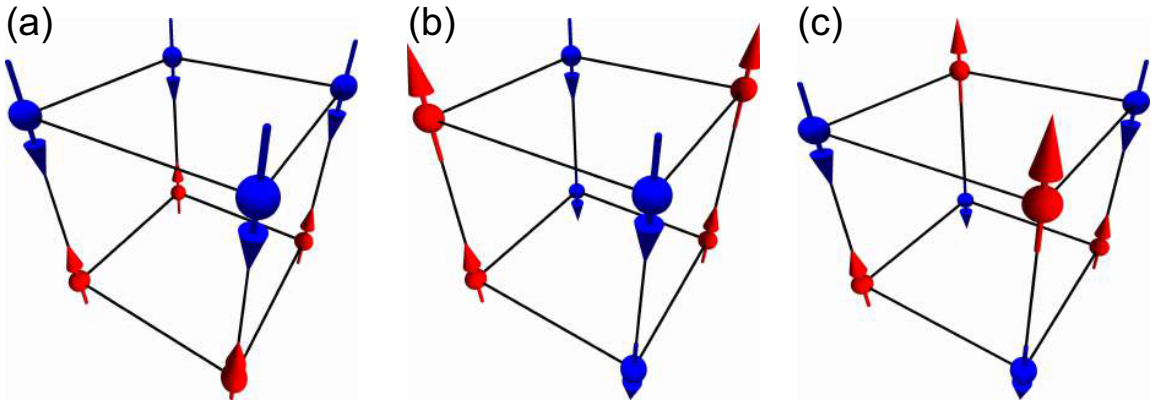

Figure 2.6: Schematic illustration of three types of AFM ordering. (a) A-type, (b) C-type, and (c) G-type. Arrows denote the magnetization vectors in a cubic lattice.

augmented with STTs reads

$$\frac{\mathrm{d}\boldsymbol{m}}{\mathrm{d}t} = \gamma \boldsymbol{m} \times \boldsymbol{h}_{\mathrm{eff}} + \alpha \left(\boldsymbol{m} \times \frac{\mathrm{d}\boldsymbol{m}}{\mathrm{d}t} \right) - u\boldsymbol{m} \times \left(\boldsymbol{m} \times \frac{\partial \boldsymbol{m}}{\partial x} \right) - \beta u \boldsymbol{m} \times \frac{\partial \boldsymbol{m}}{\partial x}, \tag{2.15}$$

where $\boldsymbol{h}_{\mathrm{eff}}$ is the reduced effective field, i.e., $\boldsymbol{h}_{\mathrm{eff}} = \boldsymbol{H}_{\mathrm{eff}}/M_{\mathrm{S}}$.

When a charge current is injected into a heavy-metal layer with strong spin-orbit coupling, the spin Hall effect (SHE) will convert the charge current to the spin current and result in the spin accumulation at the surfaces of the heavy-metal layer. If a FM layer is interfaced with the heavy-metal layer, the spin current will propagate into the FM layer and exert spin-orbit torques (SOTs) on the FM layer. The SOTs are written as [16, 17]

$$\begin{aligned} \boldsymbol{\tau}_{\mathrm{IP}} &= -\frac{u}{b} \boldsymbol{m} \times (\boldsymbol{m} \times \boldsymbol{p}), \\ \boldsymbol{\tau}_{\mathrm{OOP}} &= -\xi \frac{u}{b} \boldsymbol{m} \times \boldsymbol{p}, \end{aligned} \tag{2.16}$$

where $\boldsymbol{p}$ is the unit electron polarization direction, b is the FM layer thickness, and ξ is the amplitude of the out-of-plane torque relative to the in-plane one. For example, for the heavy-metal/FM bilayer, as shown in the Fig. 2.3, the spin current could be injected into

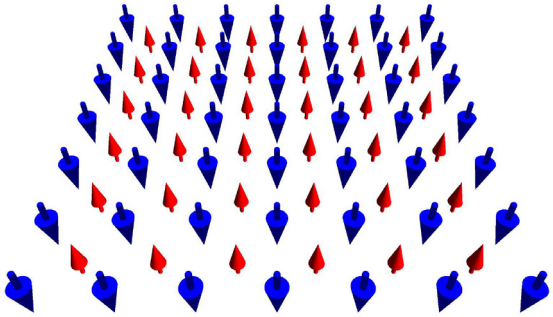

Figure 2.7: Schematic illustration of a ferrimagnetic structure. Arrow direction denotes the magnetization vector direction, while arrow size stands for the magnitude of magnetization.

the heavy metal layer. Due to the SHE, the electron with the same spin polarization will accumulate on one side. Then, the SOTs act on the magnetization, resulting in the motion of the domain wall. The effective fields of the in-plane and out-of-plane terms are illustrated in Fig. 2.3. In this case, the domain wall moves against the electron flow, contrary to the case driven by conventional STTs. The vector of the spin polarization depends on the current direction and material properties, such as the spin Hall angle. For instance, $\boldsymbol{p} = \hat{y}$ for Pt/CoFe and $\boldsymbol{p} = -\hat{y}$ for Ta/CoFe [5]. Then, the LLG equation (cf. Eq. 2.13) augmented with SOTs reads

$$\frac{\mathrm{d}\boldsymbol{m}}{\mathrm{d}t} = \gamma \boldsymbol{m} \times \boldsymbol{h}_{\text{eff}} + \alpha \left(\boldsymbol{m} \times \frac{\mathrm{d}\boldsymbol{m}}{\mathrm{d}t} \right) - \frac{u}{b} \boldsymbol{m} \times (\boldsymbol{m} \times \boldsymbol{p}) - \xi \frac{u}{b} \boldsymbol{m} \times \boldsymbol{p}. \tag{2.17}$$

2.5 Typical magnetic structures

We have introduced typical interactions in magnetic materials in Sec. 2.2. Many different magnetic structures can be formed as a result of the competition between these interactions.

In FM materials, the strong Heisenberg exchange interaction leads to the magnetization pointing along the same direction. Figure 2.4(a) shows the magnetic structure for FM domain. When other interactions are considered and can not be neglected with respect to the Heisenberg exchange interaction, especially the DDI or DMI, multiple domains having different magnetization orientations will be formed to reduce the total energy, where the interfaces between adjacent domains are called domain walls. Figure 2.4(b) and 2.4(c) give two 180° domain walls, Bloch-type domain wall and Néel-type domain wall, respectively. For the Bloch-type domain wall, the magnetization rotates in a plane perpendicular to the plane of the domain wall. When the stray field in the FM system is not significant and the FM sample is thick, the Bloch-type domain wall is favorable. For the Néel-type domain wall, the rotation of the magnetization occurs in the plane parallel to the plane of the domain

wall. The Néel-type domain wall often occurs in FM ultrathin films, where the domain wall width is very large compared to the film thickness.

Figure 2.5 shows the magnetic structures for magnetic vortex, bubble, skyrmion, and meron. The magnetic vortex state can be found in thin film of the soft magnetic materials. The magnetic bubble often occurs when the thickness of the sample is comparable to the domain dimensions ($4\sqrt{AK}/\pi M_S^2$) and its quality factor $K/2\pi M_S^2 \geq 1$ [18]. The size of the magnetic bubble is usually of the order of micrometer. The configuration of the skyrmion is shown in Fig. 2.5(c). The magnetization rotates from $180°$ at the center to $0°$ at the edge. The skyrmion can be found in various magnetic materials with asymmetric exchange interactions, such as the DMI. The typical size of a skyrmion varies from sub-micrometer to nanometer ($1 \sim 1000$ nm). In the materials with in-plane anisotropy, the skyrmion solution will change to the meron pair [19]. The magnetic configuration of a single meron is shown in Fig. 2.5(d).

In AFM materials, the AFM exchange interaction make the magnetization to be antiparallel to the NN site. As shown in Fig. 2.6, there are three types of magnetization ordering in AFM materials, i.e., A-type, G-type and C-type. As the magnetization of the two underlying sublattices are equal in the perfect AFM system, there is no net magnetization for the AFM materials. If the magnetization of two underlying sublattices are not equal, then the magnetization of the system will not cancel out, as shown in Fig. 2.7. This kind of materials are ferrimagnets.

2.6 The Objected Oriented MicroMagnetic Framework

In this dissertation, all simulations regarding the magnetization dynamics are performed by using the 1.2α5 release of the Object Oriented MicroMagnetic Framework (OOMMF) [20]. The OOMMF is a public domain micromagnetics program developed at the National Institute of Standards and Technology, which is written in C++ and Tcl/Tk. The OOMMF can operate across a wide range of Unix, Mac OS X, and Windows platforms, and it forms a completely functional micromagnetics package, with the additional capability to be extended by users. Our simulations are carried out by a set of the OOMMF extensible solver objects of the standard OOMMF distribution. We also include several OXS extension modules in order to model, for examples, the DMI and frustrated exchange interactions (cf. Ch. 4.4).

BIBLIOGRAPHY

[1] J. Stöhr, and H. C. Siegmann, *Magnetism: From Fundamentals to Nanoscale Dynamics* (Springer Berlin Heidelberg, 2006).

[2] I. Dzyaloshinsky, A thermodynamic theory of "weak" ferromagnetism of antiferromagnetics. J. Phys. Chem. Solids **4**, 241–255 (1958).

[3] T. Moriya, Anisotropic superexchange interaction and weak ferromagnetism. Phys. Rev. **120**, 91–98 (1960).

[4] S. Heinze, K. Bergmannvon, M. Menzel, J. Brede, A. Kubetzka, R. Wiesendanger, G. Bihlmayer, and S. Blugel, Spontaneous atomic-scale magnetic skyrmion lattice in two dimensions. Nat. Phys. **7**, 713–718 (2011).

[5] S. Emori, U. Bauer, S.-M. Ahn, E. Martinez, and G. S. D. Beach, Current-driven dynamics of chiral ferromagnetic domain walls. Nat. Mater. **12**, 611–616 (2013).

[6] S. Rohart, and A. Thiaville, Skyrmion confinement in ultrathin film nanostructures in the presence of Dzyaloshinskii-Moriya interaction. Phys. Rev. B **88**, 184422 (2013).

[7] A. Thiaville, S. Rohart, É. Jué, V. Cros, and A. Fert, Dynamics of Dzyaloshinskii domain walls in ultrathin magnetic films. EPL (Europhysics Letters) **100**, 57002 (2012).

[8] J. Sampaio, V. Cros, S. Rohart, A. Thiaville, and A. Fert, Nucleation, stability and current-induced motion of isolated magnetic skyrmions in nanostructures. Nat. Nanotechnol. **8**, 839–844 (2013).

[9] S. Mühlbauer, B. Binz, F. Jonietz, C. Pfleiderer, A. Rosch, A. Neubauer, R. Georgii, and P. Böni, Skyrmion lattice in a chiral magnet. Science **323**, 915–919 (2009).

[10] X. Z. Yu, Y. Onose, N. Kanazawa, J. H. Park, J. H. Han, Y. Matsui, N. Nagaosa, and Y. Tokura, Real-space observation of a two-dimensional skyrmion crystal. Nature **465**, 901–904 (2010).

[11] X. Z. Yu, N. Kanazawa, Y. Onose, K. Kimoto, W. Z. Zhang, S. Ishiwata, Y. Matsui, and Y. Tokura, Near room-temperature formation of a skyrmion crystal in thin-films of the helimagnet FeGe. Nat. Mater. **10**, 106–109 (2011).

[12] L. D. Landau, and E. Lifshitz, On the theory of the dispersion of magnetic permeability in ferromagnetic bodies. Phys. Z. Sowjetunion **8**, 153–169 (1935).

[13] T. L. Gilbert, A Lagrangian formulation of the gyromagnetic equation of the magnetization field. Phys. Rev. **100**, 1243 (1955).

[14] T. L. Gilbert, A phenomenological theory of damping in ferromagnetic materials. IEEE Trans. Magn. **40**, 3443–3449 (2004).

[15] A. Thiaville, Y. Nakatani, J. Miltat, and Y. Suzuki, Micromagnetic understanding of current-driven domain wall motion in patterned nanowires. EPL (Europhysics Letters) **69**, 990 (2005).

[16] J. Xiao, A. Zangwill, and M. D. Stiles, Boltzmann test of Slonczewski's theory of spin-transfer torque. Phys. Rev. B **70**, 172405 (2004).

[17] A. V. Khvalkovskiy, V. Cros, D. Apalkov, V. Nikitin, M. Krounbi, K. A. Zvezdin, A. Anane, J. Grollier, and A. Fert, Matching domain-wall configuration and spin-orbit torques for efficient domain-wall motion. Phys. Rev. B **87**, 020402(R) (2013).

[18] A. Malozemoff, and J. Slonczewski, *Magnetic Domain Walls in Bubble Materials: Advances in Materials and Device Research* (Academic press, 2016).

[19] S.-Z. Lin, A. Saxena, and C. D. Batista, Skyrmion fractionalization and merons in chiral magnets with easy-plane anisotropy. Phys. Rev. B **91**, 224407 (2015).

[20] M. J. Donahue, and D. G. Porter, OOMMF User's Guide, Version 1.0, Interagency Report. NO.NISTIR **6376**, 158 (1999).

CHAPTER 3

Magnetic skyrmion and skyrmion Hall effect

In this chapter, we provide a review on the magnetic skyrmion as well as its topological charge. Besides, we present a theoretical and numerical study on the SkHE, which is supported by recent experimental observations.

3.1 Magnetic skyrmion

The skyrmion is a topological soliton or a topological defect in condensed-matter systems [1, 2, 3, 4, 5, 6, 7, 8, 9]. Originally, it was proposed by British nuclear physicist Tony Skyrme in the 1960's as a quasi-particle-like topological excitation in certain field theories for the description of the interactions of pions [10]. Later in the 1990's, Bogdanov et al. for the first time theoretically suggested that the topologically protected skyrmion can be existed as a stable or metastable state in magnetic materials with DMIs [11]. In 2001, Bogdanov and Rößler theoretically predicted and described the skyrmion in magnetic thin films [1]. Then, in 2009, Mühlbauer et al. first experimentally observed the magnetic skyrmion lattice in B20-type bulk chiral magnet MnSi with broken inversion symmetry [3]. Subsequently, skyrmions have been experimentally observed, created, and manipulated in a number of material systems, including magnetic materials [12, 13, 14, 15], multiferroic materials [16], ferroelectric materials [17], and semiconductors [18]. Due to the beneficial properties of the topologically protected stability as well as the efficient mobility driven by external forces, magnetic skyrmions are anticipated to be predominantly employed as information carriers in future data storage and information processing devices [4, 5, 19, 20], logic computing devices [21, 22], microwave devices [23, 24], spin-wave/magnon devices [25, 26], and transistor-like functional devices [26, 27].

For most common cases, the magnetic skyrmion is referred to the two-dimensional

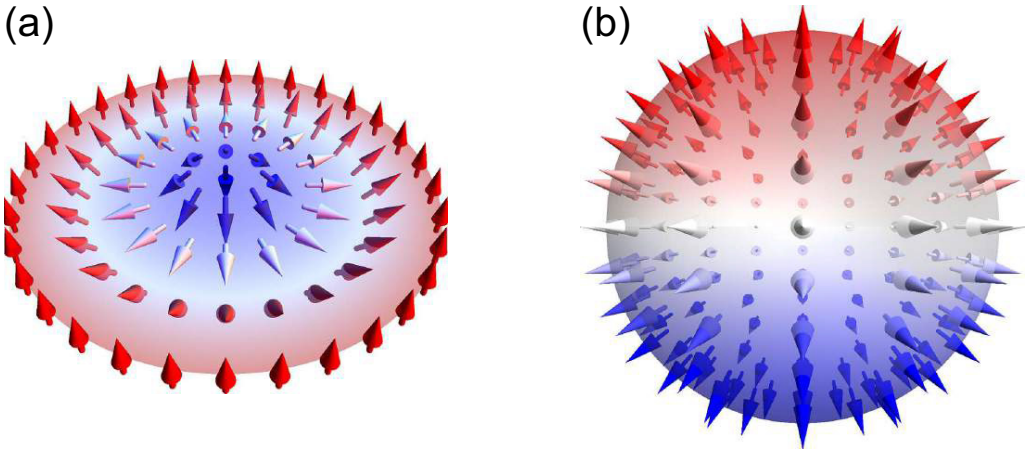

Figure 3.1: (a) Illustration of a 2D magnetic skyrmion. The arrows denote the spin direction and the out-of-plane spin component is represented by the color: red is out of the plane, white is in-plane, and blue is into the plane. (b) Illustration of the mapping of a 2D magnetic skyrmion to a unit 3D spherical surface with spins pointing in all directions.

(2D) spin texture with a nanometer-scale size (i.e., typically between $1 \sim 1000$ nm), as shown in Fig. 3.1. The spin configuration of a magnetic skyrmion is swirling in the planar space and would wrap a unit 3D spherical surface with spins pointing in all directions in the compactification of the planar space (cf. Fig. 3.1 and Ref. [28]). The full structure and topological information of a magnetic skyrmion in the planar space can be characterized by three quantum numbers, i.e., the skyrmion number $Q_{\rm s}$, the vorticity number $Q_{\rm v}$, and the helicity number $Q_{\rm h}$. In the following, we discuss the three important quantum numbers in details.

The magnetic skyrmion in the planar geometry, for instance, an ultra-thin magnetic film, is mainly characterized by the topological charge, which is referred to as the Pontryagin number [4, 7]. The Pontryagin number is given by

$$Q_{\rm s} = \int d^2\boldsymbol{r}\rho_{\rm sk}(\boldsymbol{r}), \tag{3.1}$$

where the Pontryagin number density $\rho_{\rm sk}(\boldsymbol{r})$ reads

$$\rho_{\rm sk}(\boldsymbol{r}) = \frac{1}{4\pi}\boldsymbol{n}(\boldsymbol{r})\cdot(\partial_x\boldsymbol{n}(\boldsymbol{r})\times\partial_y\boldsymbol{n}(\boldsymbol{r}))\,. \tag{3.2}$$

Thus, we have the Pontryagin number of the magnetic skyrmion

$$Q_{\rm s} = \frac{1}{4\pi}\int d^2\boldsymbol{r}\cdot\boldsymbol{n}(\boldsymbol{r})\cdot(\partial_x\boldsymbol{n}(\boldsymbol{r})\times\partial_y\boldsymbol{n}(\boldsymbol{r}))\,, \tag{3.3}$$

which is also usually referred to as the skyrmion number. It counts how many times $\boldsymbol{n}(\boldsymbol{r})$ is wrapped as the coordinate (x, y) spans the whole planar space. A point of the planar

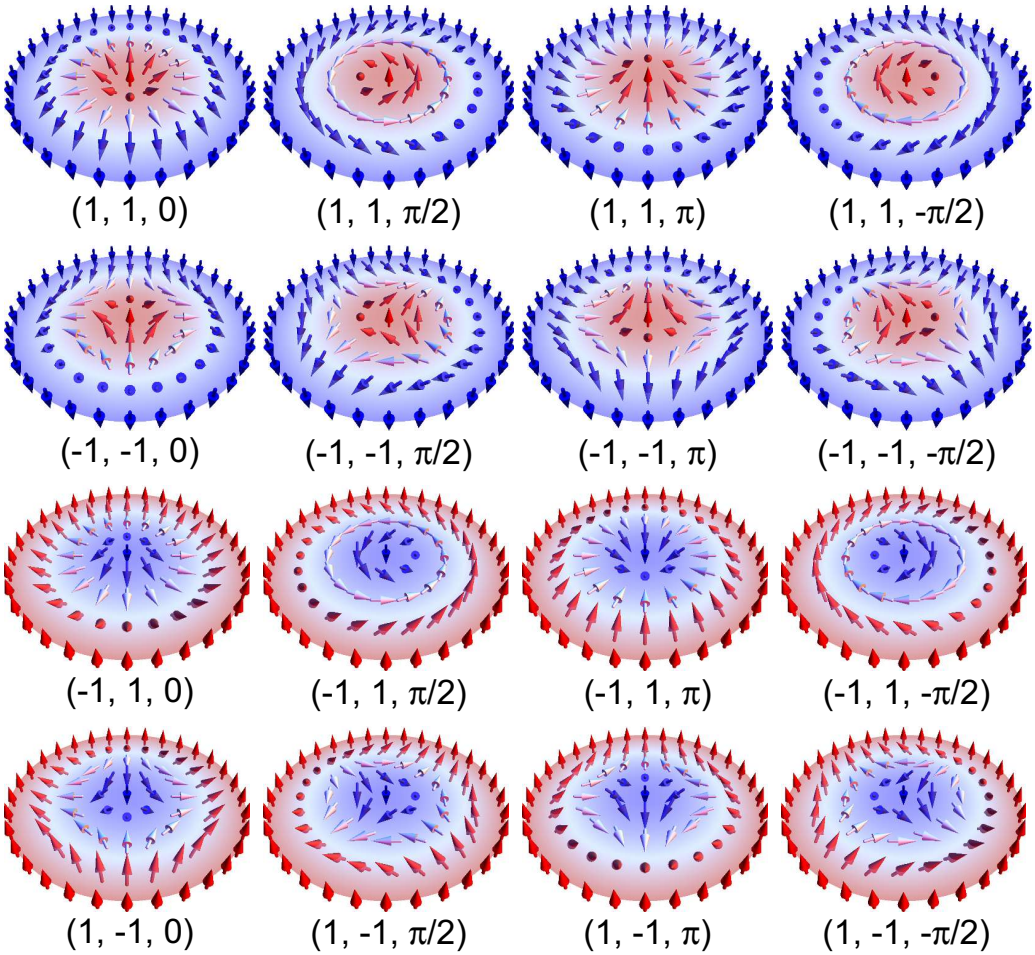

Figure 3.2: Illustrations of typical magnetic skyrmions with different topological quantum numbers (Q_{s}, Q_{v}, Q_{h}). The arrows denote the spin direction and the out-of-plane spin component is represented by the color: red is out of the plane, white is in-plane, and blue is into the plane.

space is parameterized as

$$x = r\cos\varphi, \quad y = r\sin\varphi. \tag{3.4}$$

By applying the mapping $r = 0$ as $z \to -1$, $r = 1$ as $z = 0$, $r \to \infty$ as $z \to 1$, and $\lim_{r\to\infty} \boldsymbol{n}(x, y) = \lim_{z\to 1} \boldsymbol{n}(z, \phi)$, we consider the compactification of the planar space to a 2-sphere in the xyz-space parameterized by

$$\begin{aligned} x &= \sqrt{1-z^2}\cos\phi(\varphi) = \sqrt{1-\cos^2\theta}\cos\phi, \\ y &= \sqrt{1-z^2}\sin\phi(\varphi) = \sqrt{1-\cos^2\theta}\sin\phi, \\ z &= z = \cos\theta, \end{aligned} \tag{3.5}$$

where z is defined by

$$r = \frac{1+z}{1-z} = \frac{1+\cos\theta}{1-\cos\theta}. \tag{3.6}$$

Hence, we can write

$$\boldsymbol{n}(\boldsymbol{r}) = \boldsymbol{n}(\theta,\phi) = (\sin\theta\cos\phi, \sin\theta\sin\phi, \cos\theta). \tag{3.7}$$

By substituting Eq. (3.7) into Eq. (3.3), we obtain

$$Q_{\mathrm{s}} = \frac{1}{4\pi}\int_{\pi}^{0}\sin\theta d\theta\int_{0}^{2\pi}d\phi = -\frac{1}{4\pi}[\cos\theta]_{\pi}^{0}[\phi]_{0}^{2\pi}. \tag{3.8}$$

Thus, it can be seen that the skyrmion number Q_{s} is defined by both the out-of-plane (θ) and in-plane (ϕ) textures of the magnetic skyrmion. It should be noted that we only consider the regular solution where θ rotates π when r goes from zero to infinity (cf. Ref. [29] for other complex solutions). Therefore, with respect to the out-of-plane spin texture of the magnetic skyrmion, when the spins at $r \to \infty$ point in the $+z$-direction while the spin at $r = 0$ points in the $-z$-direction, $[\cos\theta]_{\pi}^{0} = 2$, resulting in the skyrmion number for the magnetic film with spin-up $\uparrow$ (pointing in the $+z$-direction) background

$$Q_{\mathrm{s}}^{\uparrow} = -\frac{1}{2\pi}[\phi]_{0}^{2\pi}. \tag{3.9}$$

In the same way, when the spins at $r \to \infty$ point in the $-z$-direction while the spin at $r = 0$ points in the $+z$-direction, $[\cos\theta]_{\pi}^{0} = -2$, resulting in the skyrmion number for the magnetic film with spin-down $\downarrow$ (pointing in the $-z$-direction) background

$$Q_{\mathrm{s}}^{\downarrow} = \frac{1}{2\pi}[\phi]_{0}^{2\pi}. \tag{3.10}$$

On the other hand, since there are several possibilities for the in-plane texture of the magnetic skyrmion, we hereby introduce the vorticity number Q_{v} and the helicity number Q_{h}, which completely characterize the in-plane spin texture of the magnetic skyrmion. The vorticity number Q_{v} is defined by the winding number of the in-plane spin texture, namely

$$Q_{\mathrm{v}} = \frac{1}{2\pi}\oint_{C}d\phi = \frac{1}{2\pi}[\phi]_{\varphi=0}^{\varphi=2\pi}. \tag{3.11}$$

The helicity number Q_{h} is defined by the phase appearing in

$$\phi = Q_{\mathrm{v}}\varphi + Q_{\mathrm{h}}. \tag{3.12}$$

Accordingly, we can rewrite Eq. (3.7) as

$$\boldsymbol{n} = [\sin\theta\cos(Q_{\mathrm{v}}\varphi + Q_{\mathrm{h}}), \sin\theta\sin(Q_{\mathrm{v}}\varphi + Q_{\mathrm{h}}), \cos\theta]. \tag{3.13}$$

Clearly, it can be seen that the skyrmion number Q_{s} is a function of the vorticity number Q_{v}, namely

$$Q_{\mathrm{s}} = -\frac{1}{2}[\cos\theta]_{\pi}^{0} Q_{\mathrm{v}}. \tag{3.14}$$

Specifically, for the system of the magnetic film with spin-up $\uparrow$ background, we have

$$Q_{\mathrm{s}}^{\uparrow} = -Q_{\mathrm{v}}, \tag{3.15}$$

while for the system of the magnetic film with spin-down $\downarrow$ background, we have

$$Q_{\mathrm{s}}^{\downarrow} = Q_{\mathrm{v}}. \tag{3.16}$$

That is to say, when the initial spin configuration of the magnetic film is established, either spin-up $\uparrow$ or spin-down $\downarrow$, the skyrmion number Q_{s} of the magnetic skyrmion is determined by its vorticity number Q_{v} as the out-of-plane spin texture of the magnetic skyrmion is fixed. Indeed, the vorticity number Q_{v} and the helicity number Q_{h} determine the in-plane spin texture of the magnetic skyrmion. The magnetic skyrmion is completely characterized by the three numbers $(Q_{\mathrm{s}}, Q_{\mathrm{v}}, Q_{\mathrm{h}})$.

Figure 3.2 depicts typical examples of the magnetic skyrmion with different Q_{s}, Q_{v} and Q_{h}. For the sake of simplicity, we only consider the basic cases where the absolute value of the skyrmion number Q_{s} is equal to one. In conventional FM materials, the most stable states of the magnetic skyrmion in the presence of the positive interface-induced DMI are the states with $(1, 1, \pi)$ and $(-1, 1, 0)$, while the most stable states in the presence of the negative interface-induced DMI are the states with $(1, 1, 0)$ and $(-1, 1, \pi)$. The most stable states of the magnetic skyrmion in the presence of the positive bulk DMI are the states with $(1, 1, \pi/2)$ and $(-1, 1, -\pi/2)$, while the most stable states in the presence of the negative bulk DMI are the states with $(1, 1, -\pi/2)$ and $(-1, 1, \pi/2)$.

Here, we also discuss the magnetic skyrmion and magnetic antiskyrmion. As pointed in Ref. [30], the antiskyrmion is a topological soliton possessing a negative topological charge that approaches the same spin-polarized ground state asymptotically. First, in the system where the initial spin configuration of the magnetic film is given and cannot be altered, the topological charge of the magnetic skyrmion, i.e., the skyrmion number Q_{s}, is determined solely by its in-plane spin texture, i.e., the vorticity number Q_{v}. Hence, if the magnetic skyrmion is of $(Q_{\mathrm{s}}, Q_{\mathrm{v}}, Q_{\mathrm{h}})$, the magnetic antiskyrmion would be of $(Q'_{\mathrm{s}}, Q'_{\mathrm{v}}, Q'_{\mathrm{h}})$, where $Q'_{\mathrm{v}} = -Q_{\mathrm{v}}$. This is the strict definition of a magnetic antiskyrmion. Second, in the system where the initial spin configuration of the magnetic film is given but can be changed, as demonstrated in Ref. [21], the topological charge of the magnetic skyrmion, i.e., the skyrmion number Q_{s}, is determined corporately by its in-plane and out-of-plane spin textures.

Hence, if the magnetic skyrmion is of $(Q_\mathrm{s}, Q_\mathrm{v}, Q_\mathrm{h})$, the magnetic antiskyrmion would be of $(Q'_\mathrm{s}, Q'_\mathrm{v}, Q'_\mathrm{h})$, where $Q'_\mathrm{s} = -Q_\mathrm{s}$ or $Q'_\mathrm{v} = -Q_\mathrm{v}$. This is the definition of a magnetic antiskyrmion in a more general sense.

3.2 Skyrmion Hall effect

The well-known ordinary Hall effect, which was discovered by American physicist Edwin Hall in 1879, describes the transverse deflection of charged particles (i.e., electrons or holes) as a result of the Lorentz force [32]. As discussed in the last section, the magnetic skyrmion can be seen as a quasiparticle carrying certain quantized topological charge. Meanwhile, the magnetic skyrmion can be displaced by an external driving force [33, 34, 35, 36, 37, 38, 25], for example, the spin-polarized current (cf. Ch. 4). Therefore, it is intriguing to think about if the quasiparticle-like magnetic skyrmion with a topological charge shows dynamic behaviors similar to the ordinary Hall effect at certain conditions. Indeed, in the most common cases, a magnetic skyrmion in conventional FM materials cannot move in a straight line along the driving current direction (cf. Fig. 3.3), since it feels the topological structure-induced Magnus force which bends its trajectory [4, 39, 40, 41]. This phenomenon is referred to as the SkHE, which was first theoretically predicted by Zang et al. [42] and has recently been directly observed in experiments by two independent groups, Jiang et al. [39] and Litzius et al. [40]. In order to fully understand the SkHE, it is insightful to start with a theoretical approach, which describes the translational motion of a rigid magnetic skyrmion explicitly.

The magnetic skyrmion can be driven into motion by different types of spin currents (cf. Ch. 2 and Ch. 4). First, we analyze the SkHE driven by the Slonczewski-like STT [43, 44, 45], which can be provided by the vertically injected spin current generated by the SHE [43, 44, 45] in a heavy-metal layer [i.e., by the current-perpendicular-to-plane (CPP) geometry]. That is to say, a charge current is injected into the heavy-metal substrate layer, where the charge current is converted to a spin current propagating to the FM layer via the SHE, which drives the magnetic skyrmion in the FM layer into motion (cf. Fig. 3.4). The steady motion of a rigid magnetic skyrmion driven by the SHE in an infinite FM layer (i.e., no boundary effect) can be well described by the Thiele motion equation (cf. Appendix A), which is expressed as follows [4, 37, 39, 46, 47, 48]

$$\boldsymbol{G} \times \boldsymbol{v} - \alpha \boldsymbol{\mathcal{D}} \cdot \boldsymbol{v} + 4\pi \boldsymbol{\mathcal{B}} \cdot \boldsymbol{j}_\mathrm{h} = \boldsymbol{0}, \tag{3.17}$$

where the skyrmion velocity $\boldsymbol{v} = (v_x, v_y)$, and $\boldsymbol{j}_\mathrm{h} = (j_x, j_y)$ denotes the charge current in the heavy-metal substrate layer. The first term on left-hand side of Eq. (3.17) is the Magnus

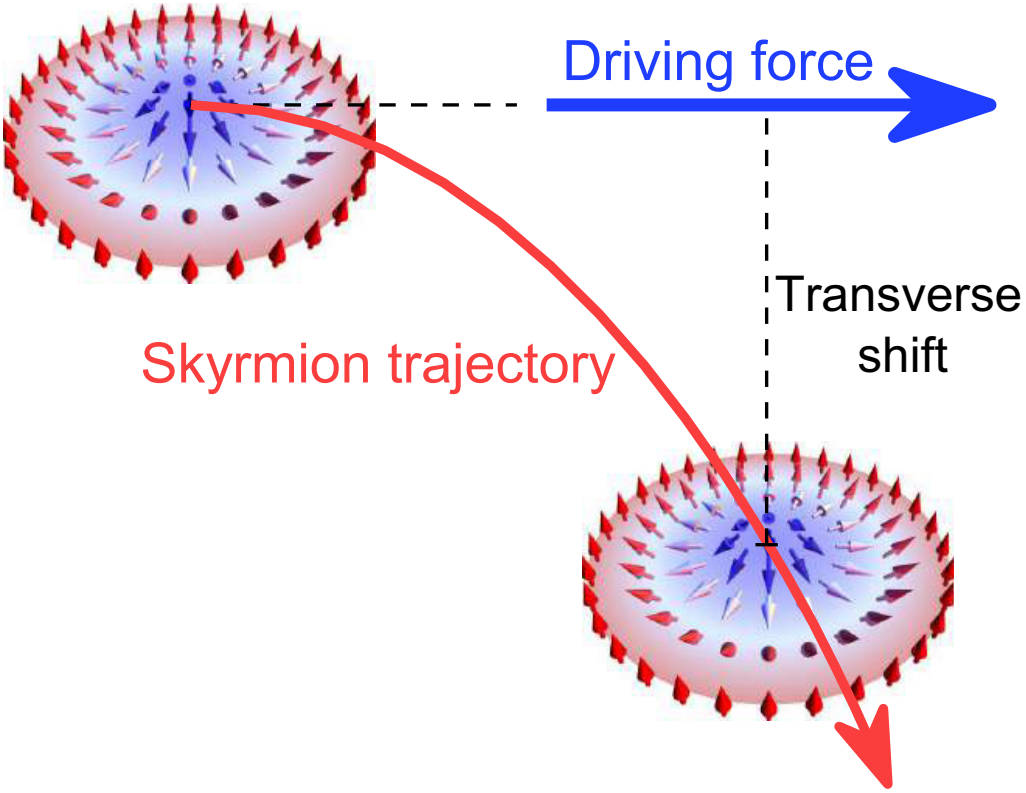

Figure 3.3: Schematic of the SkHE. The magnetic skyrmion moves at an angle with respect to the direction of the driving force provided by the spin-polarized current.

force term with the gyromagnetic coupling vector

$$\boldsymbol{G} = (0, 0, G), \tag{3.18}$$

where

$$G = -4\pi Q. \tag{3.19}$$

The skyrmion number Q is defined as

$$Q = \frac{1}{4\pi} \int \boldsymbol{m} \cdot (\frac{\partial \boldsymbol{m}}{\partial x} \times \frac{\partial \boldsymbol{m}}{\partial y}) dxdy. \tag{3.20}$$

The second term on left-hand side of Eq. (3.17) is the dissipative force term with the dissipative tensor describing the effect of the dissipative force on the moving magnetic skyrmion

$$\boldsymbol{\mathcal{D}} = 4\pi \begin{pmatrix} \mathcal{D}_{xx} & \mathcal{D}_{xy} \\ \mathcal{D}_{yx} & \mathcal{D}_{yy} \end{pmatrix}, \tag{3.21}$$

where the tensor components are calculated by

$$\mathcal{D}_{\mu\nu} = \frac{1}{4\pi} \int \frac{\partial \boldsymbol{m}}{\partial \mu} \cdot \frac{\partial \boldsymbol{m}}{\partial \nu} dxdy, \tag{3.22}$$

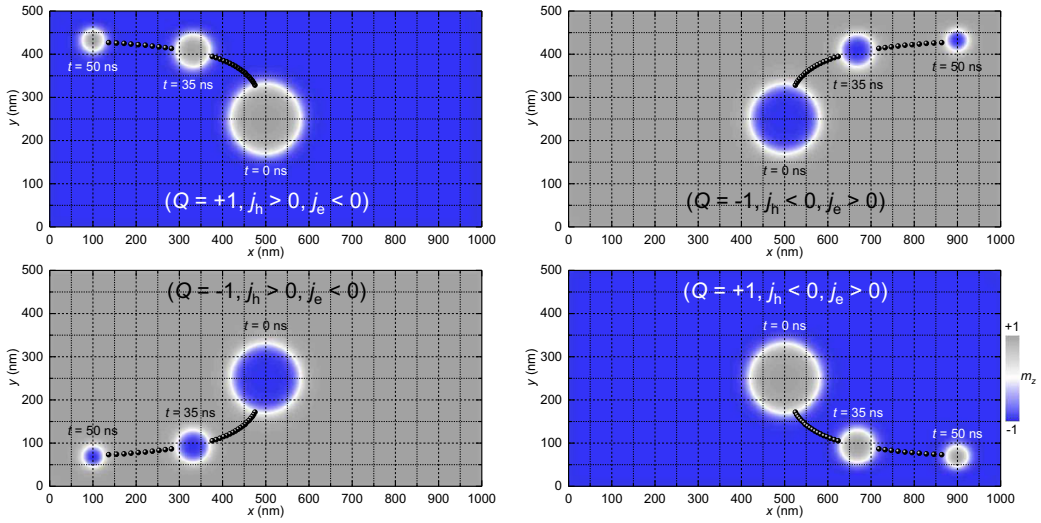

Figure 3.4: Simulation of the skyrmion motion driven by SHE generated spin current on the signs of electron current ($\boldsymbol{j}_\mathrm{e}$) and topological charge (Q). Note $\boldsymbol{j}_\mathrm{e} = -\boldsymbol{j}_\mathrm{h}$. Adapted with permission from the author's original work [39].

where μ and ν run over x and y. The integrations are carried out over the region containing the magnetic skyrmion. For the rigid magnetic skyrmion, the relations that hold are the following

$$\mathcal{D}_{xx} = \mathcal{D}_{yy} = \mathcal{D} \tag{3.23}$$

$$\mathcal{D}_{xy} = \mathcal{D}_{yx} = 0. \tag{3.24}$$

The third term on left-hand side of Eq. (3.17) is the driving force term with the tensor linked to the STT generated by the SHE

$$\boldsymbol{\mathcal{B}} = \frac{u}{a j_\mathrm{h}} \begin{pmatrix} -\mathcal{I}_{xy} & \mathcal{I}_{xx} \\ -\mathcal{I}_{yy} & \mathcal{I}_{yx} \end{pmatrix}, \tag{3.25}$$

where $u = |\frac{\gamma_0 \hbar}{\mu_0 e}| \frac{j_\mathrm{h} \theta_\mathrm{sh}}{2 M_\mathrm{S}}$ is the electron drift velocity, θ_sh is the spin Hall angle, M_S is the saturation magnetization, a is the FM layer thickness. The tensor components are calculated by

$$\mathcal{I}_{\mu\nu} = \frac{1}{4\pi} \int \left(\frac{\partial \boldsymbol{m}}{\partial \mu} \times \boldsymbol{m} \right)_\nu dxdy, \tag{3.26}$$

where μ and ν run over x and y. For the rigid hedgehog-like magnetic skyrmion that is studied in this dissertation, the relations that hold are the following

$$\mathcal{I}_{xx} = \mathcal{I}_{yy} = 0 \tag{3.27}$$

$$\mathcal{I}_{xy} = -\mathcal{I}_{yx} = \mathcal{I}. \tag{3.28}$$

Hence, the Thiele motion equation (3.17) can be rewritten into the following form

$$\begin{pmatrix} +4\pi Q v_y \\ -4\pi Q v_x \end{pmatrix} - \begin{pmatrix} 4\pi\alpha\mathcal{D} v_x \\ 4\pi\alpha\mathcal{D} v_y \end{pmatrix} - \begin{pmatrix} \frac{4\pi u}{a j_\mathrm{h}}\mathcal{I} j_x \\ \frac{4\pi u}{a j_\mathrm{h}}\mathcal{I} j_y \end{pmatrix} = \begin{pmatrix} 0 \\ 0 \end{pmatrix}. \tag{3.29}$$

Therefore, we can get the following relation

$$\begin{pmatrix} v_x \\ v_y \end{pmatrix} = \frac{u}{a j_\mathrm{h}}\mathcal{I} \begin{pmatrix} \frac{-\alpha\mathcal{D}}{Q^2+\alpha^2\mathcal{D}^2} & \frac{-Q}{Q^2+\alpha^2\mathcal{D}^2} \\ \frac{Q}{Q^2+\alpha^2\mathcal{D}^2} & \frac{-\alpha\mathcal{D}}{Q^2+\alpha^2\mathcal{D}^2} \end{pmatrix} \begin{pmatrix} j_x \\ j_y \end{pmatrix}. \tag{3.30}$$

Obviously, it can be seen that

$$v_x = \frac{u}{a j_\mathrm{h}}\mathcal{I} \cdot \frac{-\alpha\mathcal{D} j_x - Q j_y}{Q^2+\alpha^2\mathcal{D}^2} = \left|\frac{\gamma_0\hbar}{\mu_0 e}\right| \frac{\theta_\mathrm{sh}\mathcal{I}}{2aM_\mathrm{S}} \cdot \frac{-\alpha\mathcal{D} j_x - Q j_y}{Q^2+\alpha^2\mathcal{D}^2}, \tag{3.31}$$

$$v_y = \frac{u}{a j_\mathrm{h}}\mathcal{I} \cdot \frac{Q j_x - \alpha\mathcal{D} j_y}{Q^2+\alpha^2\mathcal{D}^2} = \left|\frac{\gamma_0\hbar}{\mu_0 e}\right| \frac{\theta_\mathrm{sh}\mathcal{I}}{2aM_\mathrm{S}} \cdot \frac{Q j_x - \alpha\mathcal{D} j_y}{Q^2+\alpha^2\mathcal{D}^2}. \tag{3.32}$$

Thus, the skyrmion Hall angle is given as

$$\Phi_\mathrm{sk} = \tan^{-1}\left(\frac{v_y}{v_x}\right) = \tan^{-1}\left(\frac{Q j_x - \alpha\mathcal{D} j_y}{-\alpha\mathcal{D} j_x - Q j_y}\right). \tag{3.33}$$

For the system with a spatially homogeneous charge current applied along the x direction, that is, $j_y = 0$, the velocity of the magnetic skyrmion is given as

$$v_x = \left|\frac{\gamma_0\hbar}{\mu_0 e}\frac{\theta_\mathrm{sh}\mathcal{I}}{2aM_\mathrm{S}}\right| \cdot \frac{-\alpha\mathcal{D}}{Q^2+\alpha^2\mathcal{D}^2} \cdot j_x, \tag{3.34}$$

$$v_y = \left|\frac{\gamma_0\hbar}{\mu_0 e}\frac{\theta_\mathrm{sh}\mathcal{I}}{2aM_\mathrm{S}}\right| \cdot \frac{Q}{Q^2+\alpha^2\mathcal{D}^2} \cdot j_x. \tag{3.35}$$

Accordingly, the skyrmion Hall angle is given as

$$\Phi_\mathrm{sk} = \tan^{-1}\left(\frac{v_y}{v_x}\right) = \tan^{-1}\left(-\frac{Q}{\alpha\mathcal{D}}\right). \tag{3.36}$$

It can be seen that the skyrmion Hall angle is proportional to the topological charge Q and is inversely proportional to the damping coefficient α.

As shown in Fig. 3.4, the SkHE was also studied by numerical simulations (cf. Ch. 4). It can be seen that the magnetic skyrmion driven by the SHE generated STT moves towards the upper or lower edge of the sample, which can be explained by Eq. 3.33. Note that during the motion along the edge, the size of magnetic skyrmion shrinks due to the repulsive force from the edge. Details on the numerical study of the current-driven skyrmion motion are provided in the next chapter.

In the following, we also analyze the SkHE driven by the Zhang-Li STT [50], which can be provided by the in-plane injected spin-polarized current [i.e., by the current-in-plane

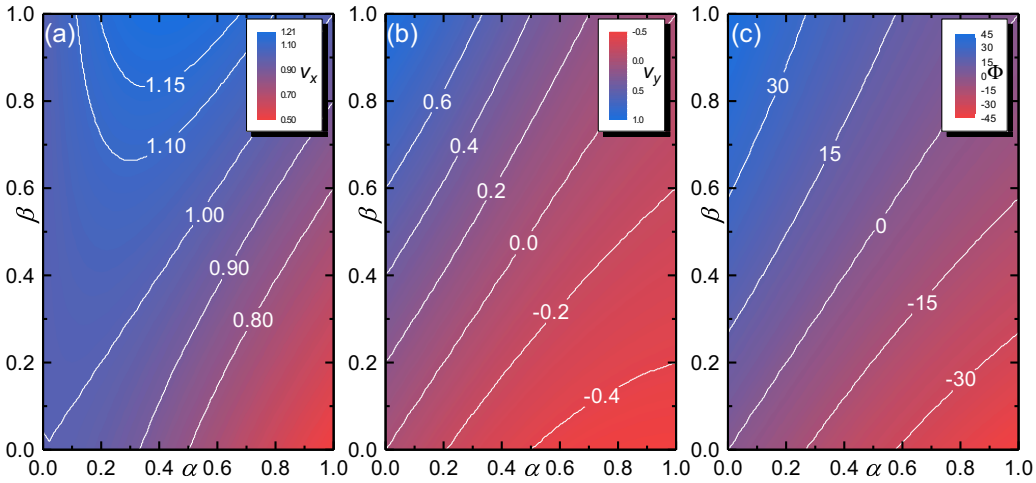

Figure 3.5: (a) v_x, (b) v_y, and (c) Φ_{sk} as functions of α and β given by Eq. (3.39) and Eq. (3.40), respectively. Note v_x and v_y are reduced by u. Adapted with permission from the author's original work [49].

(CIP) geometry], using the Thiele motion equation [28, 35, 46, 48, 51, 52, 53] by assuming the magnetic skyrmion moves in an infinite film (i.e., no boundary effect). The Thiele motion equation (cf. Appendix A) is expressed as

$$\boldsymbol{G} \times (\boldsymbol{v} - \boldsymbol{u}) + \boldsymbol{\mathcal{D}} (\beta \boldsymbol{u} - \alpha \boldsymbol{v}) = \boldsymbol{0}, \tag{3.37}$$

where $\boldsymbol{G} = (0, 0, -4\pi Q)$ is the gyromagnetic coupling vector with the skyrmion number Q. $\boldsymbol{m} = \boldsymbol{M}/M_{\text{S}}$ is the reduced magnetization and $\boldsymbol{\mathcal{D}}$ is the dissipative tensor (cf. Eq. 3.21). $\boldsymbol{u} = (u, 0)$ is the conduction electron velocity, $\boldsymbol{v}$ is the skyrmion velocity, α is the damping coefficient, and β is the strength of the non-adiabatic STT (cf. Ch. 2). For the nanoscale magnetic skyrmion studied here, we have

$$Q = -1, \quad \mathcal{D}_{xx} = \mathcal{D}_{yy} = 1, \quad \mathcal{D}_{xy} = \mathcal{D}_{yx} = 0. \tag{3.38}$$

Hence, the skyrmion velocity is given as

$$v_x = u\frac{(\alpha\beta + 1)}{\alpha^2 + 1}, \quad v_y = u\frac{(\beta - \alpha)}{\alpha^2 + 1}. \tag{3.39}$$

The skyrmion Hall angle Φ_{sk} is thus given as

$$\Phi_{\text{sk}} = \tan^{-1}(v_y/v_x) = \tan^{-1}\left(\frac{\beta - \alpha}{\alpha\beta + 1}\right). \tag{3.40}$$

By comparing with Eq. 3.36, it can be seen that the SkHE induced by the Zhang-Li STT depends not only on the damping coefficient α but also the non-adiabatic STT coefficient β.

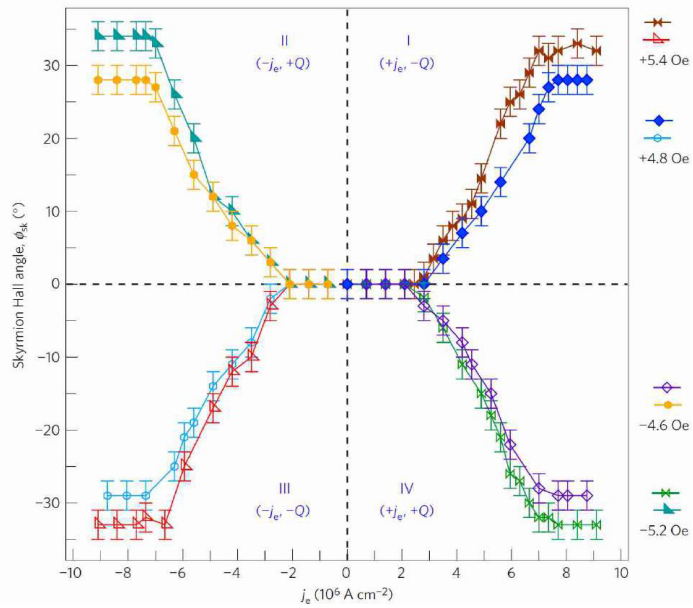

Figure 3.6: Experimental phase diagram of the skyrmion Hall angle as a function of current density/sign of topological charge in a magnetic multilayer device, obtained by tracking the motion of several tens of magnetic skyrmions. Adapted with permission from the author's original work [39].

By calculating Eq. (3.39), we show v_x as functions of α and β in Fig. 3.5(a). v_x ranges between $0.5u$ and $1.21u$, indicating the magnetic skyrmion always moves in the $+x$ direction. When $\alpha = 0.42$ and $\beta = 1$, v_x can reach the maximum value of $v_x = 1.21u$. Similarly, we show v_y as functions of α and β in Fig. 3.5(b). v_y ranges between $-0.5u$ and u, indicating the magnetic skyrmion can move in both the $\pm y$ directions. When $\alpha < \beta$, $v_y > 0$, the magnetic skyrmion shows a positive transverse motion, while when $\alpha > \beta$, $v_y < 0$, the magnetic skyrmion shows a negative transverse motion. By calculating Eq. (3.40), we also show Φ_{sk} as functions of α and β in Fig. 3.5(c), where Φ_{sk} varies between $\Phi_{\text{sk}} = 45°$ and $\Phi_{\text{sk}} = -45°$. Obviously, one has $\Phi_{\text{sk}} = 0°$, $\Phi_{\text{sk}} < 0°$, and $\Phi_{\text{sk}} > 0°$ for $\alpha = \beta$, $\alpha > \beta$, and $\alpha < \beta$, respectively.

Recently, the SkHE driven by the Slonczewski-like STT generated by the SHE was directly observed in experiments at room temperature [39]. As shown in Fig. 3.6, by using the SHE generated STT, we experimentally demonstrate the SkHE, where the experimentally measured skyrmion Hall angle depends on both the sign of the topological charge as well as the direction of the driving current, which agrees with theoretical results (cf. Eq. 3.33) and simulation results (cf. Fig. 3.4). It should be noted that the experimentally observed skyrmion Hall angle is a function of the driving current density, which is a result of the pinning effect in real magnetic materials. In the low-current-density regime, the magnetic skyrmion

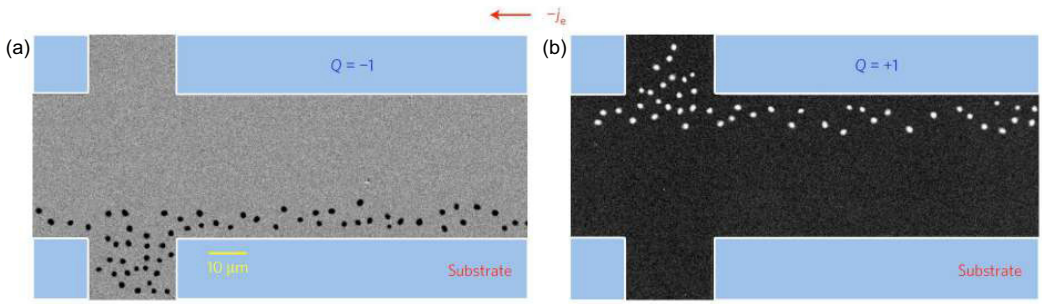

Figure 3.7: (a) Experimental demonstration of magnetic skyrmion ($Q = -1$) accumulation at the lower edge of the device. (b) Experimental demonstration of magnetic skyrmion ($Q = +1$) accumulation at the upper edge of the device. Adapted with permission from the author's original work [39].

shows the creep motion without net transverse shift. When the driving current density is larger than a certain threshold, the magnetic skyrmion shows the steady flow motion and the direction of skyrmion motion develops a well-defined transverse component. By alternating the sign of the driving electron current density ($\pm j_{\mathbf{e}}$) and the sign of topological charge ($\pm Q$), a phase diagram for the four different regimes was determined. Namely, for negative topological charge (under positive magnetic fields), regime I($+j_{\mathbf{e}}$,$+Q$) with positive Φ_{sk} and regime III($-j_{\mathbf{e}}$,$-Q$) with negative Φ_{sk} were identified by changing the polarity of the electron current. For skyrmions with positive topological charge (under negative magnetic fields) a positive Φ_{sk} in regime II($-j_{\mathbf{e}}$,$+Q$), and negative Φ_{sk} in regime IV($+j_{\mathbf{e}}$,$+Q$) were detected. Figure 3.7 shows the resultant magnetic skyrmion accumulation, by driving magnetic skyrmions from the creep motion regime into the steady flow motion regime. The experimental observation of SkHE may potentially create many exciting opportunities, such as topological selection.

BIBLIOGRAPHY

[1] A. N. Bogdanov, and U. K. Rößler, Chiral symmetry breaking in magnetic thin films and multilayers. Phys. Rev. Lett. **87**, 037203 (2001).

[2] U. K. Rößler, A. N. Bogdanov, and C. Pfleiderer, Spontaneous skyrmion ground states in magnetic metals. Nature **442**, 797–801 (2006).

[3] S. Mühlbauer, B. Binz, F. Jonietz, C. Pfleiderer, A. Rosch, A. Neubauer, R. Georgii, and P. Böni, Skyrmion lattice in a chiral magnet. Science **323**, 915–919 (2009).

[4] N. Nagaosa, and Y. Tokura, Topological properties and dynamics of magnetic skyrmions. Nat. Nanotechnol. **8**, 899–911 (2013).

[5] N. Romming, C. Hanneken, M. Menzel, J. E. Bickel, B. Wolter, K. Bergmannvon, A. Kubetzka, and R. Wiesendanger, Writing and deleting single magnetic skyrmions. Science **341**, 636–639 (2013).

[6] B. Dupé, M. Hoffmann, C. Paillard, and S. Heinze, Tailoring magnetic skyrmions in ultra-thin transition metal films. Nat. Commun. **5**, 4030 (2014).

[7] R. Wiesendanger, Nanoscale magnetic skyrmions in metallic films and multilayers: a new twist for spintronics. Nat. Rev. Mater. **1**, 16044 (2016).

[8] A. Fert, N. Reyren, and V. Cros, Magnetic skyrmions: advances in physics and potential applications. Nat. Rev. Mater. **2**, 17031 (2017).

[9] F. Casola, T. Sarvan der, and A. Yacoby, Probing condensed matter physics with magnetometry based on nitrogen-vacancy centres in diamond. Nat. Rev. Mater. **3**, 17088 (2018).

[10] T. H. R. Skyrme, A non-linear field theory. Proc. Royal Soc. A **260**, 127–138 (1961).

[11] A. Bogdanov, and A. Hubert, Thermodynamically stable magnetic vortex states in magnetic crystals. J. Magn. Magn. Mater. **138**, 255–269 (1994).

[12] X. Z. Yu, Y. Onose, N. Kanazawa, J. H. Park, J. H. Han, Y. Matsui, N. Nagaosa, and Y. Tokura, Real-space observation of a two-dimensional skyrmion crystal. Nature **465**, 901–904 (2010).

[13] S. Heinze, K. Bergmannvon, M. Menzel, J. Brede, A. Kubetzka, R. Wiesendanger, G. Bihlmayer, and S. Blugel, Spontaneous atomic-scale magnetic skyrmion lattice in two dimensions. Nat. Phys. **7**, 713–718 (2011).

[14] N. Romming, A. Kubetzka, C. Hanneken, K. Bergmannvon, and R. Wiesendanger, Field-dependent size and shape of single magnetic skyrmions. Phys. Rev. Lett. **114**, 177203 (2015).

[15] G. Chen, A. Mascaraque, A. T. N'Diaye, and A. K. Schmid, Room temperature skyrmion ground state stabilized through interlayer exchange coupling. Appl. Phys. Lett. **106**, 242404 (2015).

[16] S. Seki, X. Z. Yu, S. Ishiwata, and Y. Tokura, Observation of skyrmions in a multiferroic material. Science **336**, 198-201 (2012).

[17] Y. Nahas, S. Prokhorenko, L. Louis, Z. Gui, I. Kornev, and L. Bellaiche, Discovery of stable skyrmionic state in ferroelectric nanocomposites. Nat. Commun. **6**, 8542 (2015).

[18] B. Dupé, G. Bihlmayer, M. Böttcher, S. Blügel, and S. Heinze, Engineering skyrmions in transition-metal multilayers for spintronics. Nat. Commun. **7**, 11779 (2016).

[19] A. Fert, V. Cros, and J. Sampaio, Skyrmions on the track. Nat. Nanotechnol. **8**, 152–156 (2013).

[20] W. Koshibae, Y. Kaneko, J. Iwasaki, M. Kawasaki, Y. Tokura, and N. Nagaosa, Memory functions of magnetic skyrmions. Jpn. J. Appl. Phys. **54**, 053001 (2015).

[21] X. Zhang, M. Ezawa, and Y. Zhou, Magnetic skyrmion logic gates: conversion, duplication and merging of skyrmions. Sci. Rep. **5**, 9400 (2015).

[22] X. Xing, P. W. T. Pong, and Y. Zhou, Skyrmion domain wall collision and domain wall-gated skyrmion logic. Phys. Rev. B **94**, 054408 (2016).

[23] W. Wang, M. Beg, B. Zhang, W. Kuch, and H. Fangohr, Driving magnetic skyrmions with microwave fields. Phys. Rev. B **92**, 020403 (2015).

[24] B. Zhang, W. Wang, M. Beg, H. Fangohr, and W. Kuch, Microwave-induced dynamic switching of magnetic skyrmion cores in nanodots. Appl. Phys. Lett. **106**, 102401 (2015).

[25] X. Zhang, M. Ezawa, D. Xiao, G. P. Zhao, Y. Liu, and Y. Zhou, All-magnetic control of skyrmions in nanowires by a spin wave. Nanotechnology **26**, 225701 (2015).

[26] J. Xia, Y. Huang, X. Zhang, W. Kang, C. Zheng, X. Liu, W. Zhao, and Y. Zhou, A microwave field-driven transistor-like skyrmionic device with the microwave current-assisted skyrmion creation. J. Appl. Phys. **122**, 153901 (2017).

[27] X. Zhang, Y. Zhou, M. Ezawa, G. P. Zhao, and W. Zhao, Magnetic skyrmion transistor: skyrmion motion in a voltage-gated nanotrack. Sci. Rep. **5**, 11369 (2015).

[28] K. Everschor-Sitte, and M. Sitte, Real-space Berry phases: Skyrmion soccer (invited). J. Appl. Phys. **115**, 172602 (2014).

[29] S. Rohart, and A. Thiaville, Skyrmion confinement in ultrathin film nanostructures in the presence of Dzyaloshinskii-Moriya interaction. Phys. Rev. B **88**, 184422 (2013).

[30] Ezawa, Z. F. *Quantum Hall Effects.* (World Scientific, Singapore,2008).

[31] A. O. Leonov, and M. Mostovoy, Edge states and skyrmion dynamics in nanostripes of frustrated magnets. Nat. Commun. **8**, 14394 (2017).

[32] E. H. Hall, On a new action of the magnet on electric currents. Am. J. Math. **2**, 287–292 (1879).

[33] M. Mochizuki, Spin-wave modes and their intense excitation effects in skyrmion crystals. Phys. Rev. Lett. **108**, 017601 (2012).

[34] J. Sampaio, V. Cros, S. Rohart, A. Thiaville, and A. Fert, Nucleation, stability and current-induced motion of isolated magnetic skyrmions in nanostructures. Nat. Nanotechnol. **8**, 839–844 (2013).

[35] J. Iwasaki, M. Mochizuki, and N. Nagaosa, Universal current-velocity relation of skyrmion motion in chiral magnets. Nat. Commun. **4**, 1463 (2013).

[36] S.-Z. Lin, C. Reichhardt, C. D. Batista, and A. Saxena, Driven skyrmions and dynamical transitions in chiral magnets. Phys. Rev. Lett. **110**, 207202 (2013).

[37] R. Tomasello, E. Martinez, R. Zivieri, L. Torres, M. Carpentieri, and G. Finocchio, A strategy for the design of skyrmion racetrack memories. Sci. Rep. **4**, 6784 (2014).

[38] L. Kong, and J. Zang, Dynamics of an insulating skyrmion under a temperature gradient. Phys. Rev. Lett. **111**, 067203 (2013).

[39] W. Jiang, X. Zhang, G. Yu, W. Zhang, X. Wang, M. Benjamin Jungfleisch, J. E. Pearson, X. Cheng, O. Heinonen, K. L. Wang, Y. Zhou, A. Hoffmann, and S. G. E. Velthuiste, Direct observation of the skyrmion Hall effect. Nat. Phys. **13**, 162–169 (2017).

[40] K. Litzius, I. Lemesh, B. Kruger, P. Bassirian, L. Caretta, K. Richter, F. Buttner, K. Sato, O. A. Tretiakov, J. Forster, R. M. Reeve, M. Weigand, I. Bykova, H. Stoll, G. Schutz, G. S. D. Beach, and M. Klaui, Skyrmion Hall effect revealed by direct time-resolved X-ray microscopy. Nat. Phys. **13**, 170–175 (2017).

[41] B. L. Brown, U. C. Täuber, and M. Pleimling, Effect of the Magnus force on skyrmion relaxation dynamics. Phys. Rev. B **97**, 020405 (2018).

[42] J. Zang, M. Mostovoy, J. H. Han, and N. Nagaosa, Dynamics of skyrmion crystals in metallic thin films. Phys. Rev. Lett. **107**, 136804 (2011).

[43] L. Liu, C.-F. Pai, Y. Li, H. W. Tseng, D. C. Ralph, and R. A. Buhrman, Spin-torque switching with the giant spin Hall effect of Tantalum. Science **336**, 555–558 (2012).

[44] T. Jungwirth, J. Wunderlich, and K. Olejník, Spin Hall effect devices. Nat. Mater. **11**, 382 (2012).

[45] A. Hoffmann, Spin Hall effects in metals. IEEE Trans. Magn. **49**, 5172–5193 (2013).

[46] A. A. Thiele, Steady-state motion of magnetic domains. Phys. Rev. Lett. **30**, 230–233 (1973).

[47] S.-Z. Lin, Edge instability in a chiral stripe domain under an electric current and skyrmion generation. Phys. Rev. B **94**, 020402 (2016).

[48] X. Zhang, Y. Zhou, and M. Ezawa, Magnetic bilayer-skyrmions without skyrmion Hall effect. Nat. Commun. **7**, 10293 (2016).

[49] X. Zhang, J. Xia, G. P. Zhao, X. Liu, and Y. Zhou, Magnetic skyrmion transport in a nanotrack with spatially varying damping and non-adiabatic torque. IEEE Trans. Magn. **53**, 1-6 (2017).

[50] S. Zhang, and Z. Li, Roles of nonequilibrium conduction electrons on the magnetization dynamics of ferromagnets. Phys. Rev. Lett. **93**, 127204 (2004).

[51] T. Schulz, R. Ritz, A. Bauer, M. Halder, M. Wagner, C. Franz, C. Pfleiderer, K. Everschor, M. Garst, and A. Rosch, Emergent electrodynamics of skyrmions in a chiral magnet. Nat. Phys. **8**, 301–304 (2012).

[52] K. Everschor, M. Garst, R. A. Duine, and A. Rosch, Current-induced rotational torques in the skyrmion lattice phase of chiral magnets. Phys. Rev. B **84**, 064401 (2011).

[53] K. Everschor, M. Garst, B. Binz, F. Jonietz, S. Mühlbauer, C. Pfleiderer, and A. Rosch, Rotating skyrmion lattices by spin torques and field or temperature gradients. Phys. Rev. B **86**, 054432 (2012).

CHAPTER 4

Driving magnetic skyrmions with spin currents

In this chapter, using micromagnetic simulations and Thiele equation approach, we study the dynamic properties of a magnetic skyrmion driven by the spin-polarized current in conventional FM nanotracks, including monolayers, bilayers, and multilayers. Besides, we investigate the novel skyrmion dynamics in a magnetic monolayer with frustrated exchange interactions.

4.1 Introduction

As introduced in Ch. 3, the magnetic skyrmion is a nanoscale magnetic spin texture, which could be used to carry digital binary information [1, 2]. In principle, the binary information, i.e., "1" and "0", can be encoded by the presence or absence of an isolated skyrmion. For example, in a FM background, the presence of an isolated skyrmion stands for the binary bit "1", and the presence of a certain area with the uniform FM state stands for the binary bit "0". In some special cases [3, 4, 5, 6], the binary information can also be encoded by the skyrmion helicity or vorticity (cf. Ch. 3.1). For example, in a FM background, the Bloch-type skyrmion with a helicity of $\pi/2$ stands for the binary bit "1", and the Bloch-type skyrmion with a helicity of $3\pi/2$ stands for the binary bit "0". No matter how the information is stored, in any future information processing applications where information are carried by skyrmions, the delivery of skyrmions in a controlled manner is the key function that needs to be realized at first.

Theoretically, a promising feature of the skyrmion is that it can be driven into motion by a tiny external force [7, 8, 9, 10], which means the delivery of skyrmions may be realized in an energy-efficient fashion. There are several possible external forces that can be used to drive the skyrmion, which includes the spin-polarized current [1, 2, 11, 12, 13, 14], spin

wave [15, 16, 17], magnetic field gradient [18], thermal gradient [19], and so on. Within these different methods, the spin-polarized current appears to be an important mechanism and mature technique for effectively controlling the spin dynamics of traditional magnetic domain walls and skyrmions, which allows device scaling down to a few micrometers or even smaller. Besides, it has been reported that the threshold current density required for driving a skyrmion into motion is much smaller than that for driving a traditional magnetic domain wall [7, 8, 9, 10]. Thus, the magnetic and spintronic devices based on skyrmions could have a lower energy consumption compared to the devices based on traditional magnetic domain walls. For the above reasons, and from the application point of view, the understanding of skyrmion dynamics in nanostructures driven by the spin-polarized current is of great importance.

In this chapter, for the purpose of developing skyrmion-based information processing applications, we study the skyrmion motion in different FM nanostructures driven by different types of spin-polarized currents. We also investigate the novel current-driven dynamics of skyrmions in a frustrated magnetic thin film system.

4.2 Skyrmion dynamics in a monolayer nanotrack

The reliable transport of skyrmions in a nanotrack is a prerequisite for building the information delivery channel for skyrmion-based spintronic devices. In the following, under the framework of micromagnetics (cf. Ch. 2), we study the motion of a single isolated skyrmion in a FM monolayer nanotrack driven by the spin-polarized current. The FM monolayer nanotrack (e.g., Fe, Co, CoFeB, etc.) is coupled to a heavy metal substrate layer (e.g., Ta, Ir, Pt, etc.) with strong spin-orbit interaction, where the DMI is induced at the ferromagnet/heavy metal interface. Note that the skyrmion studied in this dissertation is assumed to be stabilized by the interface-induced DMI (cf. Ch. 2 and Ch. 3).

First, as shown in Fig. 4.1, there are two spin-polarized current injection geometries for driving the magnetic spin dynamics in such a FM monolayer nanotrack, namely, the

Table 4.1: The default intrinsic magnetic parameters for the micromagnetic simulation of the skyrmion dynamics in the FM monolayer nanotrack. The Heisenberg exchange constant, DMI constant, PMA constant, saturation magnetization, Gilbert gyromagnetic ratio, and damping coefficient are denoted by A, D, K, M_S, γ_0, and α, respectively.

A (J m^{-1})	D (J m^{-2})	K (J m^{-3})	M_S (A m^{-1})	γ_0 (m A^{-1} s^{-1})	α
15×10^{-12}	3×10^{-3}	0.8×10^{6}	580×10^{3}	2.211×10^{5}	0.3

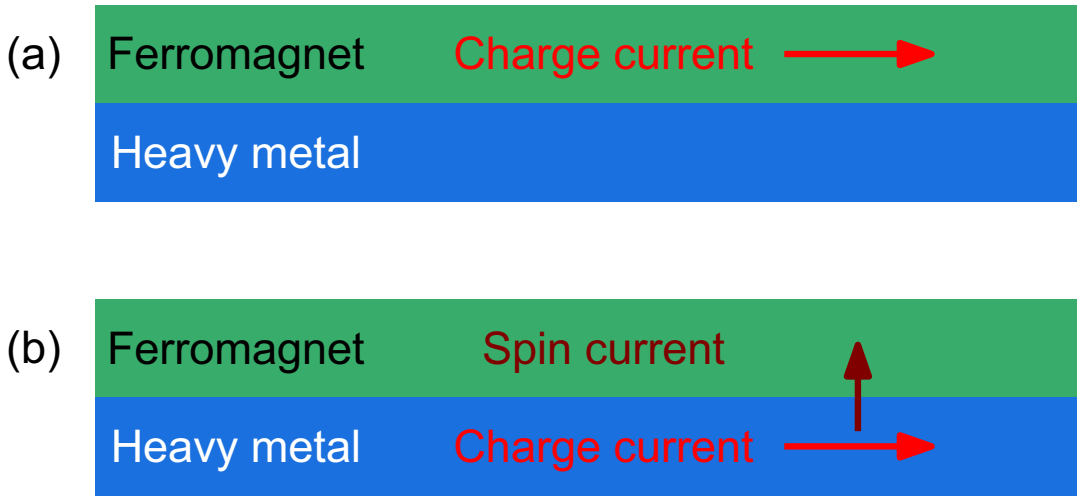

Figure 4.1: Schematics of the CIP and CPP geometries of the spin current injection for the FM monolayer nanotrack. (a) The CIP geometry. The charge current flows toward the right direction in the FM nanotrack, i.e., the corresponding electron current (spin-polarized current) flows toward the left direction in the FM nanotrack. The skyrmion motion is driven by the in-plane spin current. (b) The CPP geometry. The charge current flows through the heavy-metal substrate toward the right direction, which gives rise to a spin-polarized current perpendicularly injected to the FM nanotrack due to the SHE. The skyrmion motion is driven by the vertical spin current. In both cases, the FM nanotrack is coupled to the heavy-metal substrate, where the DMI is induced at the interface.

CIP and CPP geometries. For the CIP geometry, the charge current is directly injected into the FM nanotrack, which flows toward the right direction, i.e., the corresponding electrons flow toward the left direction, producing a spin current. The angular momentum of the spin current is transferred from itinerant conduction electrons to the magnetic moment of skyrmion, which generates the STT effect and drives the skyrmion into motion. For the CPP geometry, the charge current is directly injected into the heavy metal substrate, which flows toward the right direction, i.e., the corresponding electrons flow toward the left direction. Due to the SHE in the heavy metal, the charge current will be converted into a spin current propagating to the FM nanotrack perpendicularly. Thus, the spin current will globally exert on the magnetic spins in the FM nanotrack, and gives rise to the STT effect that could drive the skyrmion motion.

We first focus on the skyrmion motion in the FM monolayer nanotrack with the CIP geometry, i.e., the skyrmion motion is driven by the in-plane spin current. The simulation model is a FM nanotrack with the length l and the width w, where the thickness is fixed at 1 nm. The simulation is carried out by using the standard micromagnetic simulator, i.e., the 1.2 alpha 5 release of the OOMMF [24], where the model is discretized into tetragonal

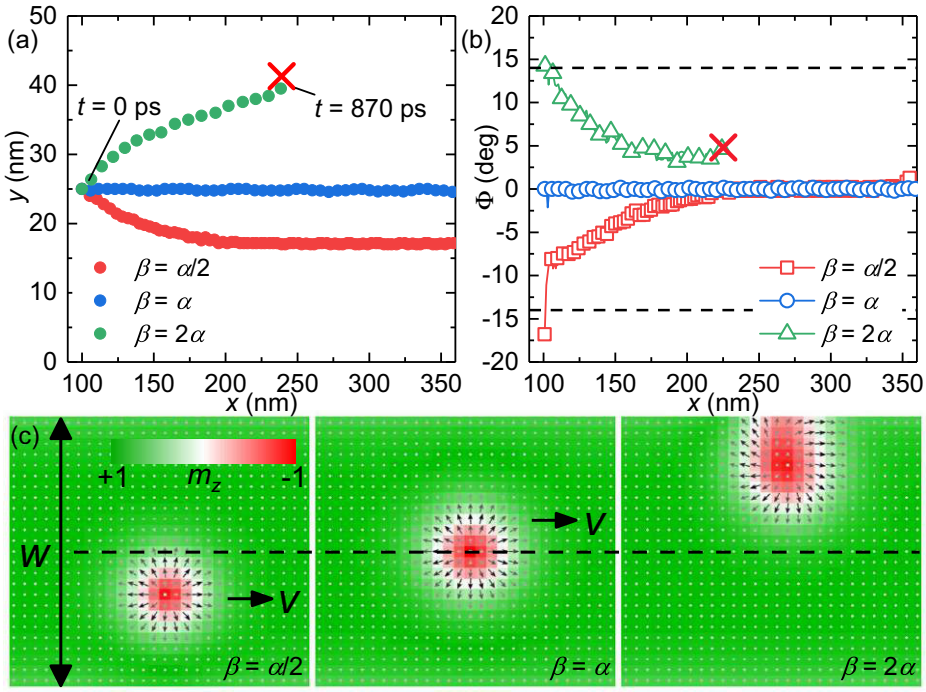

Figure 4.2: The motion of a skyrmion in a FM monolayer nanotrack driven by the in-plane spin current. (a) The trajectories of skyrmions with $\beta = \alpha/2 = 0.15$, $\beta = \alpha = 0.3$, and $\beta = 2\alpha = 0.6$. Dot denotes the skyrmion center. Red cross indicates the skyrmion destruction. (b) The skyrmion Hall angle Φ as a function of x for skyrmion motion with $\beta = \alpha/2 = 0.15$, $\beta = \alpha = 0.3$, and $\beta = 2\alpha = 0.6$. The dashed lines indicate $\Phi = \pm 14°$. (c) The real-space top-views of skyrmion motion with $\beta = \alpha/2 = 0.15$, $\beta = \alpha = 0.3$, and $\beta = 2\alpha = 0.6$. w and v denote the nanotrack width and velocity direction, respectively. The dashed line indicates the central line of the nanotrack. The skyrmion is destroyed at $t = 870$ ps when $\beta = 2\alpha = 0.6$. The out-of-plane magnetization component m_z is represented by the green-white-red color scale. Adapted with permission from the author's original work [20].

volume elements with the size of 2 nm × 2 nm × 1 nm. The magnetic spin dynamics is governed by the LLG equation augmented with the adiabatic and non-adiabatic STTs (cf. Ch. 2)

$$\begin{aligned}\frac{d\boldsymbol{M}}{dt} =& -\gamma_0 \boldsymbol{M} \times \boldsymbol{H}_{\text{eff}} + \frac{\alpha}{M_{\text{S}}}(\boldsymbol{M} \times \frac{d\boldsymbol{M}}{dt}) \\ &+ \frac{u}{M_{\text{S}}^2}(\boldsymbol{M} \times \frac{\partial \boldsymbol{M}}{\partial x} \times \boldsymbol{M}) - \frac{\beta u}{M_{\text{S}}}(\boldsymbol{M} \times \frac{\partial \boldsymbol{M}}{\partial x}),\end{aligned} \tag{4.1}$$

where $\boldsymbol{M}$ is the magnetization, M_{S} is the saturation magnetization, t is the time, γ_0 is the Gilbert gyromagnetic ratio, α is the Gilbert damping coefficient, and β is the strength of the non-adiabatic STT. The adiabatic STT coefficient is given by u, i.e., the conduction electron velocity. The value of u can be calculated from $u = |\frac{\gamma_0 \hbar}{\mu_0 e}| \frac{jP}{2M_{\text{S}}}$ with the spin polarization

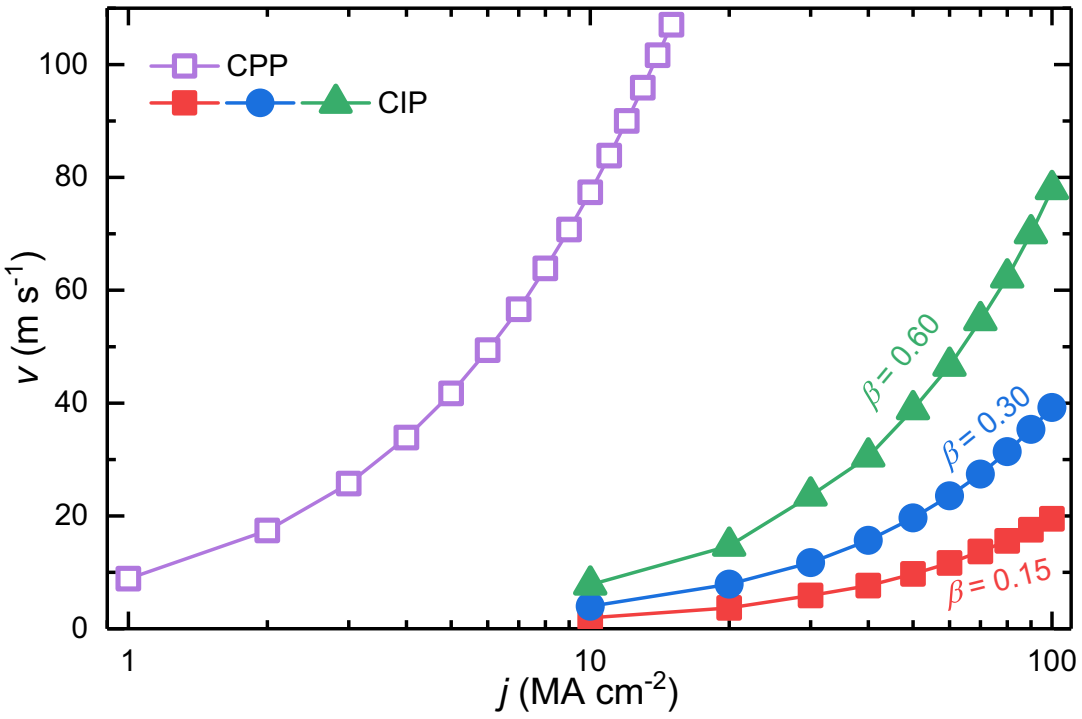

Figure 4.3: The steady-state current-velocity relation of the skyrmion motion in FM monolayer nanotracks with the CPP and CIP geometries. Here, $l = 1000$ nm, $w = 150$ nm, and $D = 3.5$ mJ m^{-2}. Other parameters are given in Table 4.1. The velocity v at different driving current density j is measured when steady motion is attained, i.e., the skyrmion is moving along the longitudinal direction of the nanotrack. Note that the skyrmion driven by the vertical spin current will be destroyed when j is larger than 17 MA cm^{-2}. Adapted with permission from the author's original work [21].

rate P (cf. Ch. 2). The default value of P is assumed to be 0.4 in this dissertation unless otherwise specifically defined. The effective field $\boldsymbol{H}_{\text{eff}}$ is expressed as

$$\boldsymbol{H}_{\text{eff}} = -\mu_0^{-1}\frac{\partial \varepsilon}{\partial \boldsymbol{M}}, \tag{4.2}$$

where μ_0 is the vacuum permeability constant. The average energy density ε contains the exchange, anisotropy, demagnetization, and DMI energies, which is given as

$$\begin{aligned}\varepsilon = A[\nabla(\frac{\boldsymbol{M}}{M_{\text{S}}})]^2 - K\frac{(\boldsymbol{n}\cdot\boldsymbol{M})^2}{M_{\text{S}}^2} - \frac{\mu_0}{2}\boldsymbol{M}\cdot\boldsymbol{H}_{\text{d}}(\boldsymbol{M}) \\ + \frac{D}{M_{\text{S}}^2}(M_z\frac{\partial M_x}{\partial x} + M_z\frac{\partial M_y}{\partial y} - M_x\frac{\partial M_z}{\partial x} - M_y\frac{\partial M_z}{\partial y}),\end{aligned} \tag{4.3}$$

where A, K, and D are the Heisenberg exchange, PMA, and DMI energy constants, respectively. $\boldsymbol{n}$ is the unit surface normal vector, and $\boldsymbol{H}_{\text{d}}(\boldsymbol{M})$ is the demagnetization field. M_x, M_y and M_z are the three Cartesian components of $\boldsymbol{M}$. The default intrinsic magnetic

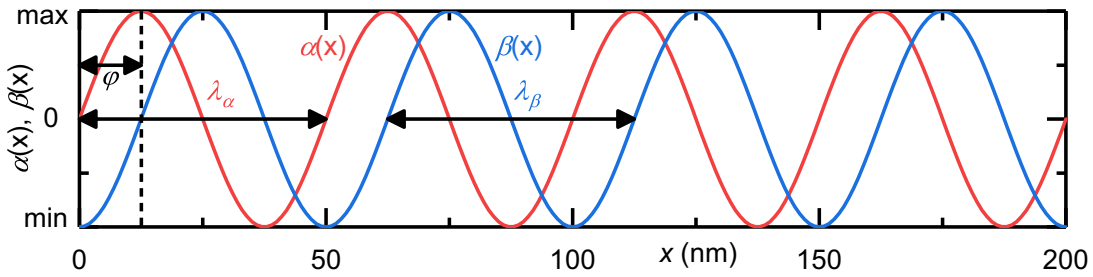

Figure 4.4: The damping coefficient $\alpha(x)$ and non-adiabatic STT coefficient $\beta(x)$ as functions of the longitudinal coordinate x in the FM monolayer nanotrack. Adapted with permission from the author's original work [20].

parameters used in the simulation are adopted from Refs. [1, 10], which are summarized in Table 4.1.

We first study the in-plane current-driven skyrmion motion in the FM monolayer nanotrack by assuming $u = 100$ m s^{-1}, $w = 50$ nm, and an isolated skyrmion is initially located at the position of $x = 100$ nm, $y = 25$ nm. As shown in Fig. 4.2(a), the skyrmion moves along the central line of the nanotrack when $\beta = \alpha = 0.3$. However, due to the SkHE (cf. Ch. 3), it shows a transverse shift toward the upper and lower edges when $\beta = 2\alpha = 0.6$ and $\beta = \alpha/2 = 0.15$, respectively. The skyrmion motion toward the nanotrack edge could ultimately result in the destruction of the skyrmion. For example, the skyrmion is destroyed by touching the upper edge when $\beta = 2\alpha = 0.6$ at $t = 870$ ps.

We recall that the definition of the skyrmion Hall angle Φ (cf. Ch. 3) is given as

$$\Phi = \tan^{-1}(v_y/v_x). \tag{4.4}$$

Figure 4.2(b) shows Φ as a function of x for the skyrmion motion with $\beta = \alpha/2 = 0.15$, $\beta = \alpha = 0.3$, and $\beta = 2\alpha = 0.6$. It can be seen that $\Phi = 0°$ when $\beta = \alpha = 0.3$, indicating the moving skyrmion has no transverse motion [cf. Fig. 4.2(c)]. When $\beta = \alpha/2 = 0.15$, Φ increases from $-15°$ to $0°$, indicating the moving skyrmion has a transverse shift toward the lower edge which is balanced by the transverse force due to the SkHE and the edge-skyrmion repulsive force [cf. Fig. 4.2(c)]. When $\beta = 2\alpha = 0.6$, Φ decreases from $15°$ to $3°$ within 870 ps, indicating the moving skyrmion shows a transverse motion toward the upper edge. At $t = 870$ ps, the skyrmion is destroyed as it touches the upper edge of the nanotrack [cf. Fig. 4.2(c)]. Note that the skyrmion profile is rigid before it touches the nanotrack edge. Therefore, it can be seen that for the skyrmion motion in the nanotrack with the CIP geometry, the SkHE depends on the ratio between the damping coefficient α and the strength of the non-adiabatic STT β.

As shown in Fig. 4.3, the steady-state skyrmion velocity in a FM monolayer nanotrack

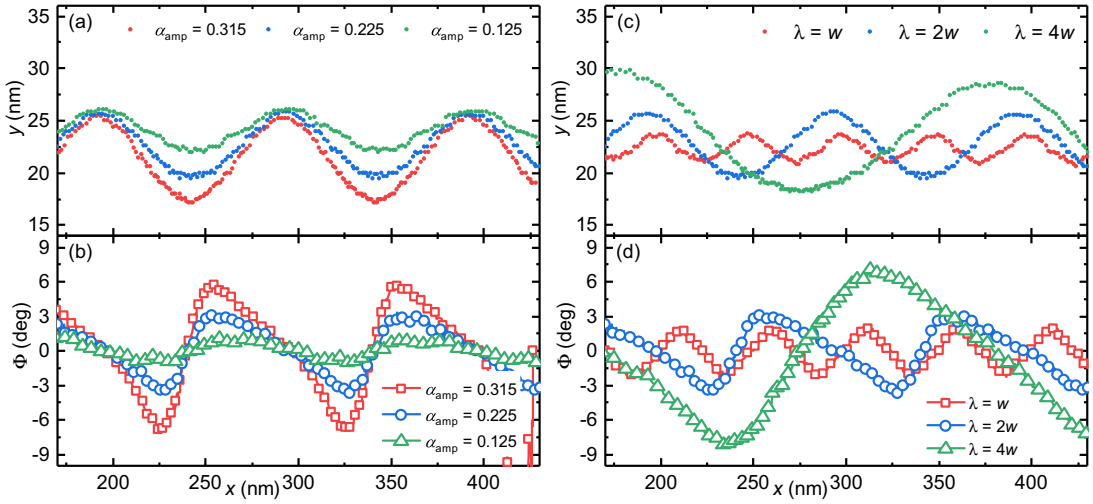

Figure 4.5: The motion of a skyrmion in a FM monolayer nanotrack with varying α driven by the in-plane spin current. (a) The trajectories of in-plane current-driven skyrmions with $\alpha_{\text{amp}} = 0.315, 0.225, 0.215$. $\lambda_\alpha = 2w$ and $\beta = 0.3$. (b) Φ as a function of x for skyrmion motion with $\alpha_{\text{amp}} = 0.315, 0.225, 0.215$. $\lambda_\alpha = 2w$ and $\beta = 0.3$. (c) The trajectories of in-plane current-driven skyrmions with $\lambda_\alpha = w, 2w, 4w$. $\alpha_{\text{amp}} = 0.225$ and $\beta = 0.3$. (d) Φ as a function of x for skyrmion motion with $\lambda_\alpha = w, 2w, 4w$. $\alpha_{\text{amp}} = 0.225$ and $\beta = 0.3$. Adapted with permission from the author's original work [20].

with the CIP geometry as a function of the driving current density j is numerically calculated for different strengths of the non-adiabatic STT β. It shows the skyrmion velocity is proportional to j at a given β. The skyrmion velocity at a given j also increases with increasing β. The skyrmion driven by the in-plane current of $j = 1 \times 10^{12}$ A m^{-1} moves along the nanotrack and reaches a steady velocity of $v \approx 20$ m s^{-1}, $v \approx 40$ m s^{-1}, and $v \approx 80$ m s^{-1}, for $\beta = \alpha/2 = 0.15$, $\beta = \alpha = 0.3$, and $\beta = 2\alpha = 0.6$, respectively.

As discussed in Ch. 3, for the in-plane current-driven skyrmion motion, the transverse motion caused by the SkHE can be analytically analyzed using the Thiele equation (cf. Appendix A) by assuming that a rigid skyrmion moves in an infinite monolayer film, which is expressed as

$$\boldsymbol{G} \times (\boldsymbol{v} - \boldsymbol{u}) + \boldsymbol{\mathcal{D}} (\beta \boldsymbol{u} - \alpha \boldsymbol{v}) = \boldsymbol{0}, \tag{4.5}$$

where the velocity solutions are given as

$$v_x = u \frac{(\alpha\beta + 1)}{\alpha^2 + 1}, \quad v_y = u \frac{(\beta - \alpha)}{\alpha^2 + 1}. \tag{4.6}$$

Accordingly, the skyrmion Hall angle solution is given as

$$\Phi = \tan^{-1}(v_y / v_x) = \tan^{-1}\left(\frac{\beta - \alpha}{\alpha\beta + 1}\right). \tag{4.7}$$

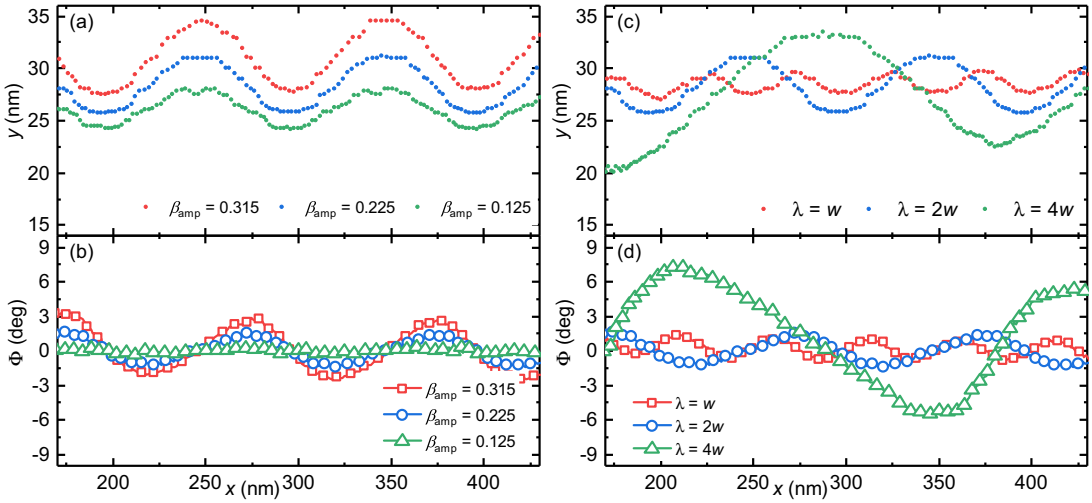

Figure 4.6: The motion of a skyrmion in a FM monolayer nanotrack with varying β driven by the in-plane spin current. (a) The trajectories of in-plane current-driven skyrmions with $\beta_{\text{amp}} = 0.315, 0.225, 0.215$. $\lambda_\beta = 2w$, $\varphi = 0$, and $\alpha = 0.3$. (b) Φ as a function of x for skyrmion motion with $\beta_{\text{amp}} = 0.315, 0.225, 0.215$. $\lambda_\beta = 2w$, $\varphi = 0$, and $\alpha = 0.3$. (c) The trajectories of in-plane current-driven skyrmions with $\lambda_\beta = w, 2w, 4w$. $\beta_{\text{amp}} = 0.225$, $\varphi = 0$, and $\alpha = 0.3$. (d) Φ as a function of x for skyrmion motion with $\lambda_\beta = w, 2w, 4w$. $\beta_{\text{amp}} = 0.225$, $\varphi = 0$, and $\alpha = 0.3$. Adapted with permission from the author's original work [20].

Here, in order to further understand the steady-state motion of the skyrmion in the FM monolayer nanotrack with the CIP geometry, we add an external force term $\boldsymbol{F}$ into the Thiele equation (cf. Appendix A) mimicking the boundary effect, where we also assume the skyrmion is rigid in the steady motion. The modified Thiele motion equation is expressed as follows

$$\boldsymbol{G} \times (\boldsymbol{v} - \boldsymbol{u}) + \boldsymbol{\mathcal{D}} (\beta \boldsymbol{u} - \alpha \boldsymbol{v}) + \boldsymbol{F} = \boldsymbol{0}, \tag{4.8}$$

where $\boldsymbol{v} = (v_x, v_y)$ is the steady velocity of the skyrmion, and $\boldsymbol{u} = (u, 0)$ is determined by the driving current j as mentioned above. For a skyrmion moving along the longitudinal direction of the nanotrack, we have two relations hold directly for the steady state: $v_y = 0$ and $F_x = 0$ (cf. Appendix A and Refs. [10, 11]). Hence, from Eq. 4.8 we find

$$v_x = \frac{\beta u}{\alpha}, \quad v_y = 0. \tag{4.9}$$

Note that for the steady-state motion of a skyrmion, its transverse shift due to the SkHE is balanced by the skyrmion-edge repulsive force. Thus, it is natural that the skyrmion Hall angle $\Phi = 0$ for the steady-state motion of the skyrmion in the nanotrack. It can be seen that the numerical results of the current-velocity relation for the skyrmion motion in the

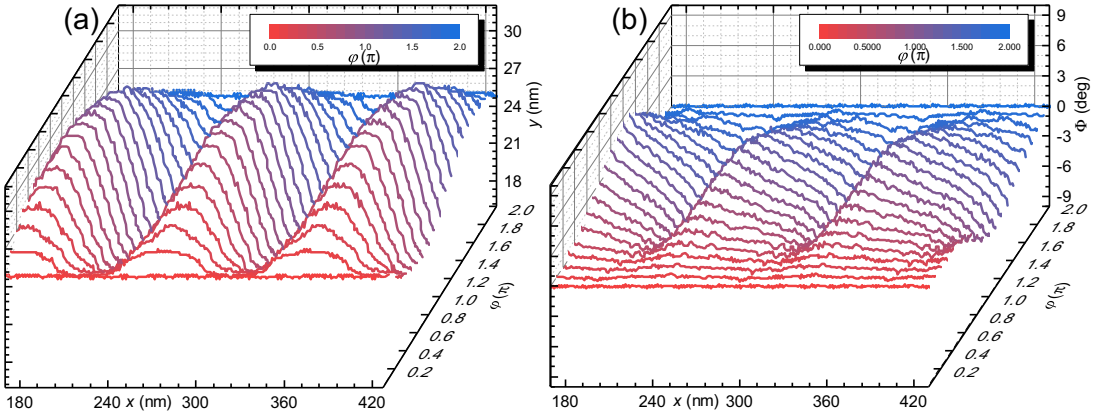

Figure 4.7: The motion of a skyrmion in a FM monolayer nanotrack with varying α and β driven by the in-plane spin current. (a) The trajectories of in-plane current-driven skyrmions with $\varphi = 0 \sim 2\pi$. $\alpha_{\text{amp}} = \beta_{\text{amp}} = 0.225$ and $\lambda_\alpha = \lambda_\beta = 2w$. (b) Φ as a function of x for skyrmion motion with $\varphi = 0 \sim 2\pi$. $\alpha_{\text{amp}} = \beta_{\text{amp}} = 0.225$ and $\lambda_\alpha = \lambda_\beta = 2w$. Adapted with permission from the author's original work [20].

nanotrack with the CIP geometry, as given in Fig. 4.3, are in a good agreement and can be well described by Eq. 4.9.

Based on Eq. 4.9 and numerical results in Fig. 4.3, it can be seen that a larger β-to-α ratio can result in a faster motion of the skyrmion in the nanotrack at a given j. Namely, a large β/α is good for the fast information delivery and processing. However, based on Eq. 4.7 and numerical results in Fig. 4.2, it can be seen that the motion of a skyrmion with a large velocity may lead to its destruction at the nanotrack edge due to the SkHE, unless the SkHE is eliminated for $\alpha = \beta$. Because it is difficult to find FM materials with exact $\alpha = \beta$, it is necessary to find alternative ways to avoid the skyrmion destruction during the skyrmion motion in the nanotrack.

In the following, we propose and demonstrate that a FM monolayer nanotrack with spatially sinusoidally varying α and/or β can be designed for transporting skyrmions in a sinusoidal manner, where the destruction of skyrmion due to the SkHE can be avoided effectively. The spatially varying α can be achieved by gradient doping of lanthanides impurities in ferromagnets [25, 26, 27]. As experiments have found that α is dependent on the interface [28], it is also realistic to construct the varying α by techniques such as interface engineering. Indeed, as shown in Ref. [29], local control of α in a FM/nonmagnetic thin-film bilayer has been experimentally demonstrated by interfacial intermixing induced by focused ion-beam irradiation. On the other hand, because that the value of β depends on the material properties [30], it is expected to realize the spatial varying β by constructing a super-lattice nanotrack using different materials, similar to the model proposed in Ref. [30].

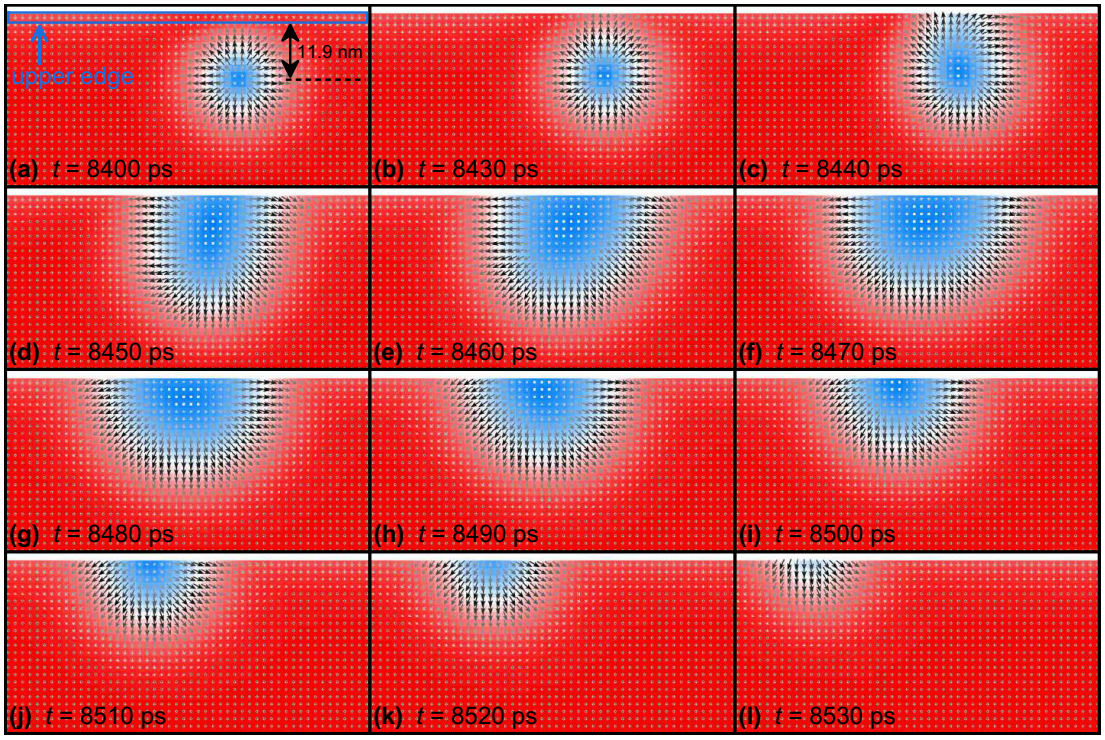

Figure 4.8: Snapshots of the destruction process of a skyrmion due to the SkHE in a FM monolayer nanotrack driven by the vertical spin current at selected times. Here, the driving current density $j = 5 \times 10^{10}$ A m^{-2}. The given nanotrack size is set as 1000 nm $\times$ 40 nm $\times$ 0.4 nm with $D = 3.0$ mJ m^{-2}. The color denotes the out-of-plane magnetization component m_z, i.e., blue for spins pointing into the plane, red for spins pointing out of the plane, white for spins pointing in the plane. Adapted with permission from the author's original work [22].

As depicted in Fig. 4.4, we define the Gilbert damping coefficient α in Eq. 4.1 as a function of the longitudinal coordinate x as follows

$$\alpha(x) = \alpha_{\text{amp}} \cdot \{1 + \sin[2\pi(x/\lambda_\alpha)]\} + \alpha_{\text{min}}, \tag{4.10}$$

where $\alpha_{\text{amp}} = (\alpha_{\text{max}} - \alpha_{\text{min}})/2$ is the amplitude of the α function. α_{max} and α_{min} stand for the maximum and minimum values of the α function, respectively. λ_α denotes the wavelength of the α function. In a similar way, we define the non-adiabatic STT coefficient β in Eq. 4.1 as a function of the longitudinal coordinate x as follows (cf. Fig. 4.4)

$$\beta(x) = \beta_{\text{amp}} \cdot \{1 + \sin[2\pi(x/\lambda_\beta) - \varphi]\} + \beta_{\text{min}}, \tag{4.11}$$

where $\beta_{\text{amp}} = (\beta_{\text{max}} - \beta_{\text{min}})/2$ is the amplitude of the β function. β_{max} and β_{min} stand for the maximum and minimum values of the β function, respectively. λ_β and φ denote the wavelength and phase of the β function, respectively.

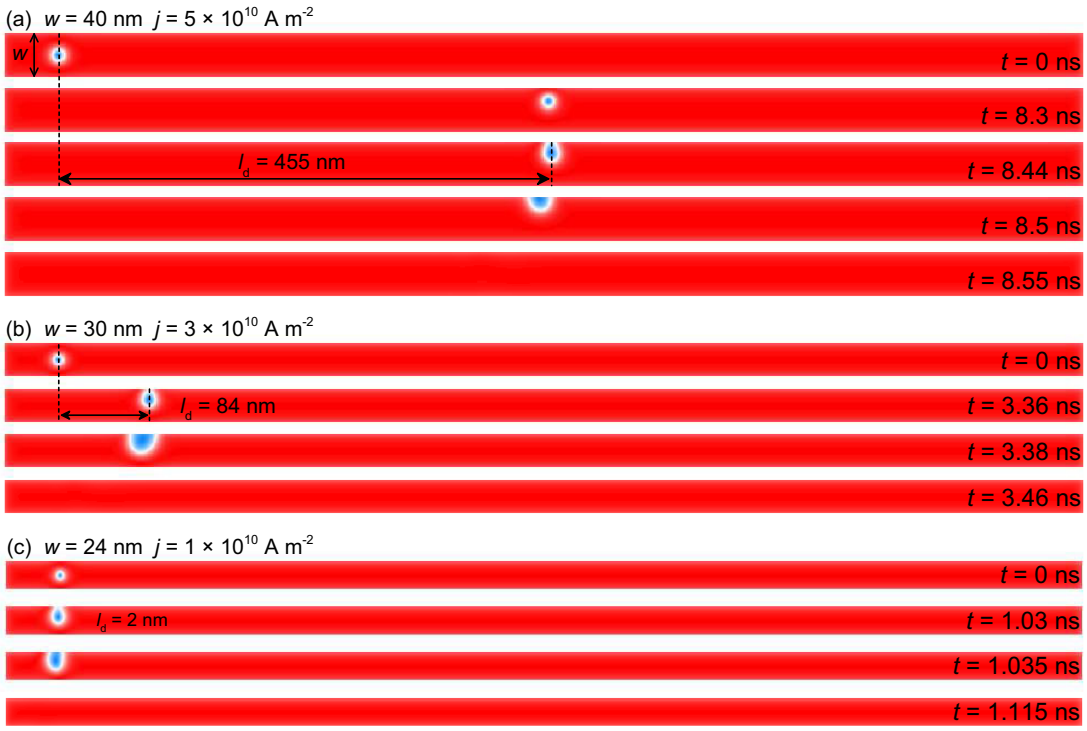

Figure 4.9: The motion driven by the vertical spin current and destruction of a skyrmion in FM monolayer nanotracks with different track width w. Here, the given nanotrack size is set as 1000 nm $\times$ w nm $\times$ 0.4 nm. l_{d} represents the horizontal distance between the position where the skyrmion is destroyed and the initial position of the skyrmion. The color denotes the out-of-plane magnetization component m_z, i.e., blue for spins pointing into the plane, red for spins pointing out of the plane, white for spins pointing in the plane. Adapted with permission from the author's original work [22].

We first demonstrate the in-plane current-driven skyrmion motion in a FM monolayer nanotrack with spatially varying α and spatially uniform β, i.e., α is a function of x, as in Eq. 4.10, and $\beta = 0.3$. Figure 4.5(a) shows the trajectories of the in-plane current-driven skyrmions with different $\alpha(x)$ functions where $\lambda_\alpha = 2w$ and $\beta = 0.3$. For $\alpha_{\mathrm{max}} = 0.75$, $\alpha_{\mathrm{min}} = 0.12$, i.e., $\alpha_{\mathrm{amp}} = 0.315$, the skyrmion moves in the rightward direction in a sinusoidal pattern. For $\alpha_{\mathrm{max}} = 0.6$, $\alpha_{\mathrm{min}} = 0.15$, i.e., $\alpha_{\mathrm{amp}} = 0.225$, the maximum transverse shift of skyrmion is reduced in compared to that of $\alpha_{\mathrm{amp}} = 0.315$. For $\alpha_{\mathrm{max}} = 0.45$, $\alpha_{\mathrm{min}} = 0.2$, i.e., $\alpha_{\mathrm{amp}} = 0.125$, the amplitude of the skyrmion trajectory further decreases. Φ as a function of x corresponding to Fig. 4.5(a) for different $\alpha(x)$ functions are given in Fig. 4.5(b). Figure 4.5(c) shows the trajectories of the in-plane current-driven skyrmions with different λ_α where $\alpha_{\mathrm{amp}} = 0.225$ and $\beta = 0.3$. Φ as a function of x corresponding to Fig. 4.5(c) for different λ_α are given in Fig. 4.5(d).

We then investigate the in-plane current-driven skyrmion motion in a FM monolayer

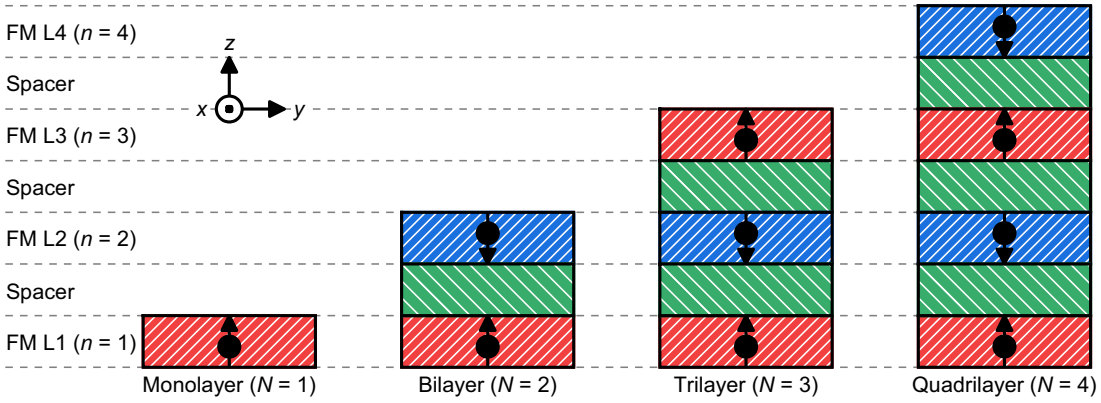

Figure 4.10: Schematics of the simulation models including the FM monolayer ($N = 1$), SyAF bilayer ($N = 2$), SyAF trilayer ($N = 3$) and SyAF quadrilayer ($N = 4$) nanotracks. The length along the x-axis, width along the y-axis, and thickness along the z-axis of each FM layer and nonmagnetic spacer are respectively equal to 500 nm, 50 nm and 1 nm, where the FM layer L1 is placed on the heavy-metal substrate. In the SyAF nanotracks, the adjacent FM layers are antiferromagnetically exchange-coupled through their respective ferromagnet/spacer/ferromagnet interfaces. The initial magnetization configurations of FM layers L1 ($n = 1$) and L3 ($n = 3$) are pointing along the $+z$-direction, while those of FM layers L2 ($n = 2$) and L4 ($n = 4$) are pointing along the $-z$-direction. The arrows represent the initial magnetization directions. Adapted with permission from the author's original work [23].

nanotrack with spatially uniform α and spatially varying β, i.e., β is a function of x, as in Eq. 4.11, and $\alpha = 0.3$. Figure 4.6(a) shows the trajectories of the in-plane current-driven skyrmions with different $\beta(x)$ functions where $\lambda_\beta = 2w$, $\varphi = 0$ and $\alpha = 0.3$. The results are similar to the case with spatially varying α. For $\beta_{\text{max}} = 0.75$, $\beta_{\text{min}} = 0.12$, i.e., $\beta_{\text{amp}} = 0.315$, the skyrmion moves in the rightward direction in a sinusoidal pattern. For $\beta_{\text{max}} = 0.6$, $\beta_{\text{min}} = 0.15$, i.e., $\beta_{\text{amp}} = 0.225$, the maximum transverse shift of skyrmion is reduced in compared to that of $\beta_{\text{amp}} = 0.315$. For $\beta_{\text{max}} = 0.45$, $\beta_{\text{min}} = 0.2$, i.e., $\beta_{\text{amp}} = 0.125$, the amplitude of the skyrmion trajectory further decreases. Φ as a function of x corresponding to Fig. 4.6(a) for different $\beta(x)$ functions are given in Fig. 4.6(b). Figure 4.6(c) shows the trajectories of the in-plane current-driven skyrmions with different λ_β where $\beta_{\text{amp}} = 0.225$ and $\alpha = 0.3$. Φ as a function of x corresponding to Fig. 4.6(c) for different λ_β are given in Fig. 4.6(d).

From the skyrmion motion with spatially varying α or spatially varying β, it can be seen that the amplitude of trajectory is proportional to α_{amp} or β_{amp}. The wavelength of trajectory is equal to $\lambda_{\alpha,\beta}$, while the amplitude of trajectory is proportional to $\lambda_{\alpha,\beta}$. Φ also varies with x in a quasi-sinusoidal manner, where the peak value of $\Phi(x)$ is proportional to α_{amp}, β_{amp}, and $\lambda_{\alpha,\beta}$. As shown in Fig. 3.5(c), when β is fixed at a value between α_{max}

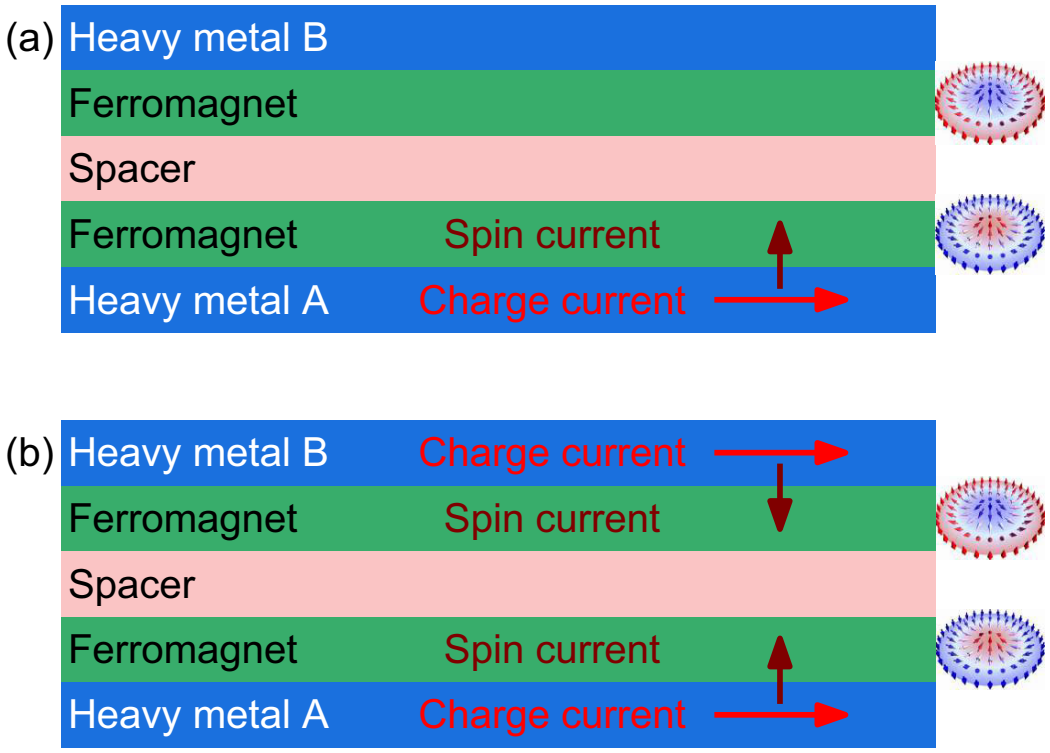

Figure 4.11: Schematics of the vertical spin current injection geometries for the SyAF bilayer nanotrack. (a) The confined CPP geometry, where the charge current flows through the heavy-metal substrate layer A toward the right direction, which gives rise to a spin current perpendicularly injected to the bottom FM layer due to the SHE. (b) The unconfined CPP geometry, where the charge currents flow through both the heavy-metal substrate layers A and B toward the right direction, which give rise to spin currents perpendicularly injected to the top and bottom FM layers due to the SHE. Adapted with permission from the author's original work [23].

and α_{min}, larger α_{amp} will lead to larger peak value of $\Phi(x)$. On the other hand, a larger $\lambda_{\alpha,\beta}$ allows a longer time for the skyrmion transverse motion toward a certain direction due to the SkHE, which will result in a larger amplitude of trajectory as well as a larger peak value of $\Phi(x)$.

We also demonstrate the in-plane current-driven skyrmion motion in a FM monolayer nanotrack with both spatially varying α and β, i.e., both α and β are functions of x, as given in Eq. 4.10 and Eq. 4.11, respectively.

Figure 4.7(a) shows the trajectories of the in-plane current-driven skyrmions with spatially varying α and β where $\alpha_{\text{amp}} = \beta_{\text{amp}} = 0.225$ and $\lambda_\alpha = \lambda_\beta = 2w$. Here, we focus on the effect of the phase difference between the $\alpha(x)$ and $\beta(x)$ functions. For $\varphi = 0$ and

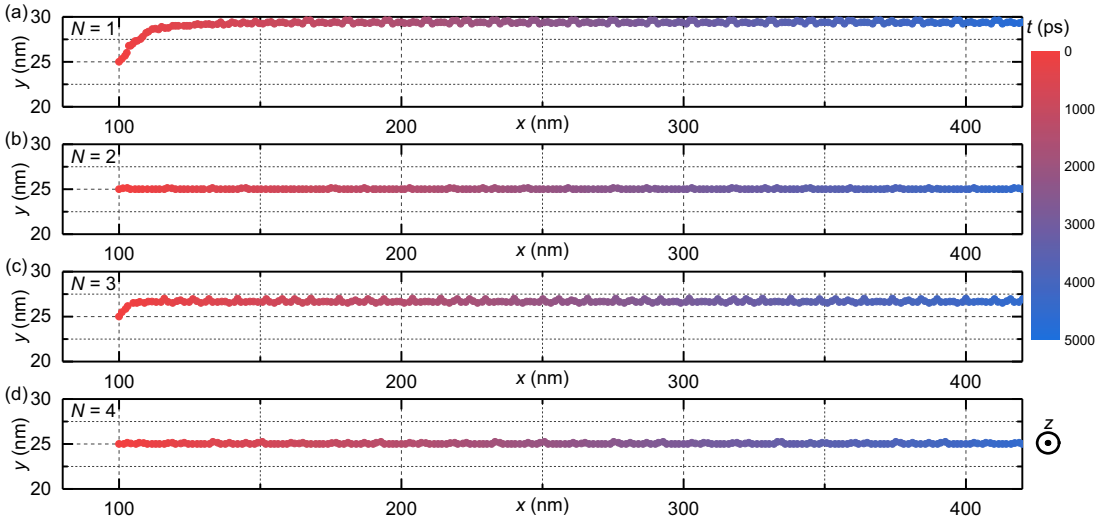

Figure 4.12: The typical trajectories of SyAF N-layer skyrmions in N-layer SyAF nanotracks. (a) The trajectory of a FM monolayer skyrmion in a monolayer FM nanotrack ($N = 1$) at $j = 10$ MA cm^{-2}. The transverse shift of the monolayer skyrmion due to the SkHE is obvious. It reaches a stable velocity of $v_x \sim 70$ m s^{-1}. (b) The trajectory of a SyAF bilayer skyrmion in a bilayer SyAF nanotrack ($N = 2$) at $j = 20$ MA cm^{-2}. The SyAF bilayer skyrmion moves along the central line ($y = 25$ nm) of the nanotrack, which reaches a stable velocity of $v_x \sim 70$ m s^{-1}. (c) The trajectory of a SyAF trilayer skyrmion in a trilayer SyAF nanotrack ($N = 3$) at $j = 30$ MA cm^{-2}. It reaches a stable velocity of $v_x \sim 70$ m s^{-1}. (d) The trajectory of a SyAF quadrilayer skyrmion in a quadrilayer SyAF nanotrack ($N = 4$) at $j = 40$ MA cm^{-2}. The SyAF quadrilayer skyrmion moves along the central line ($y = 25$ nm) of the nanotrack, which reaches a stable velocity of $v_x \sim 70$ m s^{-1}. The dot denotes the skyrmion center. The total simulation time is 5000 ps, which is indicated by the color scale. Adapted with permission from the author's original work [23].

$\varphi = 2\pi$, as the $\alpha(x)$ function is identical to the $\beta(x)$ function, the skyrmion moves along the central line of the nanotrack. For $0 < \varphi < 2\pi$, as $\alpha(x)$ could be different from $\beta(x)$ at a certain x, it is shown that the skyrmion moves toward the right direction in a sinusoidal pattern, where the phase of trajectory is subject to φ. Figure 4.7(b) shows Φ as a function of x corresponding to Fig. 4.7(a) for $\varphi = 0 \sim 2\pi$ where $\alpha_{\text{amp}} = \beta_{\text{amp}} = 0.225$ and $\lambda_\alpha = \lambda_\beta = 2w$. It shows that $\Phi = 0°$ when $\varphi = 0$ and $\varphi = 2\pi$, while it varies with x in a quasi-sinusoidal manner when $0 < \varphi < 2\pi$. The amplitude of trajectory as well as the peak value of $\Phi(x)$ reach their maximum values when $\varphi = \pi$.

In the above, we have studied the in-plane current-driven skyrmion motion in a FM monolayer nanotrack with the CIP geometry. For the nanotrack with $\alpha = \beta$, the skyrmion moves straight along the nanotrack. For the nanotrack with $\alpha \neq \beta$, the skyrmion moves along the nanotrack but shows a transverse shift due to the SkHE. Such a transverse shift may result in the destruction of the skyrmion at the nanotrack edge. In order to control the

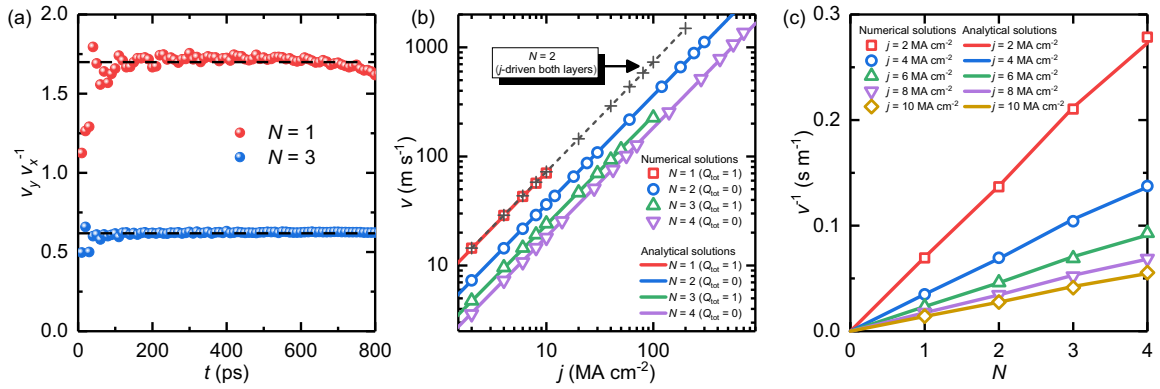

Figure 4.13: The steady-state current-velocity relation of the skyrmion motion in the FM monolayer and SyAF multilayer nanotracks driven by vertical spin currents. (a) The skyrmion Hall angle v_y/v_x as a function of t. It is almost a constant for $N = 1$ and $N = 3$. Here, we use a square sample of 200 nm $\times$ 200 nm $\times$ 1 nm in order to reduce the impact of the edge effect. The skyrmion is located at the film center (100 nm, 100 nm) at the initial time. (b) The velocity v as a function of j for the motion of SyAF N-layer skyrmions, where the driving current is injected into the bottom FM layer L1. When $j > 10$ MA cm^{-2} and $j > 100$ MA cm^{-2}, the moving FM monolayer and SyAF trilayer skyrmions are destroyed en-route caused by the SkHE, respectively. The open symbols stand for the numerical results. The solid lines represent the theoretical results given by Eq. 4.27 with $\alpha\mathcal{D} = 0.57$. The dashed line with cross symbol indicates the velocity v_x of a SyAF bilayer skyrmion in a bilayer SyAF nanotrack, where the driving current is injected into both the bottom FM layer L1 and the top FM layer L2. (c) The inverse velocity v_x^{-1} as a function of the total FM layer number N at small j, where no skyrmion is destroyed by the SkHE. The open symbols stand for the numerical results. The solid lines represent the theoretical results given by Eq. 4.27. Adapted with permission from the author's original work [23].

skyrmion motion and prevent the detrimental effect of the SkHE, we studied the skyrmion motion in the nanotrack with spatially sinusoidally varying α or β. The skyrmion moves on a sinusoidal trajectory, where the amplitude and wavelength of trajectory can be controlled by the spatial profiles of α and β. The peak value of $\Phi(x)$ is proportional to the amplitudes and wavelengths of $\alpha(x)$ and $\beta(x)$. Besides, we have demonstrated the in-plane current-driven skyrmion motion in the nanotrack having both spatially sinusoidally varying α and β with the same amplitude and wavelength. The skyrmion moves straight along the central line of the nanotrack when $\alpha(x)$ and $\beta(x)$ have no phase difference, i.e., $\varphi = 0$. When $\varphi \neq 0$, the skyrmion moves in a sinusoidal pattern, where the peak value of $\Phi(x)$ reaches its maximum value when $\varphi = \pi$. These results show the possibility to guide and control skyrmion motion in a FM monolayer nanotrack with the CIP geometry by constructing spatially varying parameters, which may enable reliable skyrmion transport in skyrmion-based information processing devices.

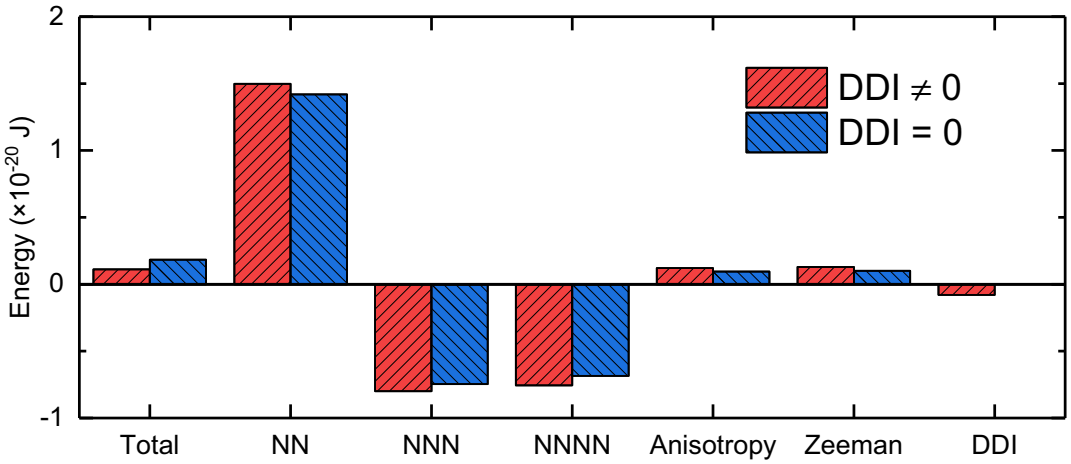

Figure 4.14: Details of the micromagnetic energy of a relaxed skyrmion with $(1, \pi/2)$ in the presence and absence of the DDI. The contribution from the DDI energy is found to be comparable to the anisotropy or Zeeman energy. The skyrmion energy is determined by the energy difference between the sample with a skyrmion and the sample without a skyrmion (i.e., with the FM state). Adapted with permission from the author's original work [6].

In the following, we continue to study the current-driven skyrmion motion in a FM monolayer nanotrack with the CPP geometry. The simulation model and parameters are identical to those used for the case of the CIP geometry (cf. Table 4.1), while the magnetic spin dynamics is governed by the extended LLG equation including the Slonczewski-like (damping-like) spin transfer torque, given as

$$\frac{d\boldsymbol{M}}{dt} = -\gamma_0 \boldsymbol{M} \times \boldsymbol{H}_{\text{eff}} + \frac{\alpha}{M_{\text{S}}}(\boldsymbol{M} \times \frac{d\boldsymbol{M}}{dt}) + \frac{u}{aM_{\text{S}}}(\boldsymbol{M} \times \boldsymbol{p} \times \boldsymbol{M}), \tag{4.12}$$

where $u = |\frac{\gamma_0 \hbar}{\mu_0 e}| \frac{j \theta_{\text{SH}}}{2M_{\text{S}}}$ is the STT coefficient, and $\boldsymbol{p} = -\hat{y}$ stands for the unit spin polarization direction. $\hbar$ is the reduced Planck constant, e is the electron charge, j is the applied current density, and θ_{SH} is the spin Hall angle. a denotes the thickness of the FM monolayer nanotrack. The effective field $\boldsymbol{H}_{\text{eff}}$ and associated average energy density ε are given in Eq. 4.2 and Eq. 4.3, respectively.

We first study the current-velocity relation of the skyrmion driven by the vertical spin current in the nanotrack with the CPP geometry (cf. Fig. 4.1). As shown in Fig. 4.3, the steady-state velocity of the skyrmion is proportional to the driving current density j. However, it is noteworthy that the skyrmion velocity in the CPP geometry at a given j is much larger than that in the CIP geometry. For example, at $j = 1 \times 10^{11}$ A m^{-2}, the skyrmion driven by the vertical spin current reaches a steady velocity of $v \approx 77$ m s^{-1}, while the skyrmion driven by the in-plane spin current only reaches a steady velocity of $v \approx 4$ m s^{-1} for $\alpha = \beta = 0.3$. It should be noted that the skyrmion driven by the vertical

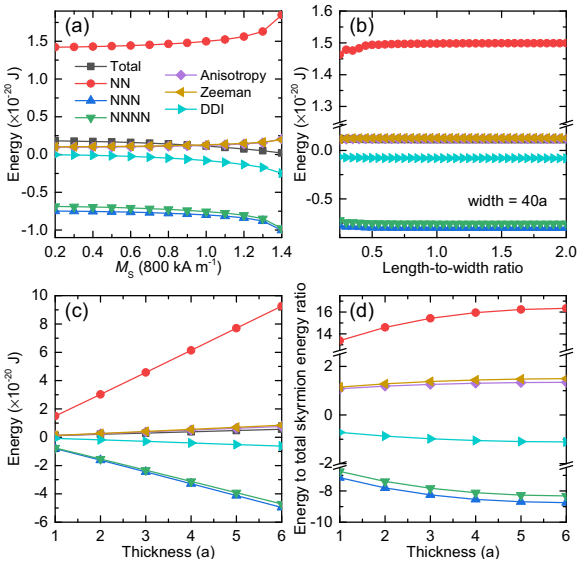

Figure 4.15: The energy of a skyrmion with $(1, \pi/2)$ as a function of material and geometric parameters. (a) The energy difference between the system with and without a skyrmion as a function of M_S of the magnetic film, of which the length, width, and thickness are fixed at $40a$, $40a$, and a, respectively. (b) The energy difference between the system with and without a skyrmion as a function of the length-to-width ratio of the magnetic film, of which the width and thickness are fixed at $40a$ and a, respectively. (c) The energy difference between the system with and without a skyrmion as a function of the thickness of the magnetic film, of which the length and width are fixed at $40a$. (d) The energy to total skyrmion energy ratio as a function of the thickness of the magnetic film, of which the length and width are fixed at $40a$. The black, red, blue, green, purple, yellow, and turquoise curves denote the differences of the total energy, NN exchange energy, NNN exchange energy, NNNN exchange energy, PMA energy, Zeeman energy, and DDI energy, respectively. Adapted with permission from the author's original work [6].

spin current also shows the SkHE, i.e., the transverse motion toward the nanotrack edge, before it reaches the steady-state motion in the nanotrack.

As discussed in Ch. 3, the skyrmion motion driven by the vertical spin current can be analytically analyzed using the Thiele equation (cf. Appendix A) by assuming the skyrmion is a rigid object and the boundary effect is excluded, which is written as

$$\boldsymbol{G} \times \boldsymbol{v} - \alpha \boldsymbol{\mathcal{D}} \cdot \boldsymbol{v} + 4\pi \boldsymbol{\mathcal{B}} \cdot \boldsymbol{j}_\mathrm{h} = \boldsymbol{0}, \tag{4.13}$$

where the velocity solutions for the CPP geometry with a spatially homogeneous charge current applied along the x direction are given as

$$v_x = \left| \frac{\gamma_0 \hbar}{\mu_0 e} \frac{\theta_\mathrm{sh} \mathcal{I}}{2aM_\mathrm{S}} \right| \cdot \frac{-\alpha \mathcal{D}}{Q^2 + \alpha^2 \mathcal{D}^2} \cdot j_x, \tag{4.14}$$

$$v_y = \left| \frac{\gamma_0 \hbar}{\mu_0 e} \frac{\theta_\mathrm{sh} \mathcal{I}}{2aM_\mathrm{S}} \right| \cdot \frac{Q}{Q^2 + \alpha^2 \mathcal{D}^2} \cdot j_x. \tag{4.15}$$

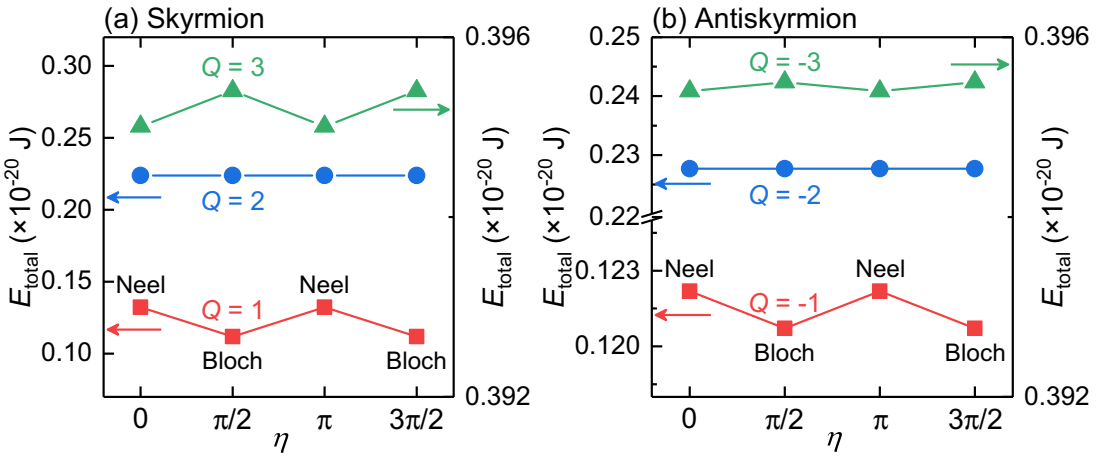

Figure 4.16: The total micromagnetic energy E_{total} for (a) relaxed skyrmions and (b) relaxed antiskyrmions as functions of Q and η. The lowest energy states are found to be two degenerate Bloch-type states both for the skyrmion ($Q = 1$) and the antiskyrmion ($Q = -1$) due to the DDI. Adapted with permission from the author's original work [6].

The corresponding skyrmion Hall angle is given as

$$\Phi_{\text{sk}} = \tan^{-1}\left(\frac{v_y}{v_x}\right) = \tan^{-1}\left(-\frac{Q}{\alpha\mathcal{D}}\right). \tag{4.16}$$

Here, for the purpose of understanding the steady-state motion of the skyrmion in the FM monolayer nanotrack with the CPP geometry, again, we add an external force term into the Thiele equation (cf. Appendix A), which accounts for the boundary effect in the nanotrack. The modified Thiele equation is written as follows

$$\boldsymbol{G} \times \boldsymbol{v} - \alpha\boldsymbol{\mathcal{D}} \cdot \boldsymbol{v} + 4\pi\boldsymbol{\mathcal{B}} \cdot \boldsymbol{j} + \boldsymbol{F} = \boldsymbol{0}, \tag{4.17}$$

where $\boldsymbol{v} = (v_x, v_y)$ is the steady velocity of the skyrmion, and $\boldsymbol{j} = (j, 0)$ is the driving current. $\boldsymbol{F}$ stands for the force exerted on the skyrmion by the edge of the nanotrack. For the situation that the skyrmion has reached the steady-state motion in the nanotrack, we have two relations hold directly: $v_y = 0$ and $F_x = 0$ (cf. Appendix A and Refs. [10, 11, 20]). Hence, from Eq. 4.17, for the CPP geometry we find

$$v_x = \frac{u\mathcal{I}_{xy}}{a\alpha\mathcal{D}_{xx}}, \quad v_y = 0. \tag{4.18}$$

Similar to the case of the CIP geometry, the transverse shift due to the SkHE is balanced by the skyrmion-edge repulsive force for the steady-state motion, i.e., $v_y = 0$. Thus, it is natural that the skyrmion Hall angle $\Phi = 0$ for the steady-state skyrmion motion. For the skyrmion in the given FM monolayer nanotrack, and according to the definitions of $\boldsymbol{\mathcal{D}}$ and $\boldsymbol{\mathcal{I}}$ (cf. Ch. 3), we find it has $\mathcal{D}_{xx} = \mathcal{D}_{yy} = 2$, $\mathcal{D}_{xy} = \mathcal{D}_{yx} = 0$, $\mathcal{I}_{xx} = \mathcal{I}_{yy} = 0$ and

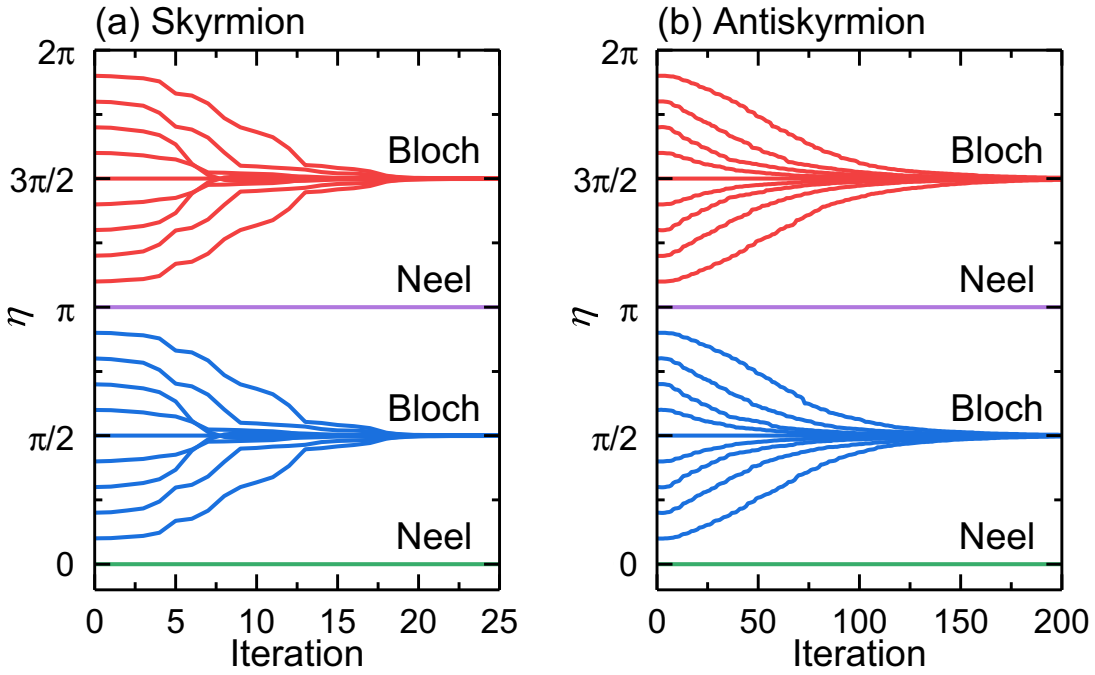

Figure 4.17: The helicity η as functions of the iteration for (a) skyrmions and (b) antiskyrmions with varied initial η. All of them are relaxed to the Bloch-type state unless they are initially in the Néel-type state. The model is a square element (11×11 spins) with the OBC. Here, $K = 0.1$ and $H_z = 0.1$. Adapted with permission from the author's original work [6].

$\mathcal{I}_{xy} = -\mathcal{I}_{yx} = 12a$. By substituting these parameters of the skyrmion into Eq. 4.18, we find the steady velocity of the skyrmion as

$$v_{x,\mathrm{sk}}^{\mathrm{CPP}} = \frac{6u}{\alpha}, \quad v_{y,\mathrm{sk}}^{\mathrm{CPP}} = 0. \tag{4.19}$$

It shows that the steady velocity of the skyrmion is inversely proportional to the damping coefficient α. By comparing Eq. 4.19 and Eq. 4.9, and considering the fact that the non-adiabatic STT strength β is ranged in $0 \sim 1$ [20], it can be seen that the steady skyrmion velocity in the CPP geometry is much larger than the steady skyrmion velocity in the CIP geometry at a certain value of α. Also, if we have $\alpha = \beta = 0.3$, the steady velocity of the skyrmion in the CIP geometry equals $v = v_x = u$, while the steady velocity in the CPP geometry is equal to $v = v_x = 20u$. Namely, the steady velocity in the CPP geometry is 20 times larger than that in the CIP geometry, which agrees well with numerical results, for example, at $j = 1 \times 10^{11}$ A m^{-2} and $\alpha = \beta = 0.3$ (cf. Fig. 4.3), the steady velocity in the CPP geometry $v \approx 77$ m s^{-1}, while in the CIP geometry $v \approx 4$ m s^{-1}.

On the other hand, although the vertical spin current-driven skyrmion in the CPP geometry moves faster than that in the CIP geometry at a given j, it could be destroyed due to the SkHE when its velocity reaches a certain threshold. The reason is that the Magnus

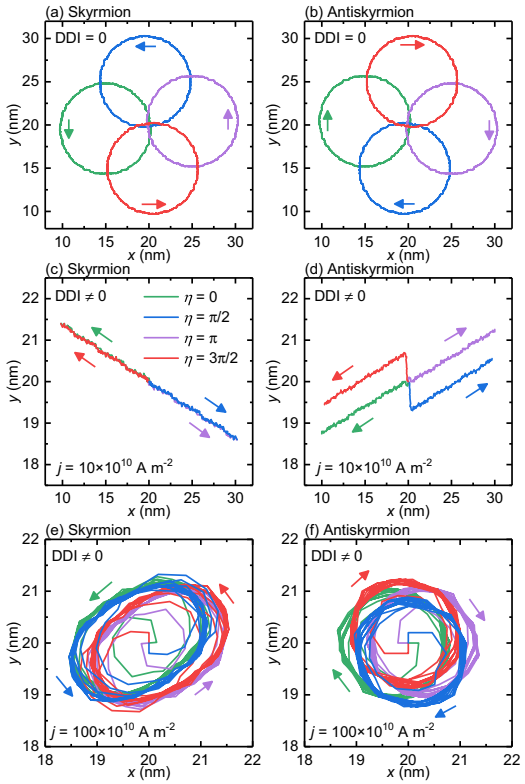

Figure 4.18: The trajectories of skyrmions and antiskyrmions in a frustrated J_1-J_2-J_3 FM thin film. Trajectories of (a) skyrmions and (b) antiskyrmions with different initial η in the absence of the DDI. Trajectories induced by (c, d) a small driving current ($j = 10 \times 10^{10}$ A m^{-2}) and by (e, f) a large driving current ($j = 100 \times 10^{10}$ A m^{-2}) in the presence of the DDI. In the presence of the DDI, the skyrmion motion is along a straight line with the helicity fixed for the small driving current, but it is along a circle together with the helicity rotation for the large driving current. This is the helicity locking-unlocking transition. The model is a square element (100×100 spins) with the OBC. Here, $K = 0.1$ and $H_z = 0.1$. Adapted with permission from the author's original work [6].

force exerted on the skyrmion is proportional to the skyrmion velocity (cf. Ch. 3), while the magnitude of the skyrmion-edge repulsive force increases and approaches a certain value with decreasing spacing between the skyrmion and the nanotrack edge. Hence, when the Magnus force cannot be compensated by the skyrmion-edge repulsive force, it will result in the annihilation of the skyrmion at the nanotrack edge.

In Fig. 4.8, we show the detailed annihilation process of the skyrmion at the nanotrack edge driven by the spin-polarized current in the FM monolayer nanotrack with the CPP geometry. Here, the driving current density is $j = 5 \times 10^{10}$ A m^{-2}. The given size of the nanotrack is 1000 nm $\times$ 40 nm $\times$ 0.4 nm with $D = 3.0$ mJ m^{-2}. The skyrmion is initially placed at the central line of the FM monolayer nanotrack, where the distance between the skyrmion core and the upper edge equals 20 nm. As shown in Fig. 4.8(a), $t = 8400$ ps, the

skyrmion moves along the nanotrack about a few hundreds of nanometers but the distance between the skyrmion core and the upper edge decreases to only 12 nm due to the SkHE. When $t > 8400$ ps, as shown in Fig. 4.8(b)-(l), the distance between the skyrmion core and the upper edge is reduced to less than 12 nm. The magnetic spins at the upper side of the skyrmion starts to rotate and an instability starts to develop, which breaks the topological protection of the skyrmion and leads to the annihilation of the skyrmion at the upper edge of the nanotrack.

The detrimental effect of the SkHE will be more pronounced when the nanotrack width is reduced. As shown in Fig. 4.9, the given size of the nanotrack is 1000 nm $\times$ w nm $\times$ 0.4 nm. l_{d} represents the horizontal distance between the position where the skyrmion is destroyed and the initial position of the skyrmion. When the width of the nanotrack equals 40 nm, the current-driven skyrmion is destroyed due to the SkHE when it moves about 460 m at the current density of 5×10^{10} A m^{-2}. The velocity of the skyrmion before its destruction equals $\sim$ 55 m s^{-1}. When the width of the nanotrack reduces to 30 nm, the skyrmion is destroyed en route due to the SkHE at a smaller driving current density of 3×10^{10} A m^{-2}, when moves $\sim$ 80 nm. When the nanotrack width is further decreased to 24 nm, the skyrmion is destroyed shortly with a displacement of 2 nm when the driving current of 1×10^{10} A m^{-2} is turned on.

From the application point of view, the nanotrack width is inversely proportional to the packing density as well as the information storage density of the skyrmion-based nanotrack devices, such as the skyrmion-based racetrack-type memory [1, 2]. Therefore, in order to realize a reliable and ultra-fast transport process of skyrmions in the information delivery channel of any information processing device, it is necessary to find a method to avoid the SkHE, as pointed out in the above discussion on the nanotrack with the CIP geometry. For the nanotrack with the CPP geometry, it is also practicable to control the skyrmion trajectory and reduce the detrimental SkHE by construct a varying α. However, a more feasible and effective method to totally eliminate the SkHE is to utilize the antiferromagnetically exchange-coupled bilayer and multilayer nanotracks, i.e., the synthetic AFM (SyAF) nanotracks, which will be investigated in detail and discussed in the next section.

4.3 Skyrmion dynamics in multilayer nanotracks

In this section, we study the motion of skyrmions in bilayer and multilayer SyAF nanotracks driven by vertical spin currents. Figure 4.10 shows the schematics of the simulation models including the FM monolayer ($N = 1$), SyAF bilayer ($N = 2$), SyAF trilayer ($N = 3$), and SyAF quadrilayer ($N = 4$) nanotracks. The FM monolayer nanotrack con-

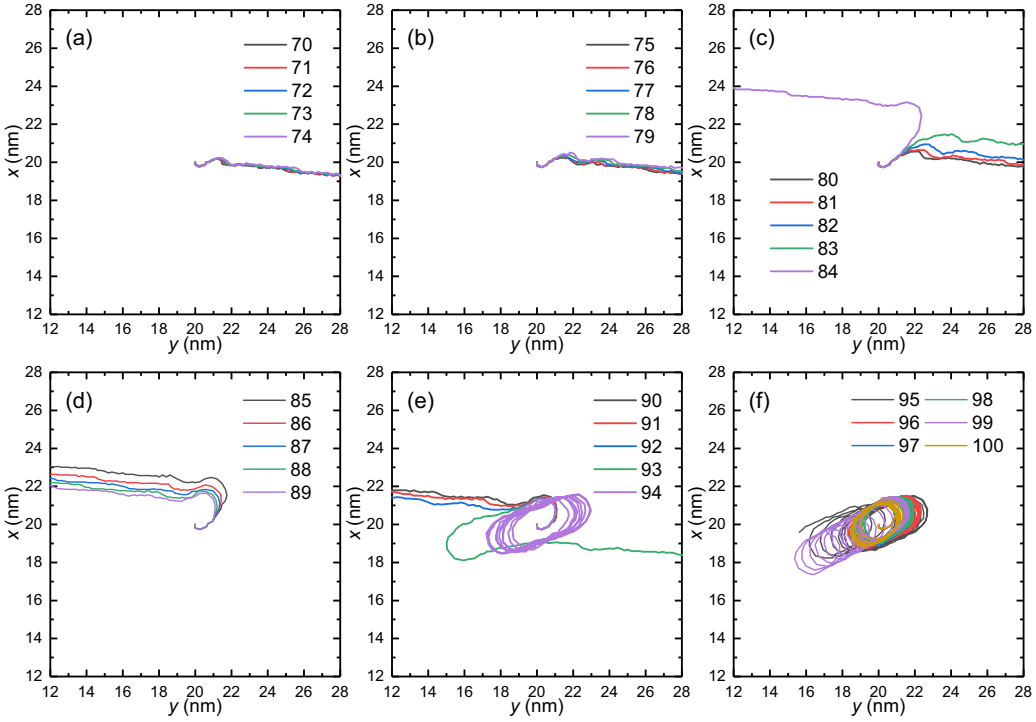

Figure 4.19: The trajectories of the skyrmion at varied values of the driving current density. The skyrmion has an initial helicity number of $\eta = \pi/2$. The driving current density ranges from $j = 70 \times 10^{10}$ A m^{-2} to $j = 100 \times 10^{10}$ A m^{-2}. (a) At small driving current densities (e.g., $j = 70 \times 10^{10}$ A m^{-2}), the skyrmion moves toward the right. (c) When the driving current density is increased to a larger value (e.g., $j = 84 \times 10^{10}$ A m^{-2}), the helicity unlocking event occurs once, and (d) the skyrmion moves toward the left after the flip of the helicity. (f) When the driving current density is further increased to a more larger value (e.g., $j = 94 \times 10^{10}$ A m^{-2}), the helicity is totally unlocked, and the skyrmion moves in an orbital circle. The model is a square element with 100×100 spins. Here, $K = 0.1$ and $H_z = 0.1$. The unit of the current density is 10^{10} A m^{-2}. Adapted with permission from the author's original work [6].

tains one FM layer and a heavy-metal substrate underneath the FM layer. The N-layer SyAF nanotrack ($N \geq 2$) includes N FM layers, which are separated by $N - 1$ nonmagnetic spacer layers. The FM layers are denoted from bottom to top as L1, L2, L3, $\cdots$. In all models, the length along the x-axis, width along the y-axis, and thickness along the z-axis of each FM layer and nonmagnetic spacer are respectively equal to 500 nm, 50 nm, and 1 nm, where the FM layer L1 is attached to the heavy-metal substrate. In the SyAF N-layer nanotracks ($N \geq 2$), the neighboring FM layers are antiferromagnetically exchange-coupled through their ferromagnet/spacer/ferromagnet interfaces. The magnetization in each FM layer is perpendicular to the nanotrack plane due to the high PMA, while the magnetization in neighboring FM layers are antiparallel due to the interlayer AFM ex-

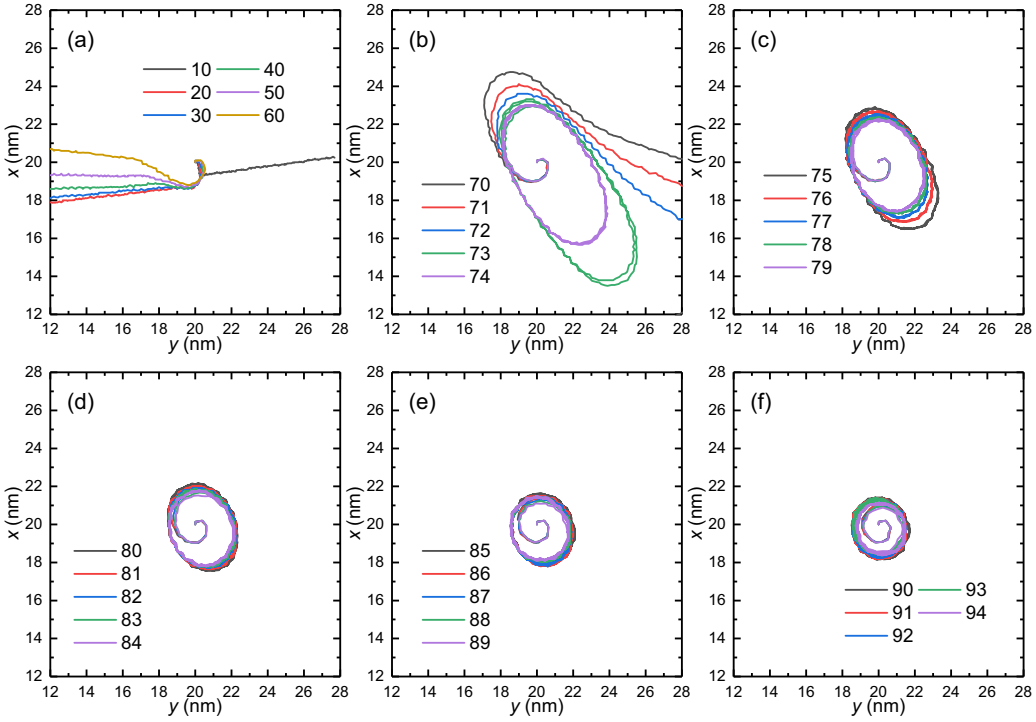

Figure 4.20: The trajectories of the antiskyrmion at varied values of the driving current density. The antiskyrmion has an initial helicity number of $\eta = \pi/2$. The driving current density ranges from $j = 10 \times 10^{10}$ A m^{-2} to $j = 94 \times 10^{10}$ A m^{-2}. (a) At small driving current densities (e.g., $j = 10 \times 10^{10}$ A m^{-2}), the antiskyrmion moves toward the right. (b) When the driving current density is increased to a larger value (e.g., $j = 20 \times 10^{10}$ A m^{-2}), the helicity unlocking event occurs once, and the antiskyrmion moves toward the left after the flip of the helicity. (c)-(f) When the driving current density is further increased to a more larger value (e.g., $j = 73 \times 10^{10}$ A m^{-2}), the helicity is totally unlocked, and the antiskyrmion moves in an orbital circle. The model is a square element with 100×100 spins. Here, $K = 0.1$ and $H_z = 0.1$. The unit of the current density is 10^{10} A m^{-2}. Adapted with permission from the author's original work [6].

change coupling. The DMI in FM layers lead to the tilt of magnetization near the edges of the FM layers. It is worth mentioning that the DMI in FM layers can be induced by both the heavy-metal substrate and spacer layers in real experiments [31]. Recently, theoretical [32, 33] and experimental [34, 35, 36, 37, 38] studies have suggested and developed the methods to induce the DMI in multilayers. More promisingly, it has been experimentally demonstrated that by constructing the spacer layer made of two different heavy-metal materials, additive DMIs can be achieved in multilayers [35].

In our numerical simulations we explicitly consider the SyAF N-layer skyrmions with $N = 1, 2, 3, 4$. We assume that the relaxed magnetization distributions of the FM layers L1 and L3 are almost pointing along the $+z$-direction, while those of the FM layers L2 and

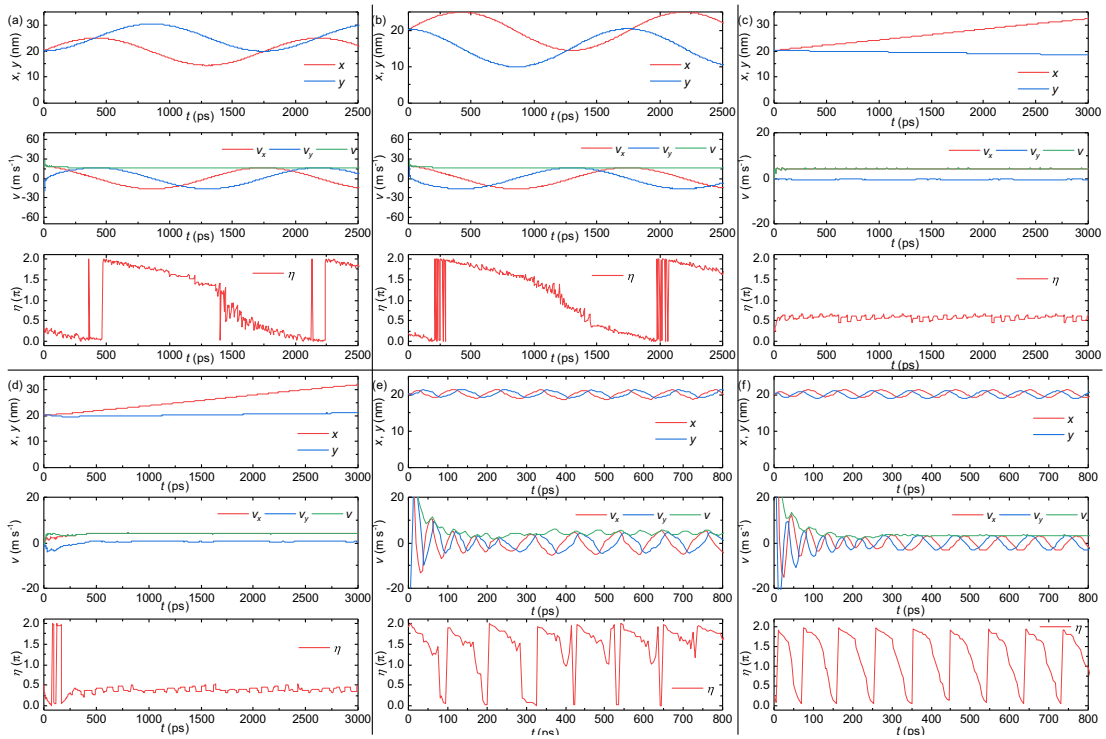

Figure 4.21: The time dependences of the location (x, y), the velocity (v_x, v_y, $v = \sqrt{v_x^2 + v_y^2}$), and the helicity (η) corresponding to Fig. 4.18. (a) and (b) are corresponding to Fig. 4.18(a) and 4.18(b), respectively, where $j = 50 \times 10^{10}$ A m^{-2}. (c) and (d) are corresponding to Fig. 4.18(c) and 4.18(d), respectively, where $j = 10 \times 10^{10}$ A m^{-2}. (e) and (f) are corresponding to Fig. 4.18(e) and 4.18(f), respectively, where $j = 100 \times 10^{10}$ A m^{-2}. The helicity in (a) and (b) is unlocked due to the absence of DDI. The helicity in (c) and (d) is locked due to the presence of DDI. The helicity in (e) and (f) is unlocked due to the presence of both DDI and a strong driving current. The helicity number is calculated by $\eta = \arctan(m_y/m_x)$ on the extreme right spin at the $m_z = 0$ circle of a skyrmion or an antiskyrmion. Adapted with permission from the author's original work [6].

L4 are almost pointing along the $-z$-direction. The background magnetization directions determine the skyrmion number of the skyrmion in each FM layer. The skyrmion number equals 1 in the FM layers L1 and L3, while it equals -1 in the FM layers L2 and L4. The total skyrmion number Q_{tot} of the SyAF N-layer skyrmion is N modulo 2. Namely, $Q_{\text{tot}} = 1, 0, 1, 0$ for $N = 1, 2, 3, 4$, respectively. More generally, the total skyrmion number Q_{tot} is defined as

$$Q_{\text{tot}} = \sum_{n=1}^{N} Q_n, \tag{4.20}$$

where Q_n is the skyrmion number of the skyrmion in the FM layer with layer index n, given as

$$Q_n = -\frac{1}{4\pi} \int \boldsymbol{m}^n(\boldsymbol{x}) \cdot (\partial_x \boldsymbol{m}^n(\boldsymbol{x}) \times \partial_y \boldsymbol{m}^n(\boldsymbol{x}))\, d^2\boldsymbol{x}. \tag{4.21}$$

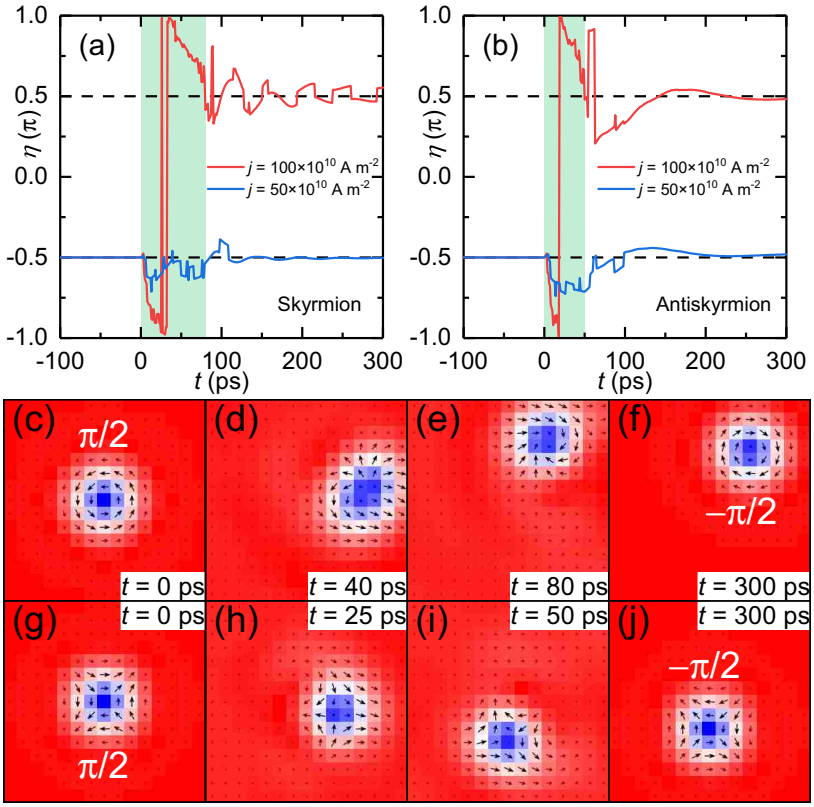

Figure 4.22: Flip of the skyrmion (antiskyrmion) helicity induced by a current pulse. (a) Skyrmion helicity as a function of time. A skyrmion is at rest with the helicity being $\eta = -\pi/2$. The helicity is flipped by a strong 80-ps-long current pulse and becomes $\eta = \pi/2$. Such a flip does not occur by applying a small current pulse with the same duration. (b) A similar flip occurs also for an antiskyrmion. (c)-(f) Snapshots of the skyrmion during the helicity flip process. (g)-(j) Snapshots of the antiskyrmion during the helicity flip process. The model is a square element (39×39 spins) with the OBC. Here, $K = 0.1$ and $H_z = 0.1$. Adapted with permission from the author's original work [6].

At the initial state, the skyrmions are first created and relaxed at the position of $x = 100$ nm, $y = 25$ nm. With regard to the injection scheme of the driving current, as shown in Fig. 4.11(a), we consider a confined CPP geometry. Namely, an electron current flows through the heavy-metal substrate in the $+x$-direction, which is converted into a spin current polarized along the $-y$-direction and is perpendicularly injected into the FM layer L1, due to the SHE. The skyrmion in the FM layer L1 is driven by the vertical spin current, while the other skyrmions in the FM layers L2, L3, and L4 move accordingly due to the interlayer AFM exchange coupling between each adjacent FM layers. It should be noted that, for comparison purpose, we also simulate the straightforward case of unconfined CPP geometry with the bilayer SyAF nanotrack, where the spin current is injected into all FM layers, as illustrated in Fig. 4.11. The skyrmions in all FM layers of a SyAF multilayer

nanotrack are bound to one single SyAF multilayer skyrmion by the interlayer AFM exchange coupling. We call it a SyAF N-layer skyrmion, where N stands for the number of constituent FM layers.

The total Hamiltonian H of the multilayer nanotrack is decomposed into the Hamiltonian for each FM layer H_n and the interlayer AFM exchange coupling H_{inter} between neighboring FM layers, that is,

$$H = \sum_{n=1}^{N} H_n + H_{\text{inter}}. \tag{4.22}$$

The Hamiltonian for each FM layer reads

$$\begin{aligned} H_n &= -A_{\text{intra}} \sum_{\langle i,j \rangle} \boldsymbol{m}_i^n \cdot \boldsymbol{m}_j^n + D_{ij} \sum_{\langle i,j \rangle} (\boldsymbol{\nu}_{ij} \times \hat{z}) \cdot (\boldsymbol{m}_i^n \times \boldsymbol{m}_j^n) \\ &\quad + K \sum_i [1 - (m_i^{n,z})^2] + H_{\text{DDI}}, \end{aligned} \tag{4.23}$$

where n is the FM layer index ($n = 1, 2, \cdots, N$), $\boldsymbol{m}_i^n$ represents the local magnetic moment orientation normalized as $|\boldsymbol{m}_i^n| = 1$ at the site i, and $\langle i, j \rangle$ runs over all the NN sites in each FM layer. The first term represents the intralayer FM exchange interaction with the intralayer FM exchange stiffness A_{intra}. The second term represents the DMI with the DMI coupling energy D_{ij}, where $\boldsymbol{\nu}_{ij}$ is the unit vector between sites i and j. The third term represents the PMA with the anisotropy constant K. H_{DDI} represents the DDI. When $N > 1$, there exists an AFM exchange coupling between the NN FM layers

$$H_{\text{inter}} = -\sum_{n=1}^{N-1} A_{\text{inter}} \sum_i \boldsymbol{m}_i^n \cdot \boldsymbol{m}_i^{n+1}. \tag{4.24}$$

The sign of the interlayer exchange stiffness A_{inter} is negative for the interlayer AFM exchange interaction. We take the initial magnetization direction in the FM layer L1 to be pointing upward (cf. Fig. 4.10). The dynamics of magnetic spins in each FM layer is described by the LLG equation including the Slonczewski-like STT which is generated by the SHE in the heavy-metal substrate (cf. Eq. 4.12). For the confined CPP geometry (cf. Fig. 4.11), we have $j = 0$ in the FM layers above the FM layer L1, thus there is no STT effect on the FM layer with the layer index number $n > 1$.

The 3D micromagnetic simulations are also performed by using the 1.2 alpha 5 release of the OOMMF [24]. The typical material parameters used in the micromagnetic simulations are given in Table 4.1. Besides, we employed additional parameters required by the SyAF multilayer nanotracks: interlayer AFM exchange stiffness $A_{\text{inter}} = -1$ pJ m^{-1}, interface AFM exchange coefficient $\sigma = -1$ mJ m^{-2}, and spin Hall angle $\theta_{\text{SH}} = 0.4$.

Let us first recapitulate the motion of a FM monolayer skyrmion in a FM monolayer nanotrack driven by the vertical spin current, which undergoes a transverse motion toward the upper edge of the nanotrack because of the SkHE. We show the trajectory at a moderate driving current of $j = 10$ MA cm^{-2} in Fig. 4.12(a). The moving skyrmion reaches a stable velocity of $v_x \sim 70$ m s^{-1} and has a transverse shift of ~ 5 nm due to the SkHE. It does not touch the edge because of the repulsive force from the edge. Nevertheless, when $j > 10$ MA cm^{-2}, it is destroyed by touching the edge shortly after the driving current is applied. Let us also recapitulate the motion of a SyAF bilayer skyrmion in a SyAF bilayer nanotrack driven by the vertical spin current. It goes straight in the SyAF bilayer nanotrack as a result of the suppression of the SkHE ($Q_{\rm tot} = 0$). The trajectory at a moderate driving current of $j = 20$ MA cm^{-2} is shown in Fig. 4.12(b), where it reaches a stable speed of ~ 70 m s^{-1}. The SyAF bilayer skyrmion strictly moves along the central line ($y = 25$ nm) of the nanotrack. We continue to study the motion of a SyAF trilayer skyrmion with $Q_{\rm tot} = 1$ [see Fig. 4.12(c)], and a SyAF quadrilayer skyrmion with $Q_{\rm tot} = 0$ [see Fig. 4.12(d)] driven by the vertical spin current. The SyAF trilayer skyrmion experiences the SkHE as in the case of the FM monolayer skyrmion. On the other hand, the SyAF quadrilayer skyrmion moves reliably in the SyAF quadrilayer nanotrack even at a strong driving current, demonstrating the suppression of the SkHE as in the case of the SyAF bilayer skyrmion. The SyAF quadrilayer skyrmion moves along the central line ($y = 25$ nm) of the nanotrack.

We compare the SkHEs at $N = 1$ and $N = 3$ quantitatively. We show the skyrmion Hall angle v_y/v_x as a function of time t in Fig. 4.13(a) for $N = 1, 3$. The skyrmion Hall angle is inversely proportional to N. Namely, the SkHE for $N = 3$ is 3 times smaller than that for $N = 1$. In Fig. 4.13(b), we show the velocity v_x as a function of the applied driving current density j for the motion of SyAF N-layer skyrmions, where $N = 1, 2, 3, 4$. The velocity v_x is almost inversely proportional to N as shown in Fig. 4.13(c). This is because the driving current is only applied to the bottom FM layer L1 [cf. Fig. 4.11(a)].

In order to further improve the j-v relation of the SyAF N-layer skyrmions, here taking the SyAF bilayer skyrmion as an example, we also investigate the j-v curve when the driving current is applied in both constituent FM layers of the SyAF bilayer nanotrack, which is plotted in Fig. 4.13(b) as a dashed curve. It can be seen that, when both FM layers are driven by the current [cf. Fig. 4.11(b)], the j-v relation of the SyAF bilayer skyrmion matches well with that of a FM monolayer skyrmion moving in a FM monolayer nanotrack at the small driving current regime. When $j = 10$ MA cm^{-2}, the velocity of the FM monolayer skyrmion is $v_x = 70$ m s^{-1}, while the velocity of the SyAF bilayer skyrmion is $v_x = 72$ m s^{-1}.

In order to interpret the simulation results, we employ the Thiele equation [39, 40] and

generalize it to the SyAF N-layer skyrmion system in SyAF multilayer nanotracks driven by the vertical spin current. The Thiele equation would read in each FM layer as

$$\boldsymbol{G}_n \times \boldsymbol{v}^n - \mathcal{D}\alpha \boldsymbol{v}^n + \boldsymbol{j}^n_{\text{spin}} + \boldsymbol{I}^n_{\text{AFM}} = \boldsymbol{0}, \tag{4.25}$$

with n the layer index, where $\boldsymbol{v}^n$, $\boldsymbol{j}^n_{\text{spin}}$ and $\boldsymbol{I}^n_{\text{AFM}}$ represent the skyrmion velocity, the spin current, and the interlayer AFM exchange force, respectively. $\boldsymbol{G}_n = (0, 0, 4\pi Q_n)$ is the gyromagnetic coupling constant representing the Magnus force with Q_n the skyrmion number, which is defined by Eq. 4.21. We have taken the same dissipation matrix $\mathcal{D}$ and the same damping coefficient α for all nanotracks.

We assume that all skyrmions move together with the same velocity $\boldsymbol{v}$ since they are tightly bound. Summing all N Thiele Eqs. 4.25, we would phenomenologically obtain

$$\boldsymbol{G}_{\text{tot}} \times \boldsymbol{v} - N\mathcal{D}\alpha \boldsymbol{v} + \boldsymbol{j}_{\text{spin}} = \boldsymbol{0}, \tag{4.26}$$

where the interlayer AFM forces are assumed to be canceled out, i.e., $\sum \boldsymbol{I}^n_{\text{AFM}} = 0$, $\boldsymbol{G}_{\text{tot}} = (0, 0, 4\pi Q_{\text{tot}})$, and $\boldsymbol{j}_{\text{spin}} = \sum_{n=1}^{N} \boldsymbol{j}^n_{\text{spin}}$. Actually, $\boldsymbol{j}^n_{\text{spin}} = \delta_{n1}\boldsymbol{j}_{\text{spin}}$, where $\boldsymbol{j}_{\text{spin}}$ is the spin current induced by the charge current in the heavy-metal substrate due to the SHE.

The first term on the left hand side of Eq. 4.26 corresponds to the Magnus force. When the number N of the FM layers is odd, the total skyrmion number equals one, i.e., $Q_{\text{tot}} = 1$. While when the number N of the FM layers is even, $Q_{\text{tot}} = 0$, because $Q_n = -(-1)^n$. The velocity is given by explicitly solving Eq. 4.26 as

$$v_x = \frac{\alpha N \mathcal{D}}{Q^2_{\text{tot}} + \alpha^2 N^2 \mathcal{D}^2} j_{\text{spin}}, \quad v_y = \frac{Q_{\text{tot}}}{Q^2_{\text{tot}} + \alpha^2 N^2 \mathcal{D}^2} j_{\text{spin}}. \tag{4.27}$$

When $Q_{\text{tot}} = 1$, which is the case for N being odd, a skyrmion undergoes a transverse motion, where

$$\frac{v_y}{v_x} = \frac{1}{\alpha N \mathcal{D}}. \tag{4.28}$$

When $Q_{\text{tot}} = 0$, which is the case for N being even, a skyrmion goes straight, where

$$v_x = \frac{1}{\alpha N \mathcal{D}} j_{\text{spin}}, \quad v_y = 0. \tag{4.29}$$

Consequently the SyAF N-layer skyrmion experiences the SkHE only when N is odd. We call it the odd-even effect of the SkHE on SyAF multilayer nanotracks. As shown in Fig. 4.13, the theoretical expectation Eq. 4.28 explains the numerical data remarkably well with the choice of $\alpha\mathcal{D} = 0.57$. Also, we have fitted the data successfully by theoretical expectation Eq. 4.27 with the use of $\alpha\mathcal{D} = 0.57$.

We have studied the current-driven motion of skyrmions in SyAF multilayer nanotracks in contrast to the motion of skyrmions in conventional FM monolayer nanotracks. We have

found that a moving SyAF bilayer skyrmion is much more stable than a moving FM monolayer skyrmion, because that the two skyrmions consisting the SyAF bilayer skyrmion are tightly bound by the interlayer AFM exchange coupling, and thus the SyAF bilayer skyrmion is immune from the SkHE. Besides, the odd-even effect of the constituent FM layer number on the SkHE in SyAF multilayer nanotracks has also been demonstrated. Due to the suppression of the SkHE, the skyrmions have no transverse motion in SyAF multilayer nanotracks with even constituent FM layers. We suggest that the SyAF bilayer nanotrack is a preferred host for skyrmion transmission in racetrack-type device applications since it realizes a minimum system which does not show the SkHE.

4.4 Skyrmion dynamics in a frustrated magnetic monolayer

In the above sections, we have studied the current-driven motion of the skyrmion in conventional FM monolayer and SyAF multilayer nanotracks. Very recently, it was discovered experimentally that the skyrmion lattice can be stabilized by an order-from-disorder mechanism in the triangular spin model with competing interactions [41]. A rich phase diagram of an anisotropic frustrated magnet and properties of frustrated skyrmions with arbitrary vorticity and helicity were investigated [5]. Other remarkable physical properties of skyrmions in the frustrated magnetic system have also been studied theoretically [4, 42, 43, 44, 45, 46]. A prominent property is that a skyrmion and an antiskyrmion have the same energy irrespective to the helicity in the frustrated magnets. The frustrated skyrmion shows coupled dynamics of the helicity and the center of mass [4, 6]. For example, it is found that the translational motion of a skyrmion is coupled with its helicity in the frustrated magnet, resulting in the rotational skyrmion motion [4, 6]. These novel properties due to the helicity-orbit coupling are lacking in the conventional FM system, where the skyrmion is stabilized by the DMI and the helicity is locked.

In this section, we explore skyrmions and antiskyrmions in a 2D frustrated FM system with competing exchange interactions based on the J_1-J_2-J_3 classical Heisenberg model on a simple square lattice [4, 6]. We explicitly include the DDI, which is neglected in the previous literature [4]. We find that the DDI plays an essential role in the frustrated skyrmion dynamics driven by the spin current.

The Hamiltonian of the J_1-J_2-J_3 classical Heisenberg model on a simple square lat-

Table 4.2: The default intrinsic magnetic parameters for the micromagnetic simulation of the skyrmion dynamics in the frustrated magnetic film. The NN exchange constant, NNN exchange constant, NNNN exchange constant, PMA constant, applied magnetic field, saturation magnetization, Gilbert gyromagnetic ratio, damping coefficient, and spin Hall angle are denoted by J_1, J_2, J_3, K, H_z, M_S, γ_0, α, and θ_SH, respectively. Here $J_1 = 3$ meV.

J_2/J_1	J_3/J_1	K/J_1	H_z/J_1	M_S (A m^{-1})	γ_0 (m A^{-1} s^{-1})	α	θ_SH
-0.8	-1.2	$0 \sim 0.5$	$0 \sim 0.5$	8.0×10^5	2.211×10^5	0.1	0.4

tice [4, 6] is expressed as

$$\begin{aligned}\mathcal{H} = &- J_1 \sum_{<i,j>} \boldsymbol{m}_i \cdot \boldsymbol{m}_j - J_2 \sum_{\ll i,j \gg} \boldsymbol{m}_i \cdot \boldsymbol{m}_j \\ &- J_3 \sum_{\lll i,j \ggg} \boldsymbol{m}_i \cdot \boldsymbol{m}_j - H_z \sum_i m_i^z \\ &- K \sum_i (m_i^z)^2 + H_\mathrm{DDI},\end{aligned} \tag{4.30}$$

where $\boldsymbol{m}_i$ represents the normalized spin at the site i, $|\boldsymbol{m}_i| = 1$. $\langle i,j \rangle$, $\langle\langle i,j \rangle\rangle$, and $\langle\langle\langle i,j \rangle\rangle\rangle$ run over all the NN, next-NN (NNN), and next-NNN (NNNN) sites in the magnetic layer, respectively. J_1, J_2, and J_3 are the coefficients for the NN, NNN, and NNNN exchange interactions, respectively. H_z is the magnetic (Zeeman) field applied along the $+z$-direction, K is the perpendicular magnetic anisotropy (PMA) constant, H_DDI represents the DDI, i.e., the demagnetization. The total energy of the given system contains the NN exchange energy, the NNN exchange energy, the NNNN exchange energy, the anisotropy energy, the Zeeman energy, and the demagnetization energy.

The simulation is carried out by using the OOMMF software with the open boundary condition (OBC) [24]. In addition, we have developed the OXS extension modules for the calculation of the NNN and NNNN exchange interactions. We also used the OOMMF conjugate gradient (CG) minimizer for the spin relaxation simulation, which locates local minima in the energy surface through direct minimization techniques [24].

The time-dependent spin dynamics is described by the LLG equation (cf. Eq. 4.12) augmented with the Slonczewski-like STT. The geometry of the cubic cells generated by the spatial discretization in the simulation is 4 Å $\times$ 4 Å $\times$ 4 Å, namely, the lattice constant is $a = 4$ Å. The polarization direction of the vertical spin current is defined as $\boldsymbol{p} = -\hat{y}$. The default values for other magnetic parameters used in the simulation are listed in Table 4.2. We define the skyrmion number of a spin texture in the continuum limit as

$$Q = -\frac{1}{4\pi} \int \boldsymbol{m}(\boldsymbol{r}) \cdot (\partial_x \boldsymbol{m}(\boldsymbol{r}) \times \partial_y \boldsymbol{m}(\boldsymbol{r}))\, d^2\boldsymbol{r}. \tag{4.31}$$

As discussed in Ch. 3, the normalized spin field $\boldsymbol{m}(\boldsymbol{r})$ takes a value on the 2-sphere S^2. The skyrmion number Q counts how many times $\boldsymbol{m}(\boldsymbol{r})$ wraps S^2 as the coordinate (x, y) spans the whole planar space. We parametrize the spin texture as

$$\boldsymbol{m}(\boldsymbol{r}) = \boldsymbol{m}(\theta, \phi) = (\sin\theta\cos\phi, \sin\theta\sin\phi, \cos\theta), \tag{4.32}$$

with

$$\phi = Q\varphi + \eta, \tag{4.33}$$

where φ is the azimuthal angle ($0 \leq \varphi < 2\pi$) and η is the helicity defined mod 2π. Namely, the helicity η and $\eta - 2\pi$ are identical. Special values of the helicity play important roles, that is, $\eta = 0, \pi/2, \pi, 3\pi/2$. We frequently use $\eta = -\pi/2$ instead of $\eta = 3\pi/2$. We index a skyrmion as (Q, η) with the use of the skyrmion number Q and the helicity η. A skyrmion with $Q < 0$ could be called an antiskyrmion.

We first study the static energy values of the skyrmion and antiskyrmion in the frustrated magnetic film, which is fundamental to the dynamics driven by the spin current. The skyrmion energy and the antiskyrmion energy are degenerate and independent of the helicity η in the absence of the DDI (cf. Ref. [4]). Needless to say, the DDI exists in all magnetic materials, however, it has been customarily considered negligible for a microscopic spin texture. This is actually not the case. We show the detail of each contribution to the skyrmion energy in Fig. 4.14, where the DDI energy is found to be comparable to the anisotropy or Zeeman energy. Indeed, the contribution of the DDI energy is related to the material and geometric parameters of the given sample. We show in Fig. 4.15 that the DDI energy decreases with increasing M_S and increasing thickness of the sample. The DDI energy is independent of the length-to-width ratio, but the DDI energy to total skyrmion energy ratio slightly decreases with increasing thickness. Thus, it is expected that the DDI effect will be more significant in thick samples with large M_S. Also, the NN, NNN, and NNNN exchange interaction energies are independent of the length-to-width ratio, but significantly varies with the thickness.

As indicated in Fig. 4.16, there are two effects from the DDI. First, the degeneracy is resolved between the skyrmion and antiskyrmion. Second, the degeneracy is resolved between various helicities in general. The Bloch-type (Néel-type) skyrmions with $\eta = \pm\pi/2$ ($\eta = 0, \pi$) are found to possess the minimum energy for $Q = \pm 1$ ($Q = \pm 3$). It is consistent with the fact that the DDI is due to the magnetic charge $\rho_{\text{mag}} = \nabla \cdot \boldsymbol{m}$ and prefers the Bloch-type structure [2]. On the other hand, the energy is independent of the helicity for $Q = \pm 2$. The helicity dependence of the energy of antiskyrmions is similar but weaker than that of skyrmions, as shown in Fig. 4.16(b). This is because an antiskyrmion has the anti-vortex-like structure, where the contribution of the DDI is smaller than the

vortex structure of a skyrmion. The helicity dependence of the energy is a new feature due to the DDI.

As a result, all skyrmions ($Q = \pm 1$) with any η relax to the Bloch-type skyrmions with $\eta = \pm\pi/2$ since they have the minimum energy. Exceptions are those possessing the precise initial values of $\eta = 0, \pi$. Indeed, we have studied the relaxation of a skyrmion with $(\pm 1, \eta)$ for different initial values of η in the range of $\eta = 0 \sim 2\pi$. As shown in Fig. 4.17, the skyrmions with the initial helicity of $\eta = 0, \pi/2, \pi, 3\pi/2$ keep their helicity during the relaxation. However, for the skyrmions with other initial helicities, the helicity is relaxed to $\eta = \pm\pi/2$, justifying that the most stable skyrmions have $\eta = \pm\pi/2$. Consequently, the stable skyrmion is the Bloch-type skyrmion carrying the internal degree of freedom indexed by a binary value ($\eta = \pm\pi/2$).

Figure 4.18 show the dynamics of the skyrmion and antiskyrmion driven by the vertical spin current. A skyrmion and an antiskyrmion move rotationally together with a helicity rotation in the frustrated system without the DDI [4], as shown in Figs. 4.18(a) and 4.18(b). The skyrmion and antiskyrmion motion drastically change once the DDI is introduced. Indeed, the DDI produces the energy difference depending on the helicity as shown in Fig. 4.16. Namely, the helicity rotation costs some energies in the order of 0.01×10^{-20} J. Figure 4.17 shows the time evolution of the helicity. The helicity rotates toward that of the Bloch-type state ($\pm\pi/2$) unless the initial helicity is precisely of the Néel-type state. This helicity locking occurs for the small driving current, since the Bloch-type state has the lowest energy in the presence of the DDI. Namely, under the small current injection, the helicity relaxes to that of the Bloch-type state, and then the skyrmion or antiskyrmion moves along a straight line with the helicity fixed, as shown in Figs. 4.18(c) and 4.18(d). This translational motion occurs due to the helicity locking by the DDI, which is highly contrasted to the case without the DDI. However, as shown in Figs. 4.18(e) and 4.18(f), the translational motion with the fixed helicity evolves to be a rotational motion together with a helicity rotation once the driving current density exceeds a certain critical value j_c (cf. Fig. 4.19, Fig. 4.20, and Fig. 4.21). The reason is that the energy injected by the driving current overcomes the potential difference between the Bloch-type and Néel-type skyrmions.

We have revealed prominent properties of the helicity-orbit coupling of the skyrmion motion in the frustrated magnetic film with the DDI. We may design a binary memory together with a switching process based on these properties. Let us start with a skyrmion at rest. (i) It is in one of the two Bloch-type states indexed by the helicity $\eta = \pm\pi/2$; since the helicity is a conserved quantity, we may use it as a one-bit memory. (ii) We can read its value by observing the motion of a skyrmion; when a small current pulse is applied, a

skyrmion begins to move along a straight line toward left or right according to its helicity $+\pi/2$ or $-\pi/2$ [cf. Fig. 4.18(c)]; this is the read-out process of the memory. (iii) On the other hand, when we apply a strong current pulse, a skyrmion begins to rotate together with its helicity rotation; we can tune the pulse period to stop the helicity rotation so that it is relaxed to the flipped value of the initial helicity, as shown in Fig. 4.22. This is the switching process of the memory.

In this section, we have studied skyrmions in a 2D frustrated magnetic system with competing exchange interactions based on the J_1-J_2-J_3 classical Heisenberg model on a simple square lattice. We have demonstrated that the contribution of the DDI energy is significant although the scale of a skyrmion in the frustrated magnetic system is of the order of nanometer. As a result, the Bloch-type skyrmion has the lowest energy. It has a bistable structure indexed by the helicity $\eta = \pm\pi/2$.

The role of the helicity-orbit coupling becomes remarkable in the presence of the DDI. First, a skyrmion moves along a straight line with a fixed helicity under a weak driving current. The moving direction of a skyrmion is opposite when its helicity is opposite. Second, the dynamics of a skyrmion drastically change from the translational motion to the circular motion with the increase of the driving current, which is the locking-unlocking transition of the helicity. Third, we can flip the helicity of a skyrmion by applying a strong current pulse with a reasonable period. We have argued that these properties could be used to design a binary memory together with a read-out process as well as the switching process. These theoretical results have revealed the exotic and promising properties of skyrmions and antiskyrmions in frustrated magnetic systems, which may lead to novel spintronic and topological applications based on the manipulation of skyrmions and antiskyrmions.

BIBLIOGRAPHY

[1] A. Fert, V. Cros, and J. Sampaio, Skyrmions on the track. Nat. Nanotechnol. **8**, 152–156 (2013).

[2] N. Nagaosa, and Y. Tokura, Topological properties and dynamics of magnetic skyrmions. Nat. Nanotechnol. **8**, 899–911 (2013).

[3] A. O. Leonov, and M. Mostovoy, Multiply periodic states and isolated skyrmions in an anisotropic frustrated magnet. Nat. Commun. **6**, 8275 (2015).

[4] S.-Z. Lin, and S. Hayami, Ginzburg-Landau theory for skyrmions in inversion-symmetric magnets with competing interactions. Phys. Rev. B **93**, 064430 (2016).

[5] A. O. Leonov, and M. Mostovoy, Edge states and skyrmion dynamics in nanostripes of frustrated magnets. Nat. Commun. **8**, 14394 (2017).

[6] X. Zhang, J. Xia, Y. Zhou, X. Liu, H. Zhang, and M. Ezawa, Skyrmion dynamics in a frustrated ferromagnetic film and current-induced helicity locking-unlocking transition. Nat. Commun. **8**, 1717 (2017).

[7] F. Jonietz, S. Mühlbauer, C. Pfleiderer, A. Neubauer, W. Münzer, A. Bauer, T. Adams, R. Georgii, P. Böni, R. A. Duine, K. Everschor, M. Garst, and A. Rosch, Spin transfer torques in MnSi at ultralow current densities. Science **330**, 1648–1651 (2010).

[8] T. Schulz, R. Ritz, A. Bauer, M. Halder, M. Wagner, C. Franz, C. Pfleiderer, K. Everschor, M. Garst, and A. Rosch, Emergent electrodynamics of skyrmions in a chiral magnet. Nat. Phys. **8**, 301–304 (2012).

[9] X. Yu, N. Kanazawa, W. Zhang, T. Nagai, T. Hara, K. Kimoto, Y. Matsui, Y. Onose, and Y. Tokura, Skyrmion flow near room temperature in an ultralow current density. Nat. Commun. **3**, 988 (2012).

[10] J. Sampaio, V. Cros, S. Rohart, A. Thiaville, and A. Fert, Nucleation, stability and current-induced motion of isolated magnetic skyrmions in nanostructures. Nat. Nanotechnol. **8**, 839–844 (2013).

[11] J. Iwasaki, M. Mochizuki, and N. Nagaosa, Current-induced skyrmion dynamics in constricted geometries. Nat. Nanotechnol. **8**, 742–747 (2013).

[12] S.-Z. Lin, C. Reichhardt, C. D. Batista, and A. Saxena, Driven skyrmions and dynamical transitions in chiral magnets. Phys. Rev. Lett. **110**, 207202 (2013).

[13] W. Jiang, P. Upadhyaya, W. Zhang, G. Yu, M. B. Jungfleisch, F. Y. Fradin, J. E. Pearson, Y. Tserkovnyak, K. L. Wang, O. Heinonen, S. G. E. Velthuiste, and A. Hoffmann, Blowing magnetic skyrmion bubbles. Science **349**, 283–286 (2015).

[14] G. Yu, P. Upadhyaya, X. Li, W. Li, S. K. Kim, Y. Fan, K. L. Wong, Y. Tserkovnyak, P. K. Amiri, and K. L. Wang, Room-temperature creation and spin-orbit torque manipulation of skyrmions in thin films with engineered asymmetry. Nano Lett. **16**, 1981–1988 (2016).

[15] C. Schütte, and M. Garst, Magnon-skyrmion scattering in chiral magnets. Phys. Rev. B **90**, 094423 (2014).

[16] W. Wang, M. Beg, B. Zhang, W. Kuch, and H. Fangohr, Driving magnetic skyrmions with microwave fields. Phys. Rev. B **92**, 020403 (2015).

[17] X. Zhang, M. Ezawa, D. Xiao, G. P. Zhao, Y. Liu, and Y. Zhou, All-magnetic control of skyrmions in nanowires by a spin wave. Nanotechnology **26**, 225701 (2015).

[18] S. Komineas, and N. Papanicolaou, Skyrmion dynamics in chiral ferromagnets. Phys. Rev. B **92**, 064412 (2015).

[19] L. Kong, and J. Zang, Dynamics of an insulating skyrmion under a temperature gradient. Phys. Rev. Lett. **111**, 067203 (2013).

[20] X. Zhang, J. Xia, G. P. Zhao, X. Liu, and Y. Zhou, Magnetic skyrmion transport in a nanotrack with spatially varying damping and non-adiabatic torque. IEEE Trans. Magn. **53**, 1-6 (2017).

[21] X. Zhang, J. Xia, Y. Zhou, D. Wang, X. Liu, W. Zhao, and M. Ezawa, Control and manipulation of a magnetic skyrmionium in nanostructures. Phys. Rev. B **94**, 094420 (2016).

[22] X. Zhang, Y. Zhou, and M. Ezawa, Magnetic bilayer-skyrmions without skyrmion Hall effect. Nat. Commun. **7**, 10293 (2016).

[23] X. Zhang, M. Ezawa, and Y. Zhou, Thermally stable magnetic skyrmions in multilayer synthetic antiferromagnetic racetracks. Phys. Rev. B **94**, 064406 (2016).

[24] M. J. Donahue, and D. G. Porter, OOMMF User's Guide, Version 1.0, Interagency Report. NO. NISTIR **6376**, 158 (1999).

[25] H. Y. Yuan, and X. R. Wang, Nano magnetic vortex wall guide. AIP Adv. **5**, 117104 (2015).

[26] J. He, and S. Zhang, Localized steady-state domain wall oscillators. Appl. Phys. Lett. **90**, 142508 (2007).

[27] S. G. Reidy, L. Cheng, and W. E. Bailey, Dopants for independent control of precessional frequency and damping in $Ni_{81}Fe_{19}$ (50 nm) thin films. Appl. Phys. Lett. **82**, 1254–1256 (2003).

[28] R. Urban, G. Woltersdorf, and B. Heinrich, Gilbert damping in single and multilayer ultrathin films: role of interfaces in nonlocal spin dynamics. Phys. Rev. Lett. **87**, 217204 (2001).

[29] J. A. King, A. Ganguly, D. M. Burn, S. Pal, E. A. Sallabank, T. P. A. Hase, A. T. Hindmarch, A. Barman, and D. Atkinson, Local control of magnetic damping in ferromagnetic/non-magnetic bilayers by interfacial intermixing induced by focused ion-beam irradiation. Appl. Phys. Lett. **104**, 242410 (2014).

[30] K. Gilmore, I. Garate, A. H. MacDonald, and M. D. Stiles, First-principles calculation of the nonadiabatic spin transfer torque in Ni and Fe. Phys. Rev. B **84**, 224412 (2011).

[31] R. Wiesendanger, Nanoscale magnetic skyrmions in metallic films and multilayers: a new twist for spintronics. Nat. Rev. Mater. **1**, 16044 (2016).

[32] B. Dupé, G. Bihlmayer, M. Böttcher, S. Blügel, and S. Heinze, Engineering skyrmions in transition-metal multilayers for spintronics. Nat. Commun. **7**, 11779 (2016).

[33] H. Yang, A. Thiaville, S. Rohart, A. Fert, and M. Chshiev, Anatomy of Dzyaloshinsk ii-Moriya interaction at Co/Pt interfaces. Phys. Rev. Lett. **115**, 267210 (2015).

[34] S. Woo, K. Litzius, B. Kruger, M.-Y. Im, L. Caretta, K. Richter, M. Mann, A. Krone, R. M. Reeve, M. Weigand, P. Agrawal, I. Lemesh, M.-A. Mawass, P. Fischer, M. Klaui, and G. S. D. Beach, Observation of room-temperature magnetic skyrmions and their current-driven dynamics in ultrathin metallic ferromagnets. Nat. Mater. **15**, 501–506 (2016).

[35] C. Moreau-Luchaire, C. Moutafis, N. Reyren, J. Sampaio, C. A. F. Vaz, N. Van Horne, K. Bouzehouane, K. Garcia, C. Deranlot, P. Warnicke, P. Wohlhüter, J.-M. George, M. Weigand, J. Raabe, V. Cros, and A. Fert, Additive interfacial chiral interaction in multilayers for stabilization of small individual skyrmions at room temperature. Nat. Nanotechnol. **11**, 444–448 (2016).

[36] O. Boulle, J. Vogel, H. Yang, S. Pizzini, D. Souza Chavesde, A. Locatelli, T. O. Mentes, A. Sala, L. D. Buda-Prejbeanu, O. Klein, M. Belmeguenai, Y. Roussigne, A. Stashkevich, S. M. Cherif, L. Aballe, M. Foerster, M. Chshiev, S. Auffret, I. M. Miron, and G. Gaudin, Room-temperature chiral magnetic skyrmions in ultrathin magnetic nanostructures. Nat. Nanotechnol. **11**, 449–454 (2016).

[37] G. Chen, A. T. N'Diaye, Y. Wu, and A. K. Schmid, Ternary superlattice boosting interface-stabilized magnetic chirality. Appl. Phys. Lett. **106**, 062402 (2015).

[38] M. E. Stebliy, A. G. Kolesnikov, A. V. Davydenko, A. V. Ognev, A. S. Samardak, and L. A. Chebotkevich, Experimental evidence of skyrmion-like configurations in bilayer nanodisks with perpendicular magnetic anisotropy. J. Appl. Phys. **117**, 17B529 (2015).

[39] A. A. Thiele, Steady-state motion of magnetic domains. Phys. Rev. Lett. **30**, 230–233 (1973).

[40] R. Tomasello, E. Martinez, R. Zivieri, L. Torres, M. Carpentieri, and G. Finocchio, A strategy for the design of skyrmion racetrack memories. Sci. Rep. **4**, 6784 (2014).

[41] T. Okubo, S. Chung, and H. Kawamura, Multiple-q states and the skyrmion lattice of the triangular-lattice Heisenberg antiferromagnet under magnetic fields. Phys. Rev. Lett. **108**, 017206 (2012).

[42] S. Hayami, S.-Z. Lin, and C. D. Batista, Bubble and skyrmion crystals in frustrated magnets with easy-axis anisotropy. Phys. Rev. B **93**, 184413 (2016).

[43] S. Hayami, S.-Z. Lin, Y. Kamiya, and C. D. Batista, Vortices, skyrmions, and chirality waves in frustrated Mott insulators with a quenched periodic array of impurities. Phys. Rev. B **94**, 174420 (2016).

[44] S.-Z. Lin, S. Hayami, and C. D. Batista, Magnetic vortex induced by nonmagnetic impurity in frustrated magnets. Phys. Rev. Lett. **116**, 187202 (2016).

[45] C. D. Batista, S.-Z. Lin, S. Hayami, and Y. Kamiya, Frustration and chiral orderings in correlated electron systems. Rep. Prog. Phys. **79**, 084504 (2016).

[46] H. Y. Yuan, O. Gomonay, and M. Kläui, Skyrmions and multisublattice helical states in a frustrated chiral magnet. Phys. Rev. B **96**, 134415 (2017).

CHAPTER 5

Driving magnetic skyrmions with spin waves

In this chapter, we present a numerical study on the dynamics of an isolated magnetic skyrmion driven by spin waves in both wide thin films and narrow nanotracks. We also demonstrate that the position of a skyrmion can be controlled and manipulated in confined nanostructures, which could be used for building spintronic circuits.

5.1 Introduction

As a topological object in magnetic materials, the skyrmion is reasonable stable and possesses a peculiar particle-like nature, which makes it suitable for the application as a moveable information carrier. A number of theoretical and numerical studies have demonstrated that skyrmions could be essential components for future magnetic and spintronic devices for data storage and logic computing [1, 2, 3, 4, 5, 6]. In any skyrmion-based devices, the position of an isolated skyrmion must be able to be manipulated by an external driving force.

As studied in Ch. 4, a spin-polarized electric current has been reported to be an effective driving force for the directional motion of skyrmions in confined nanostructures [7, 8, 9, 10]. However, to shift a skyrmion along the central line of a nanotrack by in-plane spin-polarized current requires severe matching between the damping coefficient α and the non-adiabatic STT coefficient β (cf. Ch. 4), limiting possible hosting material systems for skyrmion applications. This situation is similar for the skyrmion driven by vertically injected spin-polarized current due to the presence of the SkHE (cf. Ch. 3 and Ch. 4). Another possibility of controlling a skyrmion is to use the propagating spin wave [11, 12, 13]. The scattering of a propagating spin wave has been demonstrated to generate a momentum-transfer resulting in a skyrmion or domain wall motion [11, 14, 15, 16, 17]. In the absence

of boundaries, the skyrmion will be driven towards the spin wave source, i.e., the skyrmion velocity posses a component antiparallel to the spin wave current [14, 15, 16, 17]. In confined nanostructures, the boundary acts as a potential barrier and its repulsive force can also result in an effective motion parallel to the spin wave current [18, 19]. From the application point of view, spin wave produces less Joule heat than electric current. Hence, the spin wave is promising for practical skyrmion-based applications.

In this chapter, we study the dynamics of an isolated skyrmion in a FM nanotrack with interface-induced DMI driven by spin waves travelling longitudinal or transverse to the nanotrack. In real skyrmion-based devices, skyrmions will travel in circuits consisting of narrow nanotracks. Therefore, the study of the skyrmion dynamics in such nanostructures is crucial for realization of skyrmion-based devices. Besides, we investigate the skyrmion dynamics driven by spin waves in modified nanostructures such as L-corners, T- and Y-junctions, which are the basic ingredients of circuits based on skyrmions.

5.2 Skyrmion dynamics in a nanotrack

We first study the skyrmion dynamics in a FM nanotrack with interface-induced DMI driven by spin waves. The micromagnetic simulations are carried out by using the OOMMF software [20]. The magnetization dynamics are controlled by the LLG equation written as

$$\frac{d\boldsymbol{M}}{dt} = -\gamma_0 \boldsymbol{M} \times \boldsymbol{H}_{\text{eff}} + \frac{\alpha}{M_{\text{S}}}(\boldsymbol{M} \times \frac{d\boldsymbol{M}}{dt}), \tag{5.1}$$

where $\boldsymbol{M}$ is the magnetization, $\boldsymbol{H}_{\text{eff}} = -\partial\varepsilon/\mu_0\partial\boldsymbol{M}$ is the effective field, t is the time, γ_0 is the absolute Gilbert gyromagnetic ratio, α is the damping coefficient, and $M_{\text{S}} = |\boldsymbol{M}|$ is the saturation magnetization. The average energy density ε of the system contains the Heisenberg exchange, PMA, applied magnetic field (Zeeman), DDI (demagnetization), and DMI energy terms, which is expressed as follows

$$\begin{aligned}\varepsilon =& A\left[\nabla\left(\frac{\boldsymbol{M}}{M_{\text{S}}}\right)\right]^2 - K\frac{(\boldsymbol{n}\cdot\boldsymbol{M})^2}{M_{\text{S}}^2} - \mu_0\boldsymbol{M}\cdot\boldsymbol{H} - \frac{\mu_0}{2}\boldsymbol{M}\cdot\boldsymbol{H}_{\text{d}}(\boldsymbol{M}) \\ &+ \frac{D}{M_{\text{S}}^2}\left(M_z\frac{\partial M_x}{\partial x} + M_z\frac{\partial M_y}{\partial y} - M_x\frac{\partial M_z}{\partial x} - M_y\frac{\partial M_z}{\partial y}\right),\end{aligned} \tag{5.2}$$

where A and K are the Heisenberg exchange and PMA energy constants, respectively. $\boldsymbol{H}$ and $\boldsymbol{H}_{\text{d}}(\boldsymbol{M})$ are the Zeeman and demagnetization field. M_x, M_y and M_z are the cardinal components of the magnetization $\boldsymbol{M}$. The material parameters used in the simulation are adopted from Refs. [5, 8, 21, 22, 23, 24, 25, 26], which are listed in Table 5.1. The simulated models are discretized into tetragonal cells with an optimum cell size of 2 nm

Table 5.1: The default intrinsic magnetic parameters for the micromagnetic simulation of the skyrmion dynamics in the FM nanotrack driven by spin waves. The Heisenberg exchange constant, DMI constant, PMA constant, saturation magnetization, Gilbert gyromagnetic ratio, and damping coefficient are denoted by A, D, K, M_{S}, γ_0, and α, respectively.

A (J m^{-1})	D (J m^{-2})	K (J m^{-3})	M_{S} (A m^{-1})	γ_0 (m A^{-1} s^{-1})	α
15×10^{-12}	3.5×10^{-3}	0.8×10^{6}	580×10^{3}	2.211×10^{5}	$0.01 \sim 0.05$

$\times$ 2 nm $\times$ 1 nm, which offers a good trade-off between the computational accuracy and efficiency. Absorbing boundary conditions (ABCs) are implemented in the simulation in order to avoid the reflection of spin waves on sample edges, unless otherwise specified.

The motion of an isolated skyrmion is investigated that is driven by spin waves propagating longitudinal and transverse to the nanotrack. We discuss the resulting skyrmion trajectories and then turn to a discussion of the relation between the driving force and the skyrmion velocity in the steady state.

As shown in Figs. 5.1 and 5.2, we consider nanotracks with a fixed length $l = 400$ nm in the x-direction and various different widths $w = 400, 200, 100,$ and 50 nm in the y-direction corresponding to panels (a)-(d), respectively. The thickness of the nanotrack in the z-direction is set as 1 nm. The initial magnetization profile of the nanotrack corresponds to a magnetization pointing along the $+z$-direction except at the sample center, where a skyrmion is initially located, and at the sample edges, where the magnetization is tilted due to the presence of the DMI.

Two setups with longitudinal and transverse driving are considered, as shown in Figs. 5.1 and 5.2, respectively. The driving force is generated by a locally applied oscillating magnetic field, i.e., a radio frequency (RF) field. The RF field is applied only within a narrow strip of width 15 nm that is either located on the left-hand side of the nanotrack for longitudinal driving or at the top of the nanotrack for transverse driving. We consider an RF field $\boldsymbol{H} = H_{\mathrm{a}} \sin(2\pi f t)\hat{s}$ with stimulating amplitude $H_{\mathrm{a}} = 1000$ mT and frequency $f = 200$ GHz. It possesses a longitudinal polarization with $\hat{s} = \hat{y}$ for Fig. 5.1 and $\hat{s} = \hat{x}$ for Fig. 5.2.

We first discuss the situation of longitudinal driving. Figure 5.1(a1) shows the case of a square-shaped thin-film nanotrack where $l = w = 400$ nm at time $t = 0$. The panels (a2)-(a4) show snapshots at later times after the driving field has been switched on. The RF field at the left edge produces spin waves traveling towards the right, along the length direction of the sample. Since the skyrmion is far away from the sample edges, we observe a nearly pure skew scattering between the propagating spin wave and the skyrmion, which is in a good agreement with that reported in Ref. [14]. Indeed, the spin-wave-skyrmion scattering

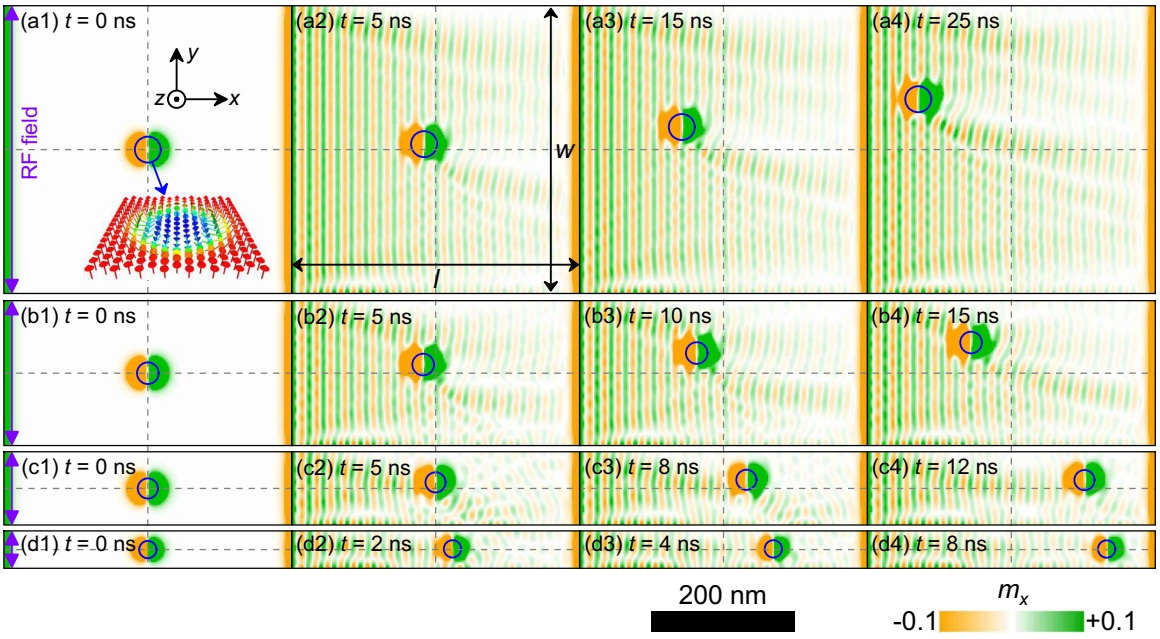

Figure 5.1: Snapshots of a skyrmion driven by spin waves parallel to the nanotrack of length $l = 400$ nm. (a1)-(a4): the width $w = 400$ nm of the nanotrack is equal to the length; (b1)-(b4): $w = 200$ nm; (c1)-(c4): $w = 100$ nm; (d1)-(d4): $w = 50$ nm; time steps of the snapshots are indicated. An RF field with an amplitude of $H_a = 1000$ mT and a frequency of $f = 200$ GHz is applied at the left edge of all samples, producing spin waves traveling towards the right edge. The damping coefficient $\alpha = 0.02$. The inset of (a1) shows the structure of the Néel-type skyrmion in our simulation, which is indicated by blue circles in all snapshots. The color scale shows the in-plane component of the magnetization m_x, which is rescaled to $[-0.1, +0.1]$ in order to show the spin wave profile more clearly. A length scale is also provided. Adapted with permission from the author's original work [27].

leads to a backwards motion of the skyrmion. It can be seen that the skyrmion basically moves against the propagation direction of the spin wave, and reaches the left edge in a finite time. In addition, the skyrmion gets slightly dragged towards the upper edge.

The width in Fig. 5.1(a) is sufficiently large so that the skyrmion reaches the spin wave source before it touches the upper edge of the nanotrack. The situation changes when the nanotrack is narrower. In Fig. 5.1(b) the width is $w = 200$ nm and the skyrmion still has not reached the upper edge at a time $t = 15$ ns. However, for even narrower nanotracks with $w = 100$ nm and $w = 50$ nm, as shown in Figs. 5.1(c) and 5.1(d), it reaches the edge after a short time. Close to the edge, the skyrmion changes the direction of its motion. Instead of approaching the driving layer, the skyrmion moves along the edge away from it. This evading motion along the edge is also much faster than the attractive motion towards the spin wave source.

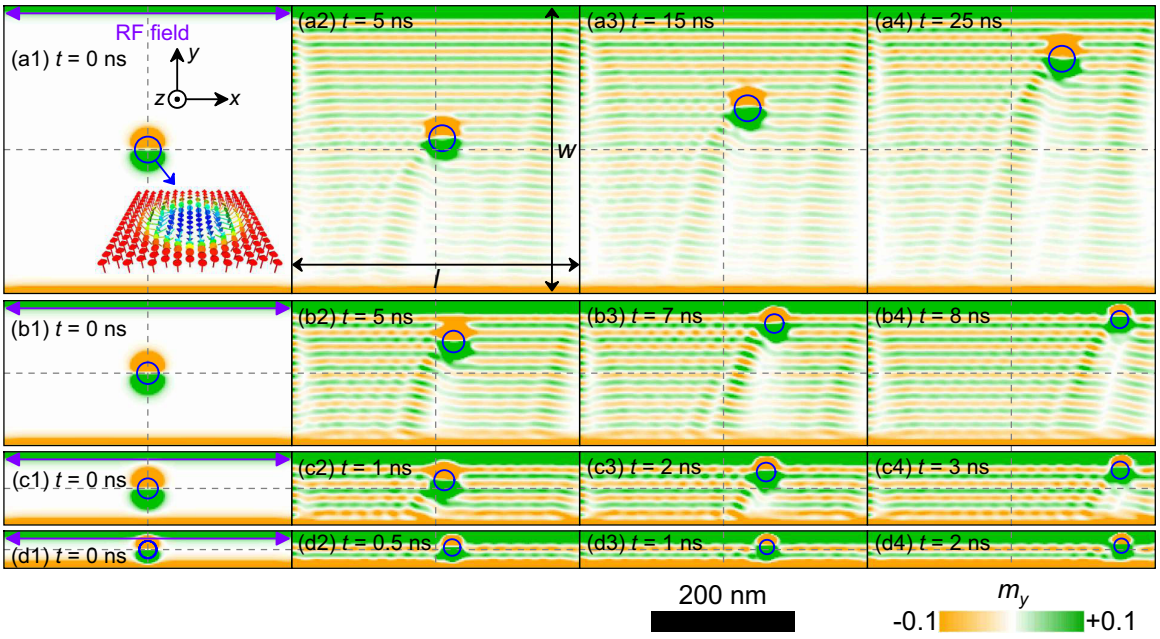

Figure 5.2: Snapshots of a skyrmion driven by spin waves transverse to the nanotrack of length $l = 400$ nm. (a1)-(a4): the width $w = 400$ nm of the nanotrack is equal to the length; (b1)-(b4): $w = 200$ nm; (c1)-(c4): $w = 100$ nm; (d1)-(d4): $w = 50$ nm; time steps of the snapshots are indicated. An RF field with an amplitude of $H_a = 1000$ mT and a frequency of $f = 200$ GHz is applied at the lower edge of all samples, producing spin waves traveling towards the upper edge. The damping coefficient $\alpha = 0.02$. The inset of (a1) shows the structure of the Néel-type skyrmion in our simulation, which is indicated by blue circles in all snapshots. The color scale shows the in-plane component of the magnetization m_y, which is rescaled to $[-0.1, +0.1]$ in order to show the spin wave profile more clearly. A length scale is also provided. Adapted with permission from the author's original work [27].

For the transverse driving, we observe similar effects. The RF field is applied on the upper edge of the nanotrack, as shown in Fig. 5.2, in the same nanotrack geometries as for the parallel driving. Due to the oscillating magnetic field, spin waves are excited and propagate downwards along the $-y$-direction. The interaction with spin waves pushes the skyrmion towards the upper edge of the nanotrack with a slight side-shift to the right-hand side. This can be particularly well seen for the wide nanotrack in Fig. 5.2(a). This setup is however too wide to observe the effects from the nanotrack edge within the simulated time span. In contrast to the longitudinal driving mechanism, the skyrmion is now driven faster towards the upper edge, which becomes apparent for the narrower nanotracks shown in Figs. 5.2(b)-(d). When the skyrmion arrives at the edge, it speeds up dramatically and moves along the upper edge towards the right-hand side. It reaches the end of the nanotrack in a much shorter time than for longitudinal driving.

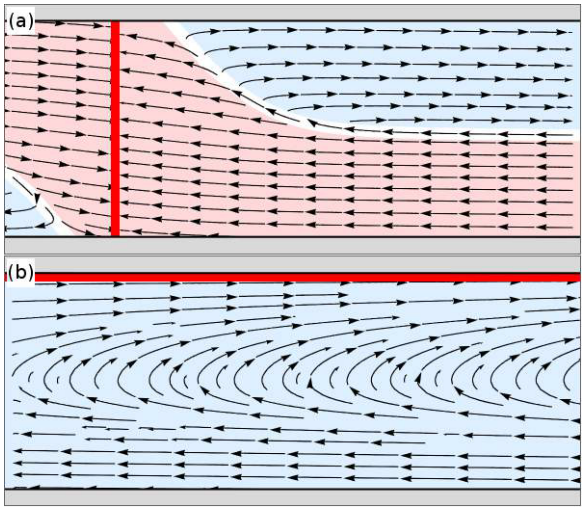

Figure 5.3: Trajectories (black arrows) of a skyrmion derived within the Thiele approximation Eq. 5.3. The skyrmion is driven by spin waves from a source (red line) and flowing longitudinal (a) and transverse (b) to the nanotrack (gray boundaries). Skyrmions in one of the colored areas either run free along the track (blue) or get captured by the spin wave source (red). Areas with different scenarios are divided by a separatrix (white). Calculation parameters are $\mathcal{D}/|G| = 1$, $\alpha = 0.01$, $\sigma_{\parallel}/L_{\text{edge}} = 0.1$, $\sigma_{\perp}/L_{\text{edge}} = 0.1$, $w/L_{\text{sw}} = 5$ for both plots and $L_{\text{sw}}/L_{\text{edge}} = 1$ and $Jq/V_{\text{edge}} = 3$ for the parallel driving (a) and $L_{\text{sw}}/L_{\text{edge}} = 3$ and $Jq/V_{\text{edge}} = 0.01$ for the transverse driving (b). Adapted with permission from the author's original work [27].

The skyrmion trajectories observed by our micromagnetic simulation can be understood in the framework of an effective Thiele motion equation for the skyrmion [28]. Within this description, the skyrmion coordinate $\boldsymbol{R}$ is governed by

$$\boldsymbol{G} \times \dot{\boldsymbol{R}} + \alpha \mathcal{D} \cdot \dot{\boldsymbol{R}} = \boldsymbol{F}(\boldsymbol{R}), \tag{5.3}$$

where $\boldsymbol{G} = G\hat{z}$ is the gyrocoupling vector with $G < 0$, which is related to the skyrmion number Q (cf. Ch. 3), α is the damping coefficient, and $\mathcal{D}$ is the dissipative tensor which can be approximated to be diagonal, $\mathcal{D}_{ij} = \mathcal{D}\delta_{ij}$. The force on the right-hand side is attributed to the edge of the nanotrack and the spin wave driving, $\boldsymbol{F} = \boldsymbol{F}_{\text{edge}} + \boldsymbol{F}_{\text{sw}}$.

Close to the edge, the DMI leads to a twist of the magnetization [29] that acts as a repulsive potential for the skyrmion [23, 30]. To a good approximation, this potential falls off exponentially with the distance to the edge [31]. We thus describe the repulsive force by the edges of a nanotrack of width w by a superposition of edges at positions $y_1 = 0$ and $y_2 = w$, given as

$$\boldsymbol{F}_{\text{edge}}(\boldsymbol{R}) = -V_{\text{edge}} \nabla \left(e^{-\frac{y}{L_{\text{edge}}}} + e^{\frac{y-w}{L_{\text{edge}}}} \right), \tag{5.4}$$

where $V_{\text{edge}} > 0$ parametrizes the strength of the potential and L_{edge} the penetration depth

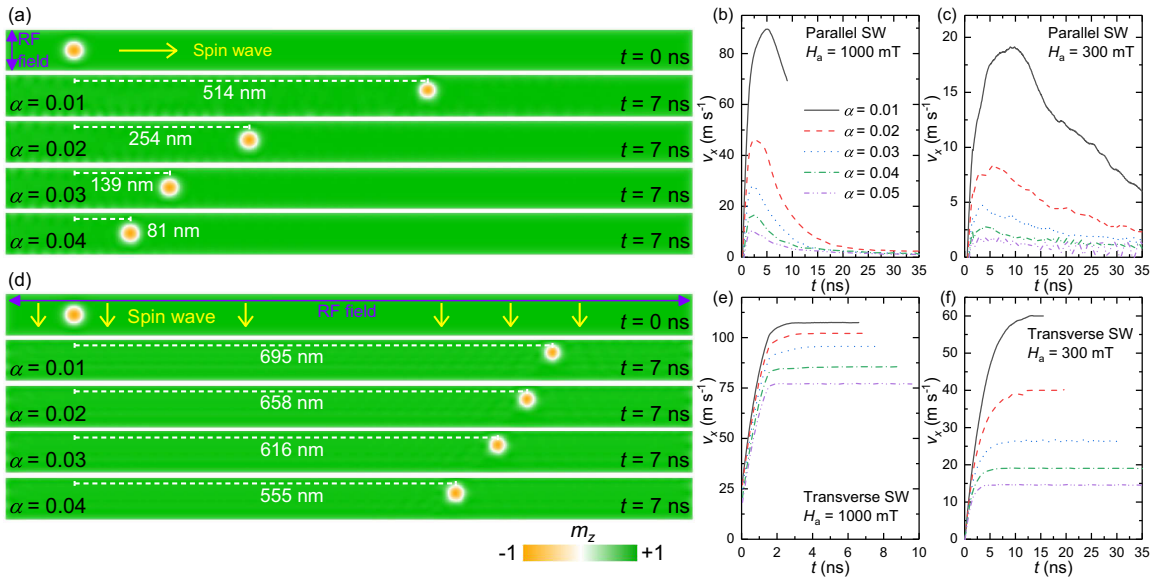

Figure 5.4: Travelled distance and velocity of a single skyrmion in a nanotrack (1000 nm $\times$ 60 nm $\times$ 1 nm) driven by spin waves. Snapshots of the system after 7 ns are shown for longitudinal (a) and transverse (d) driving with different damping coefficients α. Spin waves are excited by an RF field as indicated with $H_\mathrm{a} = 1000$ mT and $f = 180$ GHz. The color scale represents the out-of-plane component of the magnetization m_z. In panel (b), (c) and (e), (f), the velocity parallel to the wire as a function of time, $v_x(t)$, is shown for longitudinal and transverse driving for two different driving amplitudes $H_\mathrm{a} = 1000$ mT and $H_\mathrm{a} = 300$ mT and for various damping coefficients α as given in the inset of (b). The curves are only plotted in the regime, where the skyrmion is sufficiently far from the end of the nanotrack. Adapted with permission from the author's original work [27].

of the magnetization twist.

The momentum-transfer from the spin wave current to the skyrmion also results in a driving force,

$$\boldsymbol{F}_\mathrm{sw}(\boldsymbol{R}) = Je^{-\frac{\boldsymbol{r}\cdot\hat{q}}{L_\mathrm{sw}}} q \left(\sigma_\parallel \hat{q} + \sigma_\perp (\hat{z} \times \hat{q})\right), \tag{5.5}$$

where $J > 0$ is the 2D spin wave current density, and $\vec{q}$ is the wavevector of the spin wave with $q = |\vec{q}|$ and $\hat{q} = \vec{q}/q$. It is pointed out in Ref. [15] that the force is determined by the 2D transport scattering cross section of the skyrmion, $\sigma_\parallel$ and $\sigma_\perp$, longitudinal and transverse to the flow direction $\hat{q}$ of the spin wave current. In general, they depend in a non-trivial manner on the spin wave frequency. In the high-frequency limit or, equivalently, for large spin wave wavevectors q [17], the transverse transport scattering cross section is universal $\sigma_\perp \approx 4\pi/q$ and $\sigma_\parallel \sim 1/q^2$ so that $\sigma_\perp > \sigma_\parallel > 0$. We also accounted for the decay of the spin wave current on a length scale set by the damping coefficient α, $1/L_\mathrm{sw} \approx \alpha\sqrt{\frac{m}{2\hbar}2\pi f}$, where m is the spin wave mass and f is the frequency of the spin wave.

The solution of Eq. 5.3 is plotted in Fig. 5.3 for some set of parameters. For longitudinal

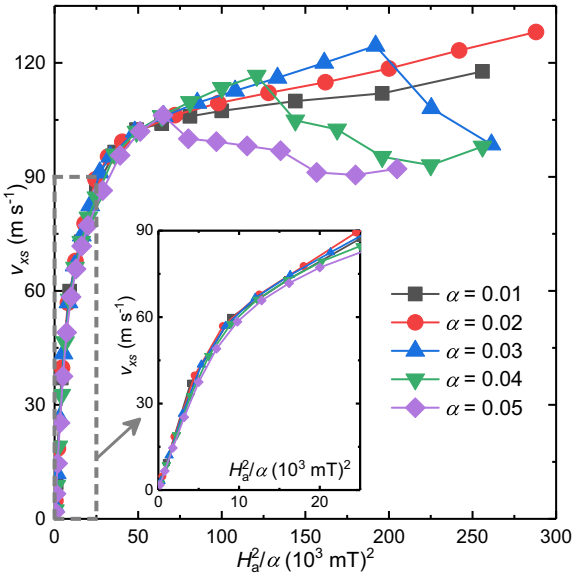

Figure 5.5: The saturation velocity v_{xs} of a skyrmion in a nanotrack as a function of the scaling variable H_a^2/α where H_a is the driving amplitude and α is the damping coefficient. Results from micromagnetic simulations for transverse driving. The stimulating field H_a ranges from 0 to 3200 mT and the frequency is fixed to $f = 180$ GHz. Dimensions of the nanotrack are 1000 nm $\times$ 60 nm $\times$ 1 nm. The saturation velocity v_{xs} is measured when the skyrmion velocity is converged. The inset shows a close-up for low driving where the data approximately collapses onto one single curve. Adapted with permission from the author's original work [27].

driving in Fig. 5.3(a), the nanotrack can be divided into two different areas. The skyrmion trajectories belonging to the red shaded area, on the one hand, will end up at the driving layer (red line). When the skyrmion starts within the blue shaded area, on the other hand, it will be driven away from the driving layer. The interplay between the spin wave and edge forces dominates the motion. As the spin wave current decays exponentially on the length scale L_sw with increasing distance to the driving layer, the spin wave force that keeps the skyrmion close to the edge also decays so that eventually the skyrmion slowly approaches the central line of the nanotrack. The red and blue shaded areas are separated by a critical skyrmion trajectory (white line). In any case, the longitudinal driving setup will not produce a steady state.

In case of transverse driving in Fig. 5.3(b), a skyrmion initially positioned at the center of the nanotrack gets attracted towards the driving layer at the top of the nanotrack. At the same time, it gets repelled by the edge twist of the magnetization and if the driving is not too strong the skyrmion reaches a steady state with $v_{ys} = 0$ and a constant velocity, v_{xs},

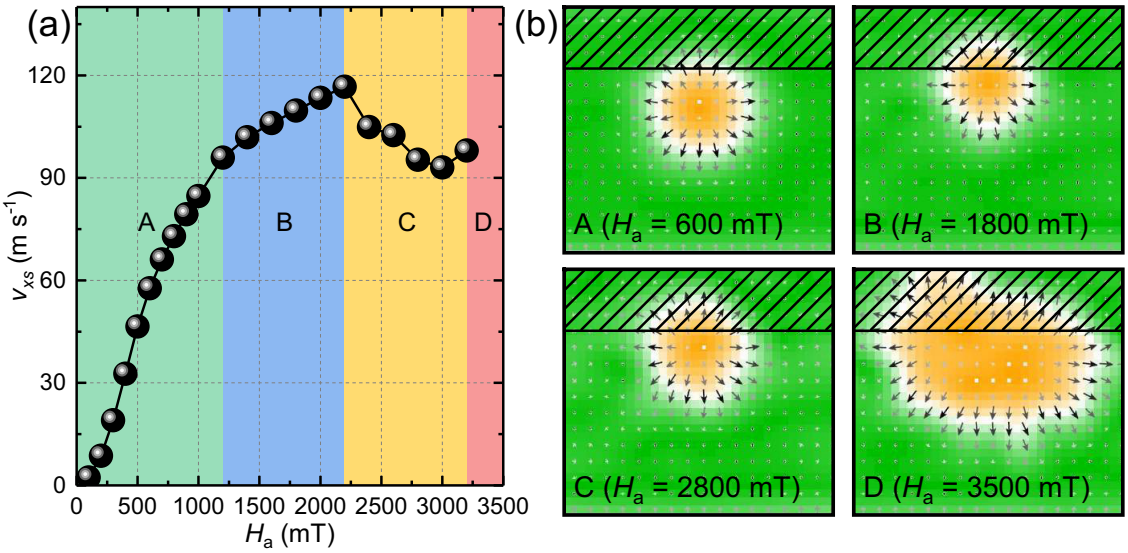

Figure 5.6: (a) The saturation velocity v_{xs} of a skyrmion driven by a transverse spin wave current in a nanotrack as a function of the stimulating field amplitude H_a. Results from micromagnetic simulations. Four different scenarios are marked with a letter and background color. "A", green: the skyrmion moves rigidly along the edge of the nanotrack. "B", blue: the skyrmion moves along the nanotrack and simultaneously emits spin waves. "C", yellow: the skyrmion moves along the nanotrack, emits spin waves, and periodically expands/shrinks in size, i.e., its breathing mode is excited. "D", red: the skyrmion is driven into the edge and gets destroyed when touching it. The frequency of the RF field is $f = 180$ GHz and the damping coefficient is $\alpha = 0.04$. Dimensions of the nanotrack are 1000 nm $\times$ 60 nm $\times$ 1 nm. (b) Snapshots of the magnetization in the four regimes described in (a). The RF field is applied at the upper edge with a width of 15 nm, which is indicated by the shadowed area. The color scale shows the out-of-plane component of the magnetization m_z. Black arrows indicate the in-plane components (m_x, m_y). Adapted with permission from the author's original work [27].

along the edge. Within the Thiele approximation, this saturated velocity is given as

$$v_{xs} = \frac{J}{\alpha D} e^{y/L_\mathrm{sw}} q\sigma_\perp \approx \frac{4\pi J}{\alpha D}. \tag{5.6}$$

It depends on the steady state distance to the edge, y, which is in turn governed by the driving amplitude J. The last equation applies in the high-frequency limit $\sigma_\perp \approx 4\pi/q$ and, in addition, $y/L_\mathrm{sw} \ll 1$. In the limit of a small driving amplitude H_a, the current J will obey $J \propto |H_\mathrm{a}|^2$. In this case, the saturated velocity will scale as $v_{xs} \propto |H_\mathrm{a}|^2/\alpha$.

In order to study the dependence of the skyrmion motion on the damping coefficient α, we performed further simulations with a long and narrow nanotrack with $w = 60$ nm and $l = 1000$ nm for various values of α in the range of $\alpha = 0.01 \sim 0.05$. We consider two amplitudes for the excitation field $H_\mathrm{a} = 300$ mT and $H_\mathrm{a} = 1000$ mT with a frequency

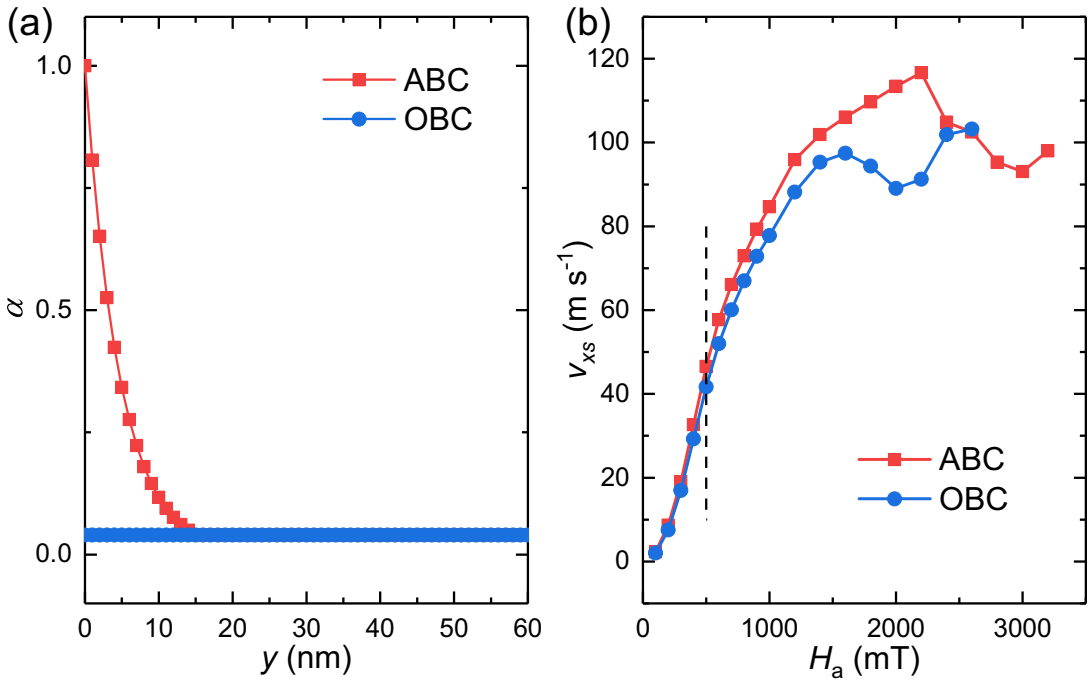

Figure 5.7: (a) The damping coefficient as a function of longitudinal coordinate $\alpha(y)$ for nanotracks with ABC and OBC. (b) The saturation velocity v_{xs} of a skyrmion driven by a transverse spin wave current in a nanotrack as a function of the stimulating field amplitude H_a for nanotracks with ABC and OBC. The results for these two cases start to differ above $H = 500$ mT (vertical dashed line). Adapted with permission from the author's original work [27].

$f = 180$ GHz. The results are shown in Fig. 5.4. All setups share the common property, that the skyrmion moves faster and also further if α is lower. The exact dependence on α is, however, very different for longitudinal and transverse driving.

For longitudinal driving in Fig. 5.4(a), the skyrmion started within the blue shaded area of Fig. 5.3(a) so that its motion is eventually along the edge of the nanotrack. The distance travelled after a time of 7 ns for a driving amplitude $H_\mathrm{a} = 1000$ mT decreases approximately exponentially with increasing α. While for the lowest simulated damping coefficient, $\alpha = 0.01$, the skyrmion travels 514 nm, it travels only half as far (254 nm) if the damping coefficient is doubled to $\alpha = 0.02$. If we increase the damping coefficient further by another $\Delta\alpha = 0.01$, the travelled distance again decreases by a factor 2 to only 139 nm. At even larger damping coefficient, $\alpha = 0.04$, the skyrmion moves 81 nm. The corresponding components of the velocity along the nanotrack, $v_x(t)$, are shown in Fig. 5.4(b). The period of acceleration lasts approximately 5 ns for low damping coefficient, $\alpha = 0.01$, and becomes shorter with increasing damping coefficient. After the peak velocity is reached, the skyrmion decelerates again. This peak velocity can be up to ~ 90 m s^{-1} for

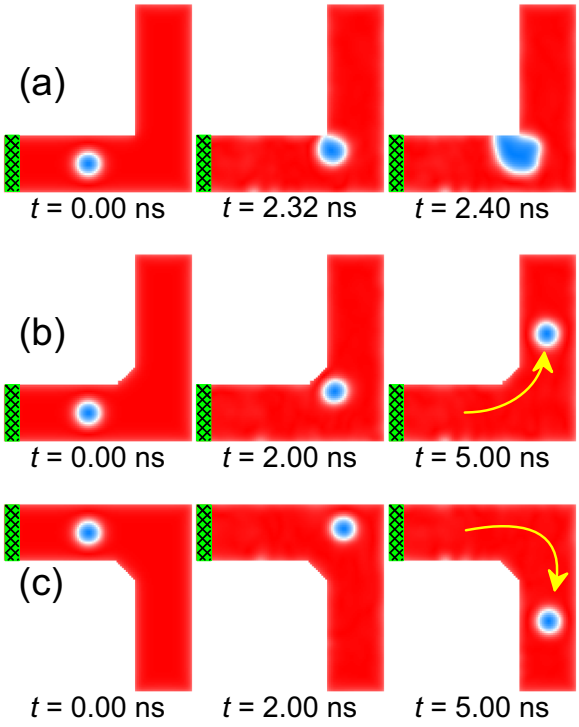

Figure 5.8: Snapshots of the spin-wave-driven skyrmion ($Q = -1$) in the L-corner. The magnetic square field pulse is applied along the lateral axis in the patterned green region with an amplitude of $H_\mathrm{a} = 600$ mT and a frequency of $f = 25$ GHz. The yellow arrow denotes the motion of the skyrmion (hereinafter the same). (a) The skyrmion is destroyed by the corner due to the tilts of magnetization at the corner edge. Hence, we cut the 90-degree corner into two 135-degree corners, and the skyrmion smoothly turns left at the L-corner in (b) and turns right in (c). Adapted with permission from the author's original work [18].

$\alpha = 0.01$, while it is only ~ 45 m s^{-1} for $\alpha = 0.02$ and ~ 25 m s^{-1} for $\alpha = 0.03$. If we lower the RF field amplitude down to $H_\mathrm{a} = 300$ mT, as shown in Fig. 5.4(c), the overall shape of the velocity curves stays the same but the time axis rescales with a factor ~ 2 while the value of the velocity rescales by ~ 0.2. The highest velocity, at $\alpha = 0.01$, is now only ~ 20 m s^{-1} and already < 5 m s^{-1} for $\alpha = 0.03$. For $\alpha > 0.03$ the motion is almost immediately damped out.

For transverse driving in Fig. 5.4(d), the skyrmion moves much faster and further as compared to longitudinal driving. For low damping coefficient $\alpha = 0.01$, the skyrmion travels 695 nm to be compared with 514 nm for longitudinal driving. For large damping coefficient $\alpha = 0.04$ the skyrmion still travels 555 nm. A closer look at the corresponding velocity, as shown in Fig. 5.4(e), reveals that after an acceleration time of ~ 2 ns the skyrmion velocity reaches a steady state. For all simulated damping coefficients, $\alpha \in [0.01, 0.05]$, the saturated velocities along the nanotrack, v_{xs}, are in the regime of 75 up

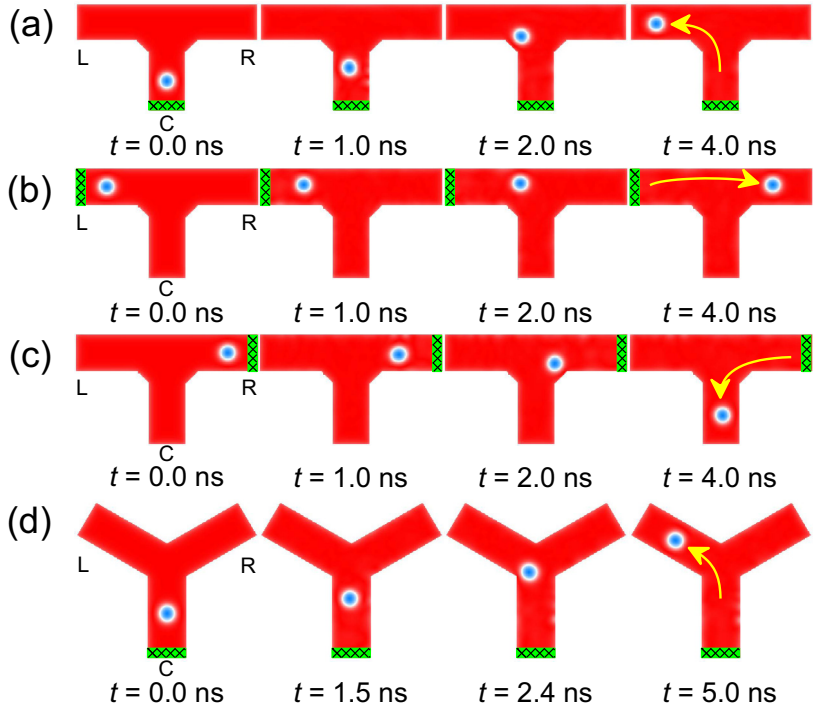

Figure 5.9: Snapshots of the spin-wave-driven skyrmion ($Q = -1$) in the T-junction and Y-junction. (a) The skyrmion turns left from the C-branch into the L-branch of the T-junction. (b) The skyrmion goes straight from the L-branch to the R-branch of the T-junction. (c) The skyrmion turns left from the R-branch into the C-branch of the T-junction. (d) The skyrmion turns left from the C-branch into the L-branch of the Y-junction, similar to (a). Adapted with permission from the author's original work [18].

to 110 m s^{-1} for $H_a = 1000$ mT, which is only comparable to the peak velocity at the lowest damping coefficient for longitudinal driving. The dependence of v_{xs} on the damping coefficient α becomes much more pronounced for smaller driving amplitude $H_a = 300$ mT as shown in Fig. 5.4(f).

For transverse driving, the skyrmion motion can assume a steady state with a constant and saturated velocity. In order to compare with Eq. 5.6 predicted by the Thiele approximation, we obtained the saturated velocity for transverse driving with the help of micromagnetic simulation using damping coefficients $\alpha = 0.01$ up to 0.05 and driving amplitudes within the range of $H_a = 0 \sim 3200$ mT at a fixed frequency of $f = 180$ GHz. The results are shown in Fig. 5.5 as a function of the scaling variable H_a^2/α.

For small values of $H_a^2/\alpha < 10 \times (10^3 \text{ mT})^2$, the data collapses onto a universal straight line corroborating the prediction from Eq. 5.6 using $J \propto |H_a|^2$. For larger values, the data still follows approximately a common curve but the steep increase of v_{xs} flattens out. Close to the value $H_a^2/\alpha \approx 70 \times (10^3 \text{ mT})^2$, the saturated velocity v_{xs} with damping coefficient $\alpha = 0.05$ shows a cusp and abruptly decreases. Subsequently, at higher values of H_a^2/α the

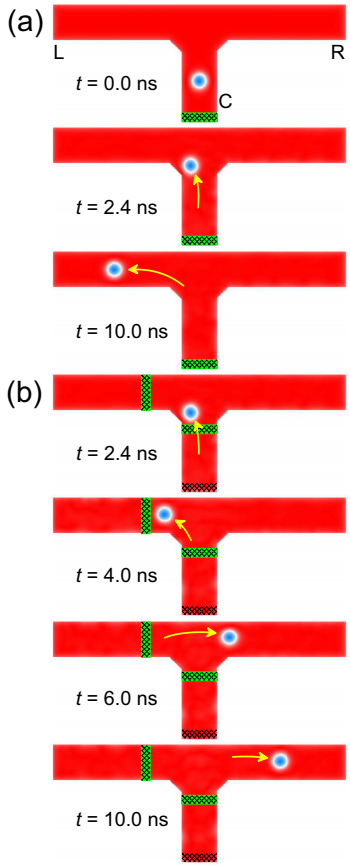

Figure 5.10: Control of the turning direction of the spin-wave-driven skyrmion ($Q = -1$) in the T-junction. (a) The skyrmion naturally turns left from the C-branch into the L-branch of the T-junction. (b) The skyrmion turns right from the C-branch into the R-branch of the T-junction with the help of two magnetic pulse elements. Similar method could be applied to control the turning direction of the skyrmion in the Y-junction. Adapted with permission from the author's original work [18].

velocities for smaller damping coefficients also exhibit a sudden breakdown.

In order to elucidate this sudden decrease of the saturated velocity, we show in Fig. 5.6(a) the saturated velocity v_{xs} versus the driving amplitude H_{a} at a fixed damping coefficient $\alpha = 0.04$. Depending on the strength of H_{a}, we can distinguish four different scenarios "A" to "D". Snapshots of the skyrmion corresponding to these scenarios are shown in Fig. 5.6(b). The shaded area at the top corresponds to the strip where the oscillating driving field is applied. The scenarios are characterized as follows.

Scenario "A" (green region) corresponds to lowest driving fields. In the range from $H_{\mathrm{a}} = 0$ up to 1200 mT, the saturated velocity v_{xs} first increases with H_{a}^2/α as predicted from the Thiele approximation and then turns to a less steep increase. In this regime, the skyrmion smoothly moves along the nanotrack, and does not suffer any significant

deformations. Moreover, only a minor fraction of the skyrmion area has entered the region where the oscillating driving field is applied, as shown in Fig. 5.6(b-A).

Scenario "B" (blue region) is the intermediate regime between $H_\mathrm{a} = 1200$ and 2200 mT. Here, the saturated velocity still increases with the amplitude of the oscillating driving field but the increase is less steep than in scenario "A". This is related to a power loss from the emission of additional spin waves by the skyrmion, which can be discerned in our simulations.

Scenario "C" (yellow region) is obtained in the range from $H_\mathrm{a} = 2200$ up to 3200 mT which is the highest accessible driving amplitude. In this regime the saturated velocity suddenly drops to a lower value. We can associate this sudden drop with the excitation of the internal breathing mode of the skyrmion. As can be seen in Fig. 5.6(b-C), a sizable fraction of the skyrmion is located within the area of the applied oscillating driving field, which facilitates the excitation of internal modes.

Scenario "D" (red region) is the regime where the drive is so strong that the skyrmion will be destroyed shortly after the oscillating driving field is applied. In this limit, $H_\mathrm{a} > 3200$ mT, the skyrmion is driven so hard towards the edge that it is eventually pushed over the edge barrier. The topologically non-trivial skyrmion then unwinds and disappears. A snapshot of the destruction process is shown in Fig. 5.6(b-D).

It is worth mentioning that, for the purpose of avoiding the reflection of spin waves on the sample edges, the ABC is implemented in all simulations discussed above. However, in real-world experiments with nanostructures, the sample edges might indeed reflect spin waves. Hence, for comparison, we also performed simulations with OBC for the representative case of a 1000 nm $\times$ 60 nm $\times$ 1 nm nanotrack, where the skyrmion is driven by a transverse spin wave current. As shown in Fig. 5.7(a), the nanotrack with ABC has an exponentially increasing damping coefficient at the edge, while the nanotrack with OBC has a uniform damping coefficient. Figure 5.7(b) shows the saturation velocity v_{xs} of a skyrmion driven by a transverse spin wave current as a function of the stimulating field amplitude H_a for the models with ABC and OBC. The comparison shows that, when the stimulating field is relatively small ($H_\mathrm{a} < 500$ mT), the results obtained for the model with OBC are in a good agreement with those obtained for the model with ABC. The reason is that the reflection of spin waves is negligible if the exciting field is sufficiently small. Also, the skyrmion barely enters the region of increased damping coefficient at the edge. However, when the stimulating field is relatively large ($H_\mathrm{a} > 500$ mT), the results for v_{xs} obtained for the model with OBC differ quantitatively from those obtained for the model with ABC, and the difference increases with increasing H_a. Nevertheless, it can be seen that qualitatively the four different scenarios can also be identified for the model with OBC, which are now

shifted to lower stimulating field values H_a.

We have studied in depth the motion of an isolated skyrmion in a nanotrack driven by the momentum-transfer force provided by spin waves. We considered two setups where spin waves are excited either longitudinal or transverse to the nanotrack. We find that the longitudinal driving is less efficient partly due to the damping of spin waves. For transverse driving, the skyrmion motion attains a steady-state with constant velocity along the nanotrack. We analyzed the saturated velocity, v_{xs}, as a function of the damping coefficient α and the driving amplitude H_a of the magnetic field that generates spin waves. It obeys for low driving the scaling relation $v_{xs} \propto J/\alpha \propto |H_\mathrm{a}|^2/\alpha$ where the spin wave current amplitude $J \propto |H_\mathrm{a}|^2$. For large transverse driving, the skyrmion is pushed into the driving layer and additional spin wave modes and even the internal breathing mode of the skyrmion become excited. This limits a further increase of the skyrmion velocity and, finally, results in a destruction of the skyrmion. The results in this section demonstrate that the position of a skyrmion can be efficiently manipulated by spin waves, and it elucidates the principle of a spin-wave-driven skyrmion motion, which might be of interest for practical applications.

5.3 Skyrmion dynamics in L-corners, T- and Y-junctions

For the application of skyrmion-based logic circuits, we also study the skyrmion driven by spin waves in modified nanostructures such as L-corners, T- and Y- junctions. In the simulation of the spin-wave-driven skyrmion in the T- and Y-junction, the width of the nanotrack is set as 60 nm, and the thickness of the nanotrack is set as 1 nm. Other simulation parameters are given in Table 5.1. As shown in Fig. 5.8(a), the skyrmion driven by spin waves in a L-corner is destroyed when it turns left and touches the edge at the corner. We therefore cut the 90-degree corner into two 135-degree corners, as shown in Fig. 5.8(b) and 5.8(c). In this configuration, the skyrmion smoothly turns left without touching the edge of the L-corner in Fig. 5.8(b). The spin wave can also drive a skyrmion into the right direction at the L-corner as shown in Fig. 5.8(c).

Figure 5.9 shows the spin-wave-driven motion of a skyrmion in the T-junction and Y-junction. For the case of T-junction, we choose a skyrmion with the skyrmion number of $Q = -1$. The skyrmion always turns left, i.e., from the central branch (C-branch) to the left branch (L-branch) as shown in Fig. 5.9(a), from the L-branch to the right branch (R-branch) as shown in Fig. 5.9(b), and from the R-branch to the C-branch as shown in Fig. 5.9(c). Similarly, for the case of Y-junction, the skyrmion always turns left, as shown in Fig. 5.9(d). By contrast, the skyrmion always turn right if the skyrmion number of the skyrmion is equal to $Q = +1$.

Although the spin-wave-driven skyrmion with negative skyrmion number (cf. Ch. 3) on the T-junction or Y-junction has an intrinsic favor of turning left at the junction as shown in Fig. 5.9, it is also possible to control the turning direction of the skyrmion based on a series of spin-wave-injection pulse elements, magnetic tunnel junction (MTJ) magnetization detectors as well as built-in circuits [1, 23, 32, 33]. Figure 5.10 shows the control of the turning direction of the spin-wave-driven skyrmion in the T-junction. As shown in Fig. 5.10(a), the spin-wave-driven skyrmion with negative skyrmion number will turn left from the C-branch into the L-branch. When the skyrmion is just out of the C-branch ($t = 2.4$ ns) as shown in Fig. 5.10(b), we apply two magnetic field pulse sources (700 mT, 25 GHz) near the exits of the C-branch and the L-branch and simultaneously switch off the pulse source (600 mT, 25 GHz) at the end of the C-branch. In this case, the skyrmion will be pushed into the R-branch by spin waves ($t = 6$ ns).

In conclusion, in this chapter we have presented micromagnetic simulations and analysis that demonstrate the feasibility of spin-wave-driven skyrmions in confined nanostructures with DMI such as nanotracks, L-corners, T- and Y-junctions. We have found a skyrmion can turn a sharp corner without touching edges even in the case of the L-corner. A skyrmion always turns left (right) at the T- or Y-junctions when the skyrmion number is negative (positive). Our results will pave a way to future skyrmion-based applications driven by spin wave in confined nanostructures.

BIBLIOGRAPHY

[1] N. Nagaosa, and Y. Tokura, Topological properties and dynamics of magnetic skyrmions. Nat. Nanotechnol. **8**, 899–911 (2013).

[2] N. Romming, C. Hanneken, M. Menzel, J. E. Bickel, B. Wolter, K. Bergmannvon, A. Kubetzka, and R. Wiesendanger, Writing and deleting single magnetic skyrmions. Science **341**, 636–639 (2013).

[3] A. Fert, V. Cros, and J. Sampaio, Skyrmions on the track. Nat. Nanotechnol. **8**, 152–156 (2013).

[4] W. Koshibae, Y. Kaneko, J. Iwasaki, M. Kawasaki, Y. Tokura, and N. Nagaosa, Memory functions of magnetic skyrmions. Jpn. J. Appl. Phys. **54**, 053001 (2015).

[5] X. Zhang, M. Ezawa, and Y. Zhou, Magnetic skyrmion logic gates: conversion, duplication and merging of skyrmions. Sci. Rep. **5**, 9400 (2015).

[6] X. Xing, P. W. T. Pong, and Y. Zhou, Skyrmion domain wall collision and domain wall-gated skyrmion logic. Phys. Rev. B **94**, 054408 (2016).

[7] X. Zhang, M. Ezawa, and Y. Zhou, Thermally stable magnetic skyrmions in multilayer synthetic antiferromagnetic racetracks. Phys. Rev. B **94**, 064406 (2016).

[8] X. Zhang, Y. Zhou, and M. Ezawa, Magnetic bilayer-skyrmions without skyrmion Hall effect. Nat. Commun. **7**, 10293 (2016).

[9] X. Zhang, J. Xia, G. P. Zhao, X. Liu, and Y. Zhou, Magnetic skyrmion transport in a nanotrack with spatially varying damping and non-adiabatic torque. IEEE Trans. Magn. **53**, 1-6 (2017).

[10] X. Zhang, J. Xia, Y. Zhou, X. Liu, H. Zhang, and M. Ezawa, Skyrmion dynamics in a frustrated ferromagnetic film and current-induced helicity locking-unlocking transition. Nat. Commun. **8**, 1717 (2017).

[11] X. S. Wang, P. Yan, Y. H. Shen, G. E. W. Bauer, and X. R. Wang, Domain wall propagation through spin wave emission. Phys. Rev. Lett. **109**, 167209 (2012).

[12] M. Mochizuki, Spin-wave modes and their intense excitation effects in skyrmion crystals. Phys. Rev. Lett. **108**, 017601 (2012).

[13] S.-Z. Lin, C. Reichhardt, C. D. Batista, and A. Saxena, Driven skyrmions and dynamical transitions in chiral magnets. Phys. Rev. Lett. **110**, 207202 (2013).

[14] J. Iwasaki, A. J. Beekman, and N. Nagaosa, Theory of magnon-skyrmion scattering in chiral magnets. Phys. Rev. B **89**, 064412 (2014).

[15] C. Schütte, and M. Garst, Magnon-skyrmion scattering in chiral magnets. Phys. Rev. B **90**, 094423 (2014).

[16] C. Schütte, J. Iwasaki, A. Rosch, and N. Nagaosa, Inertia, diffusion, and dynamics of a driven skyrmion. Phys. Rev. B **90**, 174434 (2014).

[17] S. Schroeter, and M. Garst, Scattering of high-energy magnons off a magnetic skyrmion. Low Temp. Phys. **41**, 817–825 (2015).

[18] X. Zhang, M. Ezawa, D. Xiao, G. P. Zhao, Y. Liu, and Y. Zhou, All-magnetic control of skyrmions in nanowires by a spin wave. Nanotechnology **26**, 225701 (2015).

[19] J. Kim, and S.-K. Kim, Origin of robust interaction of spin waves with a single skyrmion in perpendicularly magnetized nanostripes. arXiv preprint arXiv:1508.05682 (2015).

[20] M. J. Donahue, and D. G. Porter, OOMMF User's Guide, Version 1.0, Interagency Report. NO. NISTIR **6376**, 158 (1999).

[21] J. Sampaio, V. Cros, S. Rohart, A. Thiaville, and A. Fert, Nucleation, stability and current-induced motion of isolated magnetic skyrmions in nanostructures. Nat. Nanotechnol. **8**, 839–844 (2013).

[22] Y. Zhou, and M. Ezawa, A reversible conversion between a skyrmion and a domain-wall pair in a junction geometry. Nat. Commun. **5**, 4652 (2014).

[23] X. Zhang, G. P. Zhao, H. Fangohr, J. P. Liu, W. X. Xia, J. Xia, and F. J. Morvan, Skyrmion-skyrmion and skyrmion-edge repulsions in skyrmion-based racetrack memory. Sci. Rep. **5**, 7643 (2015).

[24] X. Zhang, Y. Zhou, M. Ezawa, G. P. Zhao, and W. Zhao, Magnetic skyrmion transistor: skyrmion motion in a voltage-gated nanotrack. Sci. Rep. **5**, 11369 (2015).

[25] Y. Zhou, E. Iacocca, A. A. Awad, R. K. Dumas, F. C. Zhang, H. B. Braun, and J. Akerman, Dynamically stabilized magnetic skyrmions. Nat. Commun. **6**, 8193 (2015).

[26] S. Zhang, J. Wang, Q. Zheng, Q. Zhu, X. Liu, S. Chen, C. Jin, Q. Liu, C. Jia, and D. Xue, Current-induced magnetic skyrmions oscillator. New J. Phys. **17**, 023061 (2015).

[27] X. Zhang, J. Müller, J. Xia, M. Garst, X. Liu, and Y. Zhou, Motion of skyrmions in nanowires driven by magnonic momentum-transfer forces. New J. Phys. **19**, 065001 (2017).

[28] A. A. Thiele, Steady-state motion of magnetic domains. Phys. Rev. Lett. **30**, 230–233 (1973).

[29] S. Rohart, and A. Thiaville, Skyrmion confinement in ultrathin film nanostructures in the presence of Dzyaloshinskii-Moriya interaction. Phys. Rev. B **88**, 184422 (2013).

[30] J. Iwasaki, M. Mochizuki, and N. Nagaosa, Current-induced skyrmion dynamics in constricted geometries. Nat. Nanotechnol. **8**, 742–747 (2013).

[31] C. Navau, N. Del-Valle, and A. Sanchez, Analytical trajectories of skyrmions in confined geometries: Skyrmionic racetracks and nano-oscillators. Phys. Rev. B **94**, 184104 (2016).

[32] R. Tomasello, E. Martinez, R. Zivieri, L. Torres, M. Carpentieri, and G. Finocchio, A strategy for the design of skyrmion racetrack memories. Sci. Rep. **4**, 6784 (2014).

[33] Y. Zhang, W. S. Zhao, D. Ravelosona, J.-O. Klein, J. V. Kim, and C. Chappert, Perpendicular-magnetic-anisotropy CoFeB racetrack memory. J. Appl. Phys. **111**, 093925 (2012).

CHAPTER 6

Possible applications of magnetic skyrmions

In this chapter, we numerically demonstrate possible future applications of magnetic skyrmions, including racetrack-type memories, logic computing devices, and voltage-gated transistor-like functional devices.

6.1 Introduction

Skyrmions are first theoretically predicted to exist in magnetic metals [1, 2] and magnetic thin films [3]. In 2009, skyrmions are experimentally observed with the formation of skyrmion lattice in MnSi [4]. Since then, skyrmions have been observed in not only FM materials [5, 6, 7, 8, 9, 10] but also other types of materials, such as semiconductors [11], multiferroic materials [12], ferroelectric nanocomposites [13], and transition metals [14]. In order to build the skyrmion-based devices, the stability and mobility of the skyrmion are current major concerns. The stability of a skyrmion could be improved via enhancing the effective DMI. For example, when the FM layer is sandwiched between two different heavy-metal layers, the DMI induced at the two interfaces could be additive if the DMI with opposite signs are induced at the two interfaces [15, 16]. The strength of DMI can also be enhanced via increasing the thickness of the heavy metal [17]. By enhancing the DMI, both stability and size of the skyrmion can be improved. So far, the room-temperature skyrmions have been obtained with diameter of ~ 30 nm [16]. The motion of a skyrmion driven by the spin-polarized current at room temperature has also been obtained experimentally [18, 19, 20]. These results make progress toward the realization of skyrmion-based applications. As we have introduced, skyrmions have small size, which is helpful to miniaturize the skyrmion-based devices. Another advantage is that the minimal current density required to drive skyrmions into motion is smaller than that is required by conventional

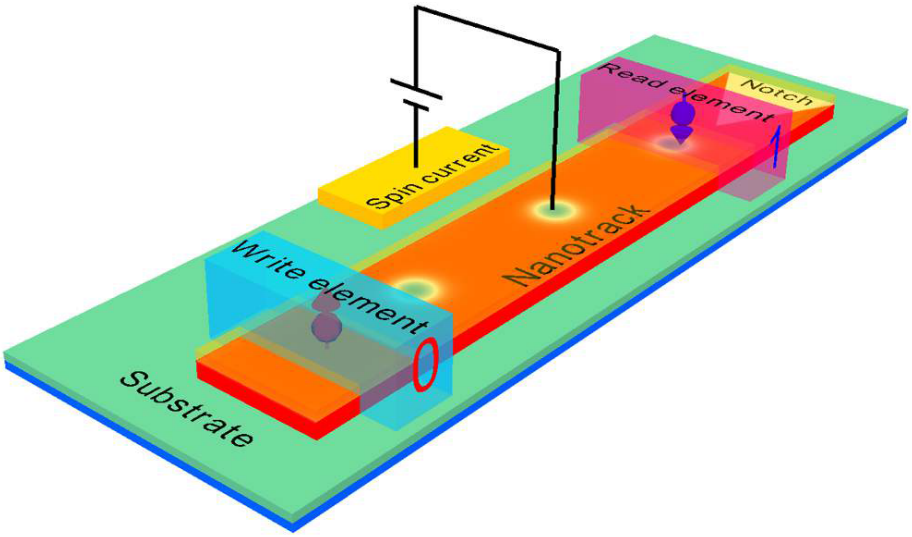

Figure 6.1: Illustration of the skyrmion-based racetrack memory. The information are encoded via skyrmions and shifted via the vertical spin current. The reading element can be placed at one end of the racetrack. Adapted with permission from the author's original work [29].

domain walls [21, 22, 23, 24], which implies that the skyrmion-based devices have low energy consumption. All these efforts make skyrmions more robust to be candidates for spintronic applications. Since the skyrmion has the small size, topologically protected stability, and low energy consumption, many potential applications of skyrmions have been proposed [24, 25, 26, 27, 28]. In this chapter, we show that skyrmions can be used for building racetrack-type memories, logic computing devices and transistor-like devices.

6.2 Skyrmion-based racetrack memory

The racetrack-type memory is proposed by Parkin et al. in 2008 [34], where domain walls are used to code information. Similarly, skyrmions can be used as information carriers in the skyrmion-based racetrack-type memory [35, 36], as shown in Fig. 6.1. In the skyrmion-based racetrack-type memory, in order to transport information, we need to drive the skyrmion information carriers into motion. The injection of the spin-polarized current is the most popular way to drive skyrmions. The in-plane spin-polarized current can be used to drive skyrmions into motion. On the one hand, the vertical injection of the spin current via SHE is more efficient than the in-plane injected current to drive skyrmions in the nanotrack [24, 32, 37]. However, as we have studied in Ch. 4, skyrmions driven by the vertical spin current experiences the SkHE [19, 20, 38] where skyrmions shows a transverse shift. The SkHE may lead to the destruction of skyrmion by pushing it to the edge of

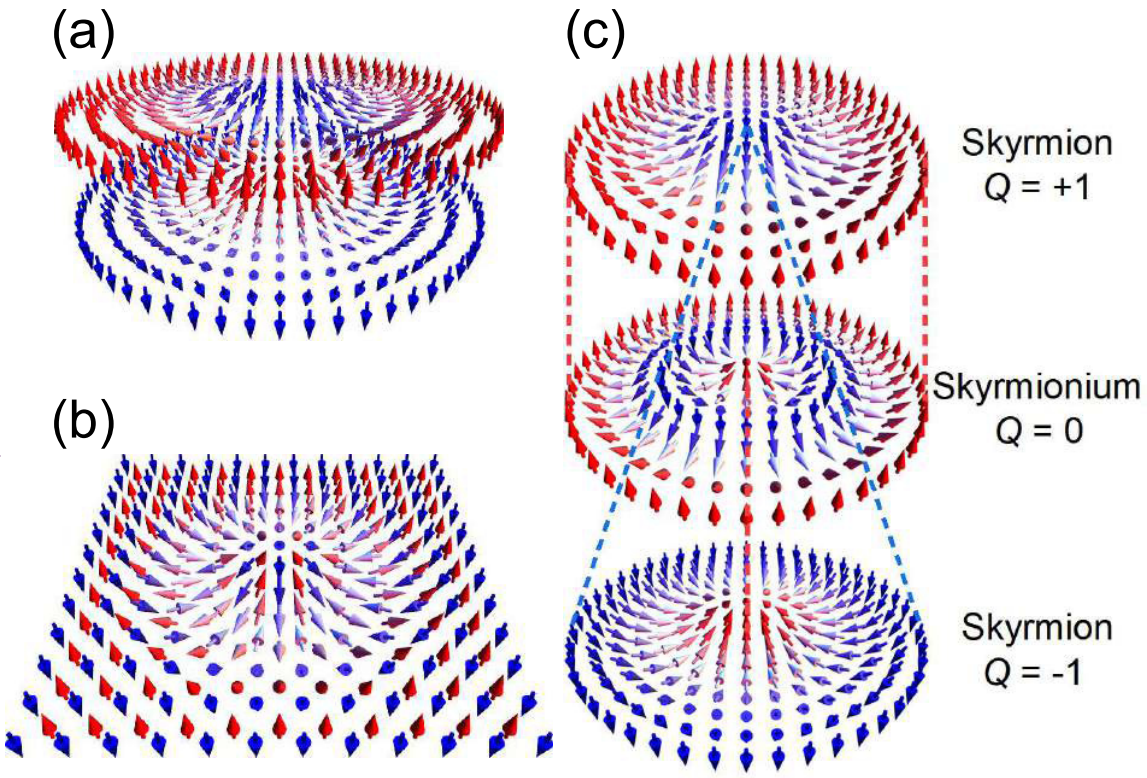

Figure 6.2: Possible skyrmion candidates for the racetrack-type application. (a) AFM-coupled bilayer skyrmion [30], (b) AFM skyrmion [31], and (c) FM skyrmionium [32]. Adapted with permission from the author's original work [30, 31, 32].

nanotrack, resulting in the damage of information. In this section, three possible solutions, AFM-coupled bilayer skyrmion [30], AFM skyrmion [31], and FM skyrmionium [32], are proposed as candidates for building the skyrmion-based racetrack memory, where the skyrmion information carrier can move along the nanotrack without showing the SkHE.

The AFM-coupled bilayer skyrmion is proposed to overcome the SkHE [38, 30, 19, 20]. As shown in Fig. 6.2(a), the AFM bilayer skyrmion is composed by two skyrmions which exist in the antiferromagnetically exchange-coupled bilayer systems (cf. Ch. 4). As discussed in Ch. 3, the SkHE is induced by the topological structure-induced Magnus force. The direction of Magnus force is determined by the topological charge of the skyrmion, i.e., the skyrmion number. Due to the AFM coupling, the skyrmion numbers of two skyrmions in the bilayer skyrmion are opposite. When the spin current is injected, the Magnus forces exerting on the two skyrmions are opposite too. When the AFM exchange coupling between two layers is weak, the AFM-coupled skyrmions may be separated by the Magnus forces and then destroyed by touching the edges [30]. When the AFM exchange coupling is sufficiently strong, the two skyrmions in the AFM bilayer systems are coupled

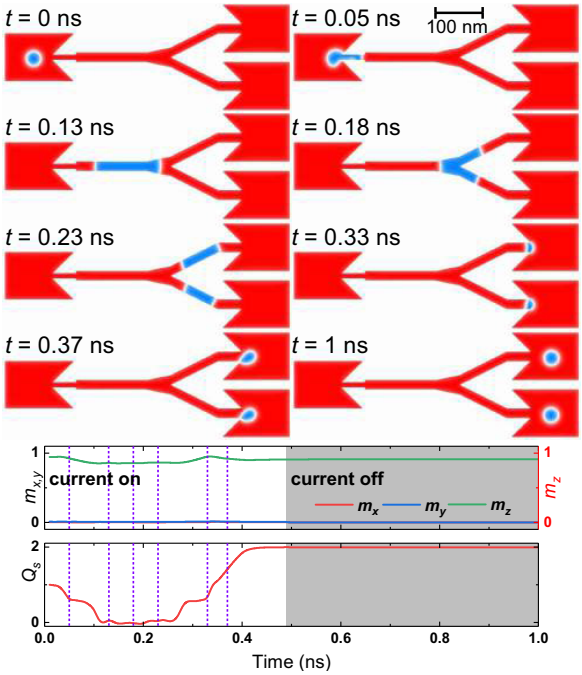

Figure 6.3: Duplication of a skyrmion. The top panel shows the snapshots of the magnetization configuration at eight selected times corresponding to the vertical lines in the middle and bottom panels. The middle panel shows the time evolution of average spin components m_x, m_y, and m_z.The bottom panel shows the time evolution of the skyrmion number Q_{s}. Adapted with permission from the author's original work [33].

together and the Magnus forces exerting on the two skyrmions are canceled. Accordingly, the AFM-coupled bilayer skyrmion can move in a straight line along the nanotrack [30].

Another solution is the skyrmion in AFM materials, i.e., the AFM skyrmion [31, 39], as shown in Fig. 6.2(b). As mentioned in Ch. 2, there are two sublattices in the AFM system, where the NN spins are aligned in an antiparallel manner. The AFM skyrmion can be seen as the composition of two skyrmions having opposite skyrmion numbers. When the spin current is injected, the Magnus forces acting on each sublattice skyrmion are pointing along opposite directions. The magnetization of each sublattice are identical in AFM materials, which leads to the perfect cancellation of the Magnus forces exerting on each sublattice. Hence, the AFM skyrmion can straightly move along the nanotrack driven by spin currents. Compared to the FM skyrmion, the AFM skyrmion can be driven by a larger current density and higher speed can be obtained since the SkHE is eliminated.

As shown in Fig. 6.2(c), the skyrmionium is the other possible candidate for building the skyrmion-based racetrack memory. A skyrmionium has a doughnut-like out-of-plane spin texture in the thin film, and can be phenomenologically viewed as a coalition of two skyrmions with opposite skyrmion numbers. Due to the zero skyrmion number, the

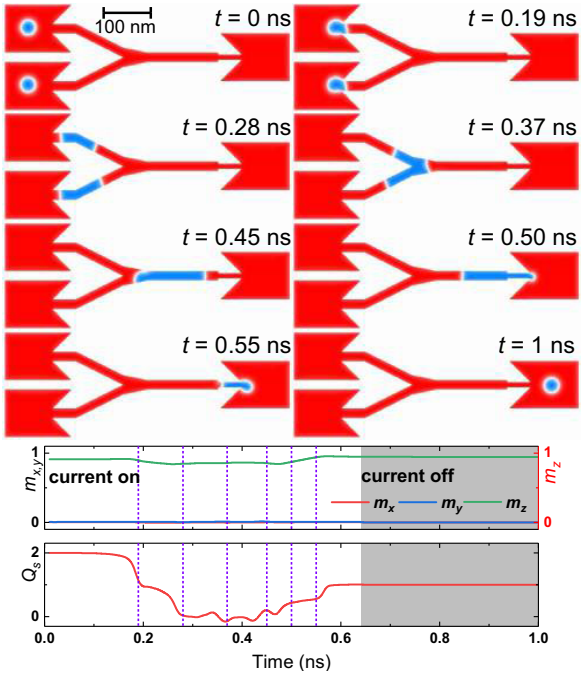

Figure 6.4: Merging of two skyrmions. The top panel shows the snapshots of the magnetization configuration at eight selected times corresponding to the vertical lines in the middle and bottom panels. The middle panel shows the time evolution of average spin components m_x, m_y, and m_z.The bottom panel shows the time evolution of the skyrmion number Q_s. Adapted with permission from the author's original work [33].

skyrmionium is free of the SkHE and could obtain higher speed than the skyrmion when they are driven by the vertically injected spin-polarized current [32]. It should be mentioned that when the skyrmionium moves with a high speed driven by the spin-polarized current, the large driving force could result in the distortion and even destruction of the skyrmionium. To avoid the destruction of the skyrmionium moving with a ultrahigh speed, AFM-coupled bilayer system can be constructed. Similar to the case of AFM-coupled bilayer skyrmion, the AFM-coupled bilayer skyrmionium is hard to be destroyed by the driving current, and thus can move with a higher speed.

For the purpose of improving the design of skyrmion-based racetrack memory, the three solutions we show here are with respect to the information carrier itself. Some solutions with respect to the racetrack structures have also been proposed, for example, one can locally modify the magnetic properties of the racetrack to realize a reliable transport of skyrmion information carriers [40, 41, 42].

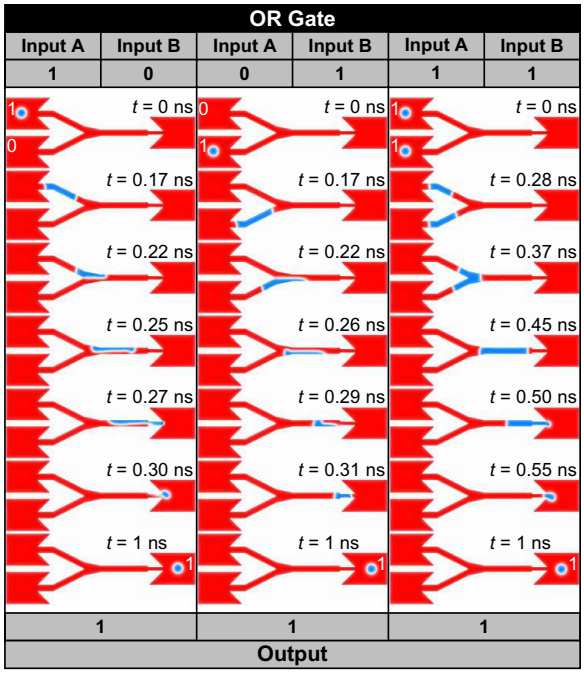

Figure 6.5: Skyrmion logical OR operation. Left panel, the basic operation of the OR gate $1 + 0 = 1$. Middle panel, the basic operation of the OR gate $0 + 1 = 1$. Right panel, the basic operation of the OR gate $1 + 1 = 1$. Adapted with permission from the author's original work [33].

6.3 Skyrmion-based logic gates

The conversion between skyrmions and domain wall pairs have been proposed recently [43]. The duplication and merging of skyrmions can be realized based on the reversible conversion between skyrmions and domain wall pairs. As shown in Fig. 6.3, the skyrmion is duplicated in the designed nanotrack. Initially, a skyrmion is located in the left input nanotrack. Under the injection of spin current, the skyrmion moves toward the right and then is converted into a domain wall pair in the narrow region. A domain wall pair is duplicated into two domain wall pairs via the Y-junction, i.e., the fan-out structure. The two domain wall pairs are converted into two skyrmions at the right output nanotracks. We can see that the total skyrmion number of the system changes from $Q = 1$ to $Q = 2$. With the same designed nanotrack, two skyrmions can be merged into one skyrmion, as shown in Fig. 6.4. Initially, two skyrmions are placed in the left input nanotracks. The two skyrmions are driven toward the right output nanotrack and then converted into two domain wall pairs in the narrow nanotrack. At the Y-junction, two domain wall pairs are merged into one domain wall pair. At the right output nanotrack, the domain wall pair is converted into a skyrmion. The skyrmion merging is thus completed.

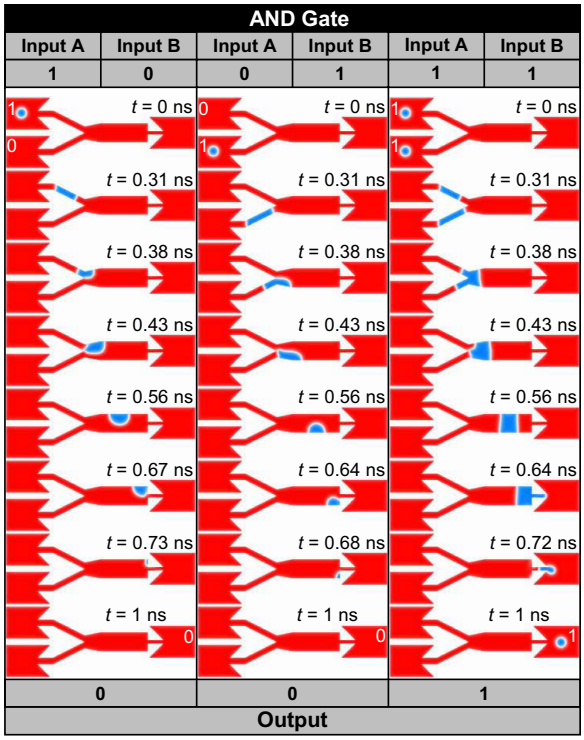

Figure 6.6: Skyrmion logical AND operation. Left panel, the basic operation of the AND gate $1 + 0 = 0$. Middle panel, the basic operation of the AND gate $0 + 1 = 0$. Right panel, the basic operation of the AND gate $1 + 1 = 1$. Adapted with permission from the author's original work [33].

Based on the duplication and merging of skyrmions, the logic OR and AND operations can be implemented, as shown in Figs. 6.5 and 6.6, respectively. Here, the skyrmion represents logical 1, and the FM ground state represents logical 0. In Fig. 6.5, the logical OR operation is demonstrated, i.e., $1 + 0 = 1$, $0 + 1 = 1$, and $1 + 1 = 1$. For operation $1 + 0 = 1$, there is a skyrmion in the input A and no skyrmion in the input B at initial time, which represents input $= 1 + 0$; The output is logical 1, where a stable skyrmion is in the output side. For operation $0 + 1 = 1$, there is a skyrmion in the input B side and no skyrmion in the input A side at initial time, which represents input $= 0 + 1$; The output is logical 1, where a stable skyrmion is in the output side. For operation $1 + 1 = 1$, there is a skyrmion in both the input A side and the input B side, which represents input $= 1+1$; The output is logical 1, where a stable skyrmion is in the output side. The operation $0 + 0 = 0$ means there is no input and there is no output. In Fig. 6.6, the logical AND operation is demonstrated, i.e., $1 + 0 = 0$, $0 + 1 = 0$, and $1 + 1 = 1$. For the operation $1 + 0 = 0$, there is a skyrmion in the input A side and no skyrmion in the input B side at initial time, which represents input $= 1 + 0$. The output is logical 0, where there is no skyrmion is in the output side. For the operation $0 + 1 = 0$, there is a skyrmion in the input B side and

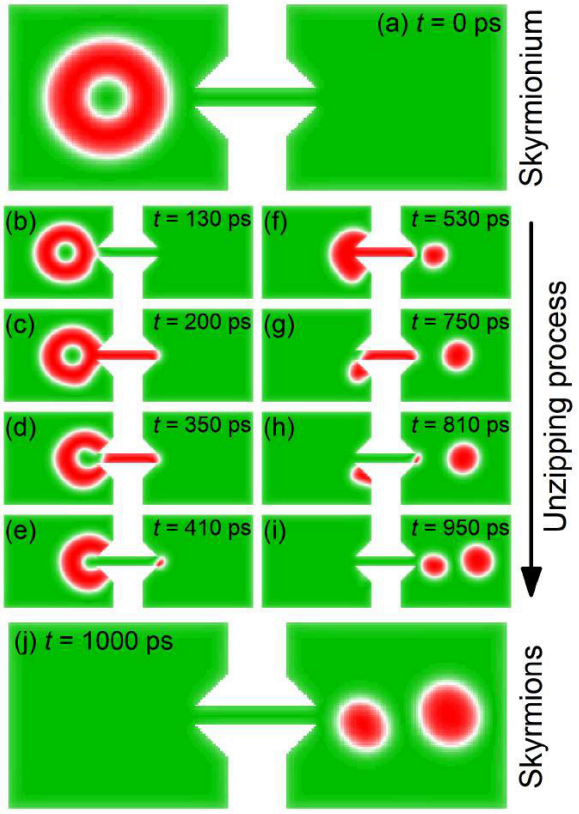

Figure 6.7: Unzipping of a skyrmionium with $Q_s = 0$ into two skyrmions with $Q_s = \pm 1$ in a FM nanotrack with the junction geometry. (a)-(j) Top views of the magnetization configuration of the device at selected times. Adapted with permission from the author's original work [32].

no skyrmion in the input A side at initial time, which represents input $= 0 + 1$. The output is logical 0, where no skyrmion is in the output side. For the operation $1 + 1 = 1$, there is a skyrmion in both the input A side and the input B side, which represents input $= 1 + 1$. The output is logical 1, where a stable skyrmion is in the output side.

With the reversible conversion between skyrmions and domain wall pairs, we can also design a nanotrack to unzip a skyrmionium into two skyrmions, as shown in Fig. 6.7. Initially, a skyrmionium is relaxed at the right input nanotrack, the skyrmionium is converted into four domain walls successively. Two domain walls can be seen as a domain wall pair and can be converted into one skyrmion. We have two domain wall pairs, then we get two skyrmions in the right output nanotrack finally.

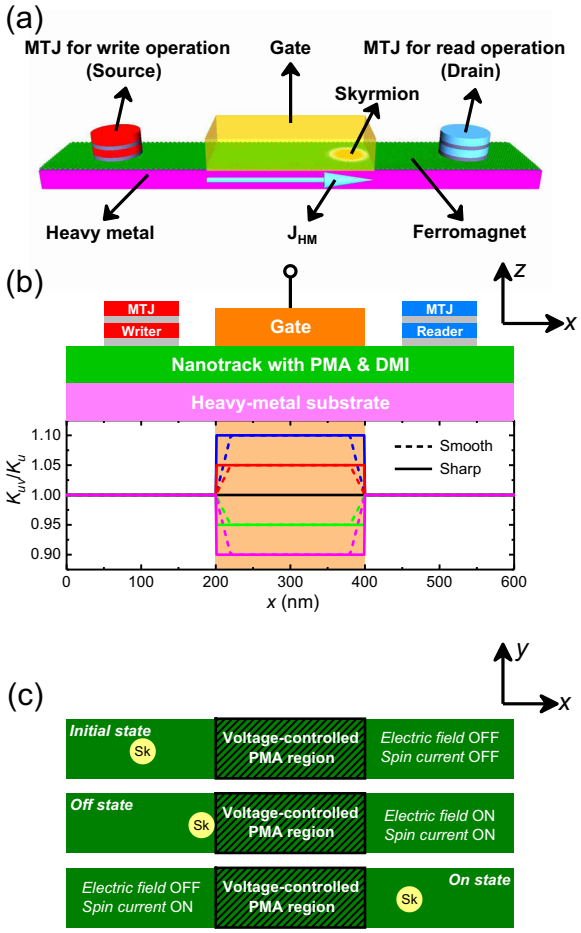

Figure 6.8: (a) Design of a skyrmion-based transistor-like device. (b) Schematic view (xz-plane) of the device. The green rectangle indicates a FM nanotrack and the orange rectangle represents the top electrode for locally changing PMA. The graph shows the PMA profiles of the nanotrack with sharp and smooth transitions. (c) Schematic view (xy-plane) of three states of the skyrmion-based transistor-like device: *inital*, *off* and *on*. Adapted with permission from the author's original work [26].

6.4 Skyrmion-based transistor-like device

The skyrmion-based transistor-like device is designed to control the motion of skyrmions in the nanotrack by using an applied electric field, as shown in Fig. 6.8(a). The switch function of transistor can be realized. In the skyrmion-based transistor-like device, the PMA of the gate region is locally controlled by the applied electric field [44, 45, 46]. The skyrmion is injected at the source side of the nanotrack via MTJ and driven into motion toward the drain side by the spin-polarized current injected from the heavy-metal layer to the FM layer due to SHE (cf. Ch. 4). The voltage gate is placed in the middle of the nanotrack. Due to the application of voltage, the PMA of the gate region varies from the intrinsic PMA of the

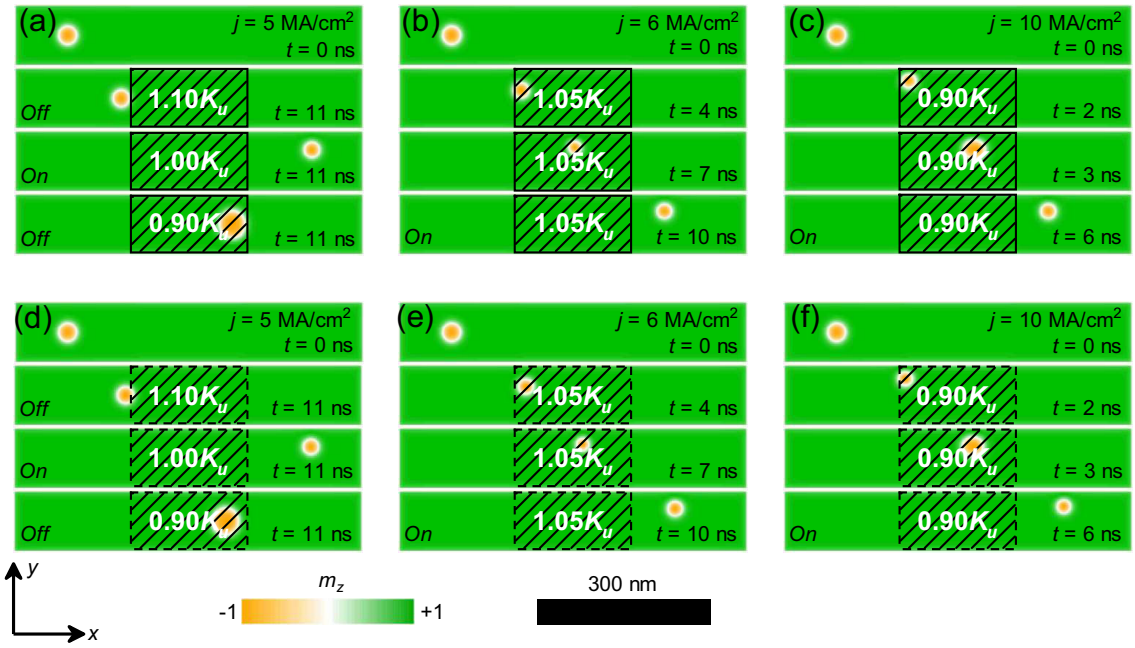

Figure 6.9: Top-view snapshots of the skyrmion-based transistor-like device with different voltage-controlled PMA and current density in the voltage-gated region with (a) sharp and (b) smooth transition profiles at selected times. The color scale denotes the out-of-plane component of the magnetization. The black-line shadow represents the voltage-controlled PMA region. Adapted with permission from the author's original work [26].

nanotrack. The PMA profiles with sharp and smooth transitions are shown in Fig. 6.8(b). The variation of PMA results in the formation of a potential well/barrier. The skyrmion could be stopped by the gate region if the potential well/barrier is too large to be overcome. This is the *off* state of the skyrmion-based transistor-like device, as shown in Fig. 6.8(c). When the voltage gate is turned off, the skyrmion driven by the spin-polarized current passes the voltage-gated region. This is *on* state.

The working states can be tuned with the amplitude of the applied electric field and the spin-polarized current density. In Fig. 6.9(a), the voltage gate is turned on, $K_{\mathrm{uv}} = 1.10K_{\mathrm{u}}$. The skyrmion is driven by the spin current and stopped by the voltage gate since that the barrier is too high to get through. When the voltage gate is turned off, $K_{\mathrm{uv}} = K_{\mathrm{u}}$. The skyrmion driven by the spin-polarized current can pass the voltage gate. When the voltage gate is turned on, $K_{\mathrm{uv}} = 0.90K_{\mathrm{u}}$, resulting a potential well. Under the driving force provided by the spin-polarized current, the skyrmion drops into the potential well. Due to the deep well, the skyrmion stops at the right boundary of the voltage gate region. The working state can be adjusted by the spin-polarized current density. As shown in Fig. 6.9(b), both spin-polarized current and voltage gate are turned on, $K_{\mathrm{uv}} = 1.05K_{\mathrm{u}}$ and $j = 6$ MA/cm^2.

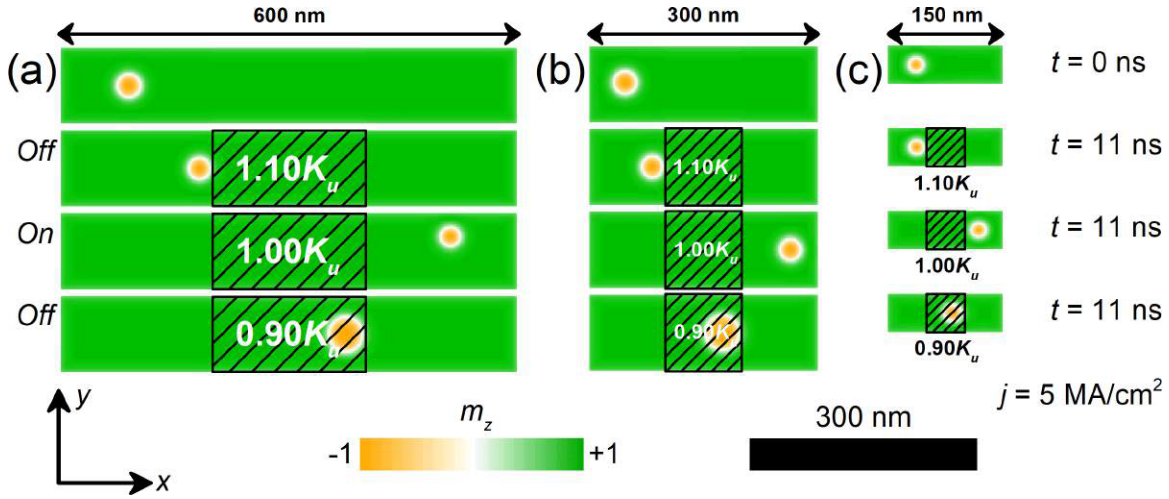

Figure 6.10: Top-view snapshots of the skyrmion-based transistor-like device with different sizes under the same working conditions at selected times. The sizes of the nanotracks are: (a) $600 \times 100 \times 1$ nm^3; (b) $300 \times 100 \times 1$ nm^3; (c) $150 \times 50 \times 1$ nm^3. The color scale denotes the out-of-plane component of the magnetization. The black-line shadow represents the voltage-controlled PMA region. Adapted with permission from the author's original work [26].

Although there is a potential barrier, the skyrmion can overcome the potential barrier and pass the voltage gate due to the large driving force. In Fig. 6.9(c), $K_{\mathrm{uv}} = 0.90K_{\mathrm{u}}$ and $j = 10$ MA/cm^2, the large driving force lead the skyrmion to pass the potential well. The results for the smooth transition profile of PMA are shown in Fig. 6.9(d)-(f). The working states are the same for the cases of sharp and smooth transitions.

We further check the effect of device size on the working states. The results are given in Fig. 6.10. With the same applied voltage and spin-polarized current, the results for the nanotracks of $600 \times 100 \times 1$ nm^3, $300 \times 100 \times 1$ nm^3 and $150 \times 50 \times 1$ nm^3 are the same, indicating that the scalability of the device is good. It is worth mentioning that, for the skyrmion-based transistor-like device, spin waves also can be used to drive skyrmion into motion (cf. Ch. 5) [47]. The working states can be tuned by adjusting the electric field applied to the voltage gate and the amplitude and frequency of the spin wave.

BIBLIOGRAPHY

[1] A. Bogdanov, and A. Hubert, Thermodynamically stable magnetic vortex states in magnetic crystals. J. Magn. Magn. Mater. **138**, 255–269 (1994).

[2] U. K. Rößler, A. N. Bogdanov, and C. Pfleiderer, Spontaneous skyrmion ground states in magnetic metals. Nature **442**, 797–801 (2006).

[3] A. N. Bogdanov, and U. K. Rößler, Chiral symmetry breaking in magnetic thin films and multilayers. Phys. Rev. Lett. **87**, 037203 (2001).

[4] S. Mühlbauer, B. Binz, F. Jonietz, C. Pfleiderer, A. Rosch, A. Neubauer, R. Georgii, and P. Böni, Skyrmion lattice in a chiral magnet. Science **323**, 915–919 (2009).

[5] X. Z. Yu, Y. Onose, N. Kanazawa, J. H. Park, J. H. Han, Y. Matsui, N. Nagaosa, and Y. Tokura, Real-space observation of a two-dimensional skyrmion crystal. Nature **465**, 901–904 (2010).

[6] S. Heinze, K. Bergmannvon, M. Menzel, J. Brede, A. Kubetzka, R. Wiesendanger, G. Bihlmayer, and S. Blugel, Spontaneous atomic-scale magnetic skyrmion lattice in two dimensions. Nat. Phys. **7**, 713–718 (2011).

[7] H. Du, J. P. DeGrave, F. Xue, D. Liang, W. Ning, J. Yang, M. Tian, Y. Zhang, and S. Jin, Highly stable skyrmion state in helimagnetic MnSi nanowires. Nano Lett. **14**, 2026-2032 (2014).

[8] N. Romming, A. Kubetzka, C. Hanneken, K. Bergmannvon, and R. Wiesendanger, Field-dependent size and shape of single magnetic skyrmions. Phys. Rev. Lett. **114**, 177203 (2015).

[9] G. Chen, A. Mascaraque, A. T. N'Diaye, and A. K. Schmid, Room temperature skyrmion ground state stabilized through interlayer exchange coupling. Appl. Phys. Lett. **106**, 242404 (2015).

[10] T. Matsumoto, Y.-G. So, Y. Kohno, H. Sawada, Y. Ikuhara, and N. Shibata, Direct observation of $\Sigma 7$ domain boundary core structure in magnetic skyrmion lattice. Sci. Adv. **2**, e1501280 (2016).

[11] W. Münzer, A. Neubauer, T. Adams, S. Mühlbauer, C. Franz, F. Jonietz, R. Georgii, P. Böni, B. Pedersen, M. Schmidt, A. Rosch, and C. Pfleiderer, Skyrmion lattice in the doped semiconductor $Fe_{1-x}Co_xSi$. Phys. Rev. B **81**, 041203 (2010).

[12] S. Seki, X. Z. Yu, S. Ishiwata, and Y. Tokura, Observation of skyrmions in a multiferroic material. Science **336**, 198-201 (2012).

[13] Y. Nahas, S. Prokhorenko, L. Louis, Z. Gui, I. Kornev, and L. Bellaiche, Discovery of stable skyrmionic state in ferroelectric nanocomposites. Nat. Commun. **6**, 8542 (2015).

[14] B. Dupé, G. Bihlmayer, M. Böttcher, S. Blügel, and S. Heinze, Engineering skyrmions in transition-metal multilayers for spintronics. Nat. Commun. **7**, 11779 (2016).

[15] C. Moreau-Luchaire, C. Moutafis, N. Reyren, J. Sampaio, C. A. F. Vaz, N. Van Horne, K. Bouzehouane, K. Garcia, C. Deranlot, P. Warnicke, P. Wohlhüter, J.-M. George, M. Weigand, J. Raabe, V. Cros, and A. Fert, Additive interfacial chiral interaction in multilayers for stabilization of small individual skyrmions at room temperature. Nat. Nanotechnol. **11**, 444–448 (2016).

[16] A. Soumyanarayanan, M. Raju, A. L. Gonzalez Oyarce, A. K. C. Tan, M.-Y. Im, A. P. Petrović, P. Ho, K. H. Khoo, M. Tran, C. K. Gan, F. Ernult, and C. Panagopoulos, Tunable room-temperature magnetic skyrmions in Ir/Fe/Co/Pt multilayers. Nat. Mater. **16**, 898 (2017).

[17] S. Tacchi, R. E. Troncoso, M. Ahlberg, G. Gubbiotti, M. Madami, J. Åkerman, and P. Landeros, Interfacial Dzyaloshinskii-Moriya interaction in Pt/CoFeB Films: effect of the heavy-metal thickness. Phys. Rev. Lett. **118**, 147201 (2017).

[18] G. Yu, P. Upadhyaya, X. Li, W. Li, S. K. Kim, Y. Fan, K. L. Wong, Y. Tserkovnyak, P. K. Amiri, and K. L. Wang, Room-temperature creation and spin-orbit torque manipulation of skyrmions in thin films with engineered asymmetry. Nano Lett. **16**, 1981–1988 (2016).

[19] W. Jiang, X. Zhang, G. Yu, W. Zhang, X. Wang, M. Benjamin Jungfleisch, J. E. Pearson, X. Cheng, O. Heinonen, K. L. Wang, Y. Zhou, A. Hoffmann, and S. G. E. Velthuiste, Direct observation of the skyrmion Hall effect. Nat. Phys. **13**, 162–169 (2017).

[20] K. Litzius, I. Lemesh, B. Kruger, P. Bassirian, L. Caretta, K. Richter, F. Buttner, K. Sato, O. A. Tretiakov, J. Forster, R. M. Reeve, M. Weigand, I. Bykova, H. Stoll, G. Schutz, G. S. D. Beach, and M. Klaui, Skyrmion Hall effect revealed by direct time-resolved X-ray microscopy. Nat. Phys. **13**, 170–175 (2017).

[21] F. Jonietz, S. Mühlbauer, C. Pfleiderer, A. Neubauer, W. Münzer, A. Bauer, T. Adams, R. Georgii, P. Böni, R. A. Duine, K. Everschor, M. Garst, and A. Rosch, Spin transfer torques in MnSi at ultralow current densities. Science **330**, 1648–1651 (2010).

[22] T. Schulz, R. Ritz, A. Bauer, M. Halder, M. Wagner, C. Franz, C. Pfleiderer, K. Everschor, M. Garst, and A. Rosch, Emergent electrodynamics of skyrmions in a chiral magnet. Nat. Phys. **8**, 301–304 (2012).

[23] X. Yu, N. Kanazawa, W. Zhang, T. Nagai, T. Hara, K. Kimoto, Y. Matsui, Y. Onose, and Y. Tokura, Skyrmion flow near room temperature in an ultralow current density. Nat. Commun. **3**, 988 (2012).

[24] J. Sampaio, V. Cros, S. Rohart, A. Thiaville, and A. Fert, Nucleation, stability and current-induced motion of isolated magnetic skyrmions in nanostructures. Nat. Nanotechnol. **8**, 839–844 (2013).

[25] Y. Zhou, E. Iacocca, A. A. Awad, R. K. Dumas, F. C. Zhang, H. B. Braun, and J. Akerman, Dynamically stabilized magnetic skyrmions. Nat. Commun. **6**, 8193 (2015).

[26] X. Zhang, Y. Zhou, M. Ezawa, G. P. Zhao, and W. Zhao, Magnetic skyrmion transistor: skyrmion motion in a voltage-gated nanotrack. Sci. Rep. **5**, 11369 (2015).

[27] C. Reichhardt, D. Ray, and C. J. O. Reichhardt, Magnus-induced ratchet effects for skyrmions interacting with asymmetric substrates. New J. Phys. **17**, 073034 (2015).

[28] W. Kang, Y. Huang, X. Zhang, Y. Zhou, and W. Zhao, Skyrmion-electronics: an overview and outlook. Proc. IEEE **104**, 2040-2061 (2016).

[29] X. Zhang, G. P. Zhao, H. Fangohr, J. P. Liu, W. X. Xia, J. Xia, and F. J. Morvan, Skyrmion-skyrmion and skyrmion-edge repulsions in skyrmion-based racetrack memory. Sci. Rep. **5**, 7643 (2015).

[30] X. Zhang, Y. Zhou, and M. Ezawa, Magnetic bilayer-skyrmions without skyrmion Hall effect. Nat. Commun. **7**, 10293 (2016).

[31] X. Zhang, Y. Zhou, and M. Ezawa, Antiferromagnetic skyrmion: stability, creation and manipulation. Sci. Rep. **6**, 24795 (2016).

[32] X. Zhang, J. Xia, Y. Zhou, D. Wang, X. Liu, W. Zhao, and M. Ezawa, Control and manipulation of a magnetic skyrmionium in nanostructures. Phys. Rev. B **94**, 094420 (2016).

[33] X. Zhang, M. Ezawa, and Y. Zhou, Magnetic skyrmion logic gates: conversion, duplication and merging of skyrmions. Sci. Rep. **5**, 9400 (2015).

[34] S. S. P. Parkin, M. Hayashi, and L. Thomas, Magnetic domain-wall racetrack memory. Science **320**, 190–194 (2008).

[35] A. Fert, V. Cros, and J. Sampaio, Skyrmions on the track. Nat. Nanotechnol. **8**, 152–156 (2013).

[36] N. Nagaosa, and Y. Tokura, Topological properties and dynamics of magnetic skyrmions. Nat. Nanotechnol. **8**, 899–911 (2013).

[37] A. Thiaville, S. Rohart, É. Jué, V. Cros, and A. Fert, Dynamics of Dzyaloshinskii domain walls in ultrathin magnetic films. EPL (Europhysics Letters) **100**, 57002 (2012).

[38] J. Zang, M. Mostovoy, J. H. Han, and N. Nagaosa, Dynamics of skyrmion crystals in metallic thin films. Phys. Rev. Lett. **107**, 136804 (2011).

[39] J. Barker, and O. A. Tretiakov, Static and dynamical properties of antiferromagnetic skyrmions in the presence of applied current and temperature. Phys. Rev. Lett. **116**, 147203 (2016).

[40] I. Purnama, W. L. Gan, D. W. Wong, and W. S. Lew, Guided current-induced skyrmion motion in 1D potential well. Sci. Rep. **5**, 10620 (2015).

[41] P. Lai, G. P. Zhao, H. Tang, N. Ran, S. Q. Wu, J. Xia, X. Zhang, and Y. Zhou, An improved racetrack structure for transporting a skyrmion. Sci. Rep. **7**, 45330 (2017).

[42] X. Zhang, J. Xia, G. P. Zhao, X. Liu, and Y. Zhou, Magnetic skyrmion transport in a nanotrack with spatially varying damping and non-adiabatic torque. IEEE Trans. Magn. **53**, 1-6 (2017).

[43] Y. Zhou, and M. Ezawa, A reversible conversion between a skyrmion and a domain-wall pair in a junction geometry. Nat. Commun. **5**, 4652 (2014).

[44] Y. Shiota, S. Murakami, F. Bonell, T. Nozaki, T. Shinjo, and Y. Suzuki, Quantitative evaluation of voltage-induced magnetic anisotropy change by magnetoresistance measurement. Appl. Phys. Express **4**, 043005 (2011).

[45] A. Schellekens, A. Brinkvan den, J. Franken, H. Swagten, and B. Koopmans, Electric-field control of domain wall motion in perpendicularly magnetized materials. Nat. Commun. **3**, 847 (2012).

[46] R. Verba, V. Tiberkevich, I. Krivorotov, and A. Slavin, Parametric excitation of spin waves by voltage-controlled magnetic anisotropy. Phys. Rev. Appl. **1**, 044006 (2014).

[47] J. Xia, Y. Huang, X. Zhang, W. Kang, C. Zheng, X. Liu, W. Zhao, and Y. Zhou, A microwave field-driven transistor-like skyrmionic device with the microwave current-assisted skyrmion creation. J. Appl. Phys. **122**, 153901 (2017).

CHAPTER 7

Conclusion and outlook

In this chapter, we summarize the key findings and major conclusions of this dissertation and discuss the future outlook on magnetic skyrmions in terms of materials, skyrmion structures, and external driving forces.

7.1 Conclusion

In this dissertation, we have studied the dynamics of magnetic skyrmion in nanostructures driven by either STTs or spin waves, which is important and fundamental to the design and development of advanced and emerging skyrmion-based spintronic and electronic applications.

We first demonstrate that the skyrmion driven by STTs will show the SkHE, namely, the skyrmion moves at an angle with respect to the designed driving force direction. Such an effect has recently been experimentally confirmed [1, 2] and could result in the undesired motion of skyrmion toward the sample edge in confined nanostructures [1, 2], which may ultimately lead to the destruction of skyrmion when it touches the sample edge. Hence, we propose two methods to eliminate the detrimental SkHE or avoid the skyrmion annihilation caused by the SkHE in nanostructures. For the skyrmion driven by in-plane spin currents (i.e., Zhang-Li STTs) in nanotracks, we find that the skyrmion motion can be controlled with spatially varying damping coefficient α and non-adiabatic STT coefficient β, which could prevent the detrimental effect of the SkHE. For the skyrmion driven by vertical spin currents (i.e., Slonczewski-like STTs) in nanotracks, we find that the SkHE can be totally eliminated in a SyAF multilayer structure with even number of constituting FM layers. For example, a SyAF bilayer skyrmion can move strictly along the longitudinal central line of the nanotrack. On the other hand, we have also studied the skyrmion dynamics in a 2D frustrated magnetic system with competing exchange interactions driven by STTs. We show that the dynamics of the frustrated skyrmion is different from its counterpart in the

conventional FM system, where the helicity dynamics of a frustrated skyrmion could be coupled to its center-of-mass dynamics.

We have also studied the skyrmion dynamics in thin films and nanostructures driven by spin waves. We find that the skyrmion driven by longitudinal spin waves in the nanotrack is less efficient due to the rapid damping of spin waves. The skyrmion can be effectively driven by transverse spin waves when the spin wave amplitude is smaller than the threshold that may lead to the excitation or destruction of skyrmion at the sample edge. In addition, we show the feasibility of spin-wave-driven skyrmion motion in complex nanostructures, such as L-corners, T- and Y-junctions.

After studied the skyrmion dynamics in nanostructures, we demonstrate several emerging spintronic applications based on the controllable skyrmion dynamics in nanostructures. For examples, the racetrack-type memory, which was initially proposed as an application of conventional domain walls, could be built and even more efficient based on skyrmions. The logic OR and logic AND operations can be realized based on current-driven skyrmion duplication and merging processes. We also show that a transistor-like functional device can be developed based on the voltage-controlled skyrmion dynamics in nanotracks.

7.2 Outlook

From the point of view of skyrmion materials, recent theoretical and experimental works have suggested that skyrmions can be created and stable in AFM and ferrimagnetic materials [3, 4, 5, 6]. Similar to the SyAF skyrmion, the AFM skyrmion has a zero skyrmion number and thus shows no SkHE when it is driven by an external driving force [3, 4]. The ferrimagnetic skyrmion has a non-zero skyrmion number, however, its SkHE can be much reduced in compared to the FM skyrmion [6]. Due to the absence of SkHE or reduced magnitude of SkHE, the AFM and ferrimagnetic skyrmions can reach a very high speed without being destroyed at sample edges. Therefore, AFM and ferrimagnetic skyrmions can be considered as possible information carriers with an improved performance in compared with their counterparts in conventional FM materials. We will try to explore the dynamics and other properties of AFM and ferrimagnetic skyrmions driven by STTs and spin waves in nanostructures.

From the point of view of skyrmion structures, the skyrmion structure and associated skyrmion number are determined by both the in-plane and out-of-plane spin configurations, which means the skyrmion has multiple degrees of freedom that can be controlled in principle. For example, although most studies are focusing on the ground-state Néel-type and Bloch-type skyrmions currently, several recent theoretical and experimental re-

ports have revealed that antiskyrmions [7, 8, 9] and skyrmioniums [10, 11] have special dynamic properties and can also be employed as information carriers. The skyrmion and antiskyrmion can be used to carrying different binary information bits in a same spintronic device. Namely, the skyrmion stands for digital "1", and the antiskyrmion stands for digital "0". In such a case, it is expected that information can be computed based on the manipulation of skyrmions and antiskyrmions. It is worth mentioning that both skyrmions and antiskyrmions are stable or meta-stable solutions in frustrated magnetic systems. Also, both Néel-type and Bloch-type skyrmions are stable or meta-stable solutions in frustrated magnetic systems. Hence, frustrated magnets are extremely promising for skyrmion-based applications. The skyrmionium has a zero skyrmion number, therefore it is immune from the SkHE and can be used to reliably delivery information in narrow and long nanotracks. We will study the antiskyrmion and skyrmionium dynamics in nanostructures (including conventional and frustrated magnetic materials) and design spintronic applications based on their unique dynamic behaviors.

Here at last, from the point of view of skyrmion driving forces, we have previously mentioned that skyrmions driven by electric current may be energy consuming and produce significant Joule heating, which impede the integration into actual nanoscale circuits. Therefore, as the Joule heating effect can be significantly suppressed under an electric field, the use of an electric field appears to be an efficient and robust method for manipulating skyrmions. The skyrmion-based applications driven by electric field will be designed to have ultra-low power consumption, which is a great beneficial property desired by industries. We will try to investigate the dynamics of skyrmion driven by the electric field and seek other effective methods to drive and manipulate skyrmions and their counterparts in different material systems, especially at room temperature.

BIBLIOGRAPHY

[1] W. Jiang, X. Zhang, G. Yu, W. Zhang, X. Wang, M. Benjamin Jungfleisch, J. E. Pearson, X. Cheng, O. Heinonen, K. L. Wang, Y. Zhou, A. Hoffmann, and S. G. E. Velthuiste, Direct observation of the skyrmion Hall effect. Nat. Phys. **13**, 162–169 (2017).

[2] K. Litzius, I. Lemesh, B. Kruger, P. Bassirian, L. Caretta, K. Richter, F. Buttner, K. Sato, O. A. Tretiakov, J. Forster, R. M. Reeve, M. Weigand, I. Bykova, H. Stoll, G. Schutz, G. S. D. Beach, and M. Klaui, Skyrmion Hall effect revealed by direct time-resolved X-ray microscopy. Nat. Phys. **13**, 170–175 (2017).

[3] J. Barker, and O. A. Tretiakov, Static and dynamical properties of antiferromagnetic skyrmions in the presence of applied current and temperature. Phys. Rev. Lett. **116**, 147203 (2016).

[4] X. Zhang, Y. Zhou, and M. Ezawa, Antiferromagnetic skyrmion: stability, creation and manipulation. Sci. Rep. **6**, 24795 (2016).

[5] P. Bessarab, D. Yudin, D. Gulevich, P. Wadley, M. Titov, and O. A. Tretiakov, Stability and lifetime of antiferromagnetic skyrmions. arXiv preprint arXiv:1709.04454 (2017).

[6] S. Woo, K. M. Song, X. Zhang, Y. Zhou, M. Ezawa, S. Finizio, J. Raabe, J. W. Choi, B.-C. Min, H. C. Koo, others , and , Current-driven dynamics and inhibition of the skyrmion Hall effect of ferrimagnetic skyrmions in GdFeCo films. Nat. Commun. **9**, 959 (2018).

[7] M. Hoffmann, B. Zimmermann, G. P. Müller, D. Schürhoff, N. S. Kiselev, C. Melcher, and S. Blügel, Antiskyrmions stabilized at interfaces by anisotropic Dzyaloshinskii-Moriya interactions. Nat. Commun. **8**, 308 (2017).

[8] S. Huang, C. Zhou, G. Chen, H. Shen, A. K. Schmid, K. Liu, and Y. Wu, Stabilization and current-induced motion of antiskyrmion in the presence of anisotropic Dzyaloshinskii-Moriya interaction. Phys. Rev. B **96**, 144412 (2017).

[9] A. K. Nayak, V. Kumar, T. Ma, P. Werner, E. Pippel, R. Sahoo, F. Damay, U. K. Rößler, C. Felser, and S. S. P. Parkin, Magnetic antiskyrmions above room temperature in tetragonal Heusler materials. Nature **548**, 561 (2017).

[10] X. Zhang, J. Xia, Y. Zhou, D. Wang, X. Liu, W. Zhao, and M. Ezawa, Control and manipulation of a magnetic skyrmionium in nanostructures. Phys. Rev. B **94**, 094420 (2016).

[11] S. Zhang, F. Kronast, G. Laanvan der, and T. Hesjedal, Real-space observation of skyrmionium in a ferromagnet-magnetic topological insulator heterostructure. Nano Lett. **18**, 1057–1063 (2018).

APPENDIX A

Derivation of Thiele Motion Equation

The magnetization distribution $\boldsymbol{m}(\boldsymbol{r})$ of a rigid magnetic skyrmion in 2D real space (x, y) can be expressed in terms of spherical coordinates (θ, ϕ) and the spatial variables in polar coordinates (r, φ), which is given as

$$\boldsymbol{m}(\boldsymbol{r}) = \boldsymbol{m}(\theta, \phi) = (\sin\theta\cos\phi, \sin\theta\sin\phi, \cos\theta), \tag{A.1}$$

with

$$\theta(\boldsymbol{r}) = \theta(r), \tag{A.2}$$

$$\phi(\boldsymbol{r}) = Q_{\mathrm{v}}\varphi + Q_{\mathrm{h}}, \tag{A.3}$$

$$\boldsymbol{r} = (x, y) = (r\cos\varphi, r\sin\varphi), \tag{A.4}$$

where $Q_{\mathrm{v}} \in \mathbb{Z}$ and $Q_{\mathrm{h}} \in [0, 2\pi]$ denote the vorticity and helicity of the skyrmion, respectively. For the hedgehog-like skyrmion with the lowest energy in the presence of positive DMI ($D > 0$), which is studied in the main text of this dissertation, we assume $\phi = \varphi$, that is, $Q_{\mathrm{v}} = 1$, and $Q_{\mathrm{h}} = 0$. For the hedgehog-like skyrmion with the lowest energy in the presence of negative DMI ($D < 0$), we assume $\phi = \varphi + \pi$, that is, $Q_{\mathrm{v}} = 1$, and $Q_{\mathrm{h}} = \pi$. The center of mass of the skyrmion is defined as

$$\boldsymbol{R} = (X, Y), \tag{A.5}$$

and thus the drift velocity of the skyrmion is

$$\boldsymbol{v} = \frac{\partial \boldsymbol{R}}{\partial t}. \tag{A.6}$$

Assuming that the shape of the skyrmion remains constant during its motion, that is, the skyrmion is a strictly rigid object, the skyrmion mass center as a function of time can be written as

$$\boldsymbol{m} = \boldsymbol{m}(\boldsymbol{r}, t) = \boldsymbol{m}[\boldsymbol{r} - \boldsymbol{R}(t)]. \tag{A.7}$$

Under this assumption, we have the relation for steady motion

$$\frac{\partial \boldsymbol{m}}{\partial t} = -\frac{\partial \boldsymbol{m}}{\partial(\boldsymbol{r}-\boldsymbol{R})}\frac{\partial \boldsymbol{R}}{\partial t} = -\left(\frac{\partial \boldsymbol{R}}{\partial t}\cdot\nabla\right)\boldsymbol{m} = -(\boldsymbol{v}\cdot\nabla)\boldsymbol{m}. \tag{A.8}$$

The Thiele motion equation for the magnetic skyrmion is obtained by projecting down the equation of motion onto the relevant translational modes [1, 2]. This mathematical procedure is achieved in three steps:

1. by considering the cross product of both members of Eq. (A.9) by $\boldsymbol{m}$;
2. multiplying the result with the operator $-\frac{\partial}{\partial r_i}\boldsymbol{m}$, where $r_i = x, y$;
3. integrating over the region containing the skyrmion.

A.1 Thiele equation for Slonczewski-like torques

The steady-state motion of the isolated rigid magnetic skyrmion can be well described by the Thiele equation [1]. Here, we derive the Thiele motion equation for the rigid magnetic skyrmion driven by the spatially divergent STT induced by the SHE in the ferromagnet/heavy metal heterostructure.

First, we recapitulate that the magnetization dynamics is described by the modified LLG equation that takes into account the current-induced spin Hall spin torque, which can be written as

$$\frac{d\boldsymbol{m}}{dt} = -\gamma_0\boldsymbol{m}\times\boldsymbol{h}_{\text{eff}} + \alpha(\boldsymbol{m}\times\frac{d\boldsymbol{m}}{dt}) - \tau_{\text{SH}}[\boldsymbol{m}\times(\boldsymbol{m}\times\boldsymbol{p})] - \xi\tau_{\text{SH}}(\boldsymbol{m}\times\boldsymbol{p}), \tag{A.9}$$

where t is the time, γ_0 is the gyromagnetic ratio with absolute value, α is the Gilbert damping coefficient, and ξ is the field-like STT coefficient. $\boldsymbol{h}_{\text{eff}}$ is the effective field, that is, the functional derivative of the micromagnetic energy density ε, which reads

$$\boldsymbol{h}_{\text{eff}} = -\frac{1}{\mu_0 M_{\text{S}}}\frac{\delta\varepsilon}{\delta\boldsymbol{m}}. \tag{A.10}$$

where μ_0 is the vacuum permeability. The considered micromagnetic energy in our simulation includes the exchange, anisotropy, external magnetic field, demagnetization and DMI terms. The micromagnetic energy density ε is written as follows

$$\begin{aligned}\varepsilon = {} & A(\nabla\boldsymbol{m})^2 - K(\boldsymbol{n}\cdot\boldsymbol{m})^2 \\ & - \mu_0 M_{\text{S}}\boldsymbol{m}\cdot\boldsymbol{H}_{\text{e}} - \frac{\mu_0 M_{\text{S}}}{2}\boldsymbol{m}\cdot\boldsymbol{H}_{\text{d}} \\ & + D(m_z\frac{\partial m_x}{\partial x} + m_z\frac{\partial m_y}{\partial y} - m_x\frac{\partial m_z}{\partial x} - m_y\frac{\partial m_z}{\partial y}),\end{aligned} \tag{A.11}$$

where A, K, and D are the exchange, anisotropy, and DMI constants, respectively. $\boldsymbol{H}_{\mathrm{e}}$ is the external magnetic field, and $\boldsymbol{H}_{\mathrm{d}}$ is the demagnetization field. The current-dependent coefficient for the antidamping-like spin Hall spin torque are defined as

$$\tau_{\mathrm{SH}} = \left| \frac{\gamma_0 \hbar}{2\mu_0 e} \right| \cdot \frac{j_{\mathrm{c}} \theta_{\mathrm{SH}}}{b M_{\mathrm{S}}}, \tag{A.12}$$

where $\hbar$ is the reduced Planck constant, e is the electron charge, b is the thickness of the FM layer, and j_{c} is the local charge current density in the heavy-metal layer. $\theta_{\mathrm{SH}} = j_{\mathrm{s}}/j_{\mathrm{c}} = j_{\mathrm{s}}/j_{\mathrm{e}}$ is the spin Hall angle, which is defined by the ratio between spin current density j_{s} and current density j_{c} (electron current density j_{e}). Note that the electron current direction is opposite to the charge current direction, that is, $\boldsymbol{j}_{\mathrm{e}} = -\boldsymbol{j}_{\mathrm{c}}$, while their amplitudes are the same, that is, $j_{\mathrm{e}} = j_{\mathrm{c}}$.

The detailed mathematical derivations are presented below. Since that the field-like torque term becomes zero after implementing step 2, the field-like term is not included in the following derivations. First, we rewrite Eq. (A.9) into the following form

$$0 = -\frac{\partial \boldsymbol{m}}{\partial t} - \gamma_0 \boldsymbol{m} \times \boldsymbol{h}_{\mathrm{eff}} + \alpha(\boldsymbol{m} \times \frac{\partial \boldsymbol{m}}{\partial t}) - \frac{\tau_{\mathrm{SH}}}{j_{\mathrm{e}}} \left\{ \boldsymbol{m} \times [\boldsymbol{m} \times (\boldsymbol{j}_{\mathrm{e}} \times \hat{z})] \right\}. \tag{A.13}$$

It should be mentioned that we assume a positive spin Hall angle θ_{SH} here, thus the polarization direction of the spin current in CoFeB due to the SHE in the Ta/CoFeB/MgO can be expressed as $\hat{j}_e \times \hat{z}$ [3] with $\hat{j}_e$ being the unit vector along electron flow.

And we treat all terms as equivalent fields by considering the cross product of all terms of Eq. (A.13) by $\boldsymbol{m}$,

$$\boldsymbol{H}^{\mathrm{g}} + \boldsymbol{H}^{\mathrm{e}} + \boldsymbol{H}^{\mathrm{d}} + \boldsymbol{H}^{\mathrm{c}} = 0. \tag{A.14}$$

where

$$\boldsymbol{H}^{\mathrm{g}} = -\boldsymbol{m} \times \frac{\partial \boldsymbol{m}}{\partial t}, \tag{A.15}$$

$$\boldsymbol{H}^{\mathrm{e}} = -\gamma_0 \boldsymbol{m} \times (\boldsymbol{m} \times \boldsymbol{h}_{\mathrm{eff}}), \tag{A.16}$$

$$\boldsymbol{H}^{\mathrm{d}} = \alpha \boldsymbol{m} \times (\boldsymbol{m} \times \frac{\partial \boldsymbol{m}}{\partial t}), \tag{A.17}$$

$$\boldsymbol{H}^{\mathrm{c}} = \frac{\tau_{\mathrm{SH}}}{j_{\mathrm{e}}} \boldsymbol{m} \times \left\{ \boldsymbol{m} \times [\boldsymbol{m} \times (\hat{z} \times \boldsymbol{j}_{\mathrm{e}})] \right\}, \tag{A.18}$$

where $\boldsymbol{H}^{\mathrm{g}}$ is the gyroscopic equivalent field, $\boldsymbol{H}^{\mathrm{e}}$ is the effective equivalent field, $\boldsymbol{H}^{\mathrm{d}}$ is the dissipative equivalent field, $\boldsymbol{H}^{\mathrm{c}}$ is the equivalent field related to the driving current. The force density is translated from the field with the operation of $-\frac{\partial}{\partial r_i} \boldsymbol{m} \cdot \boldsymbol{H}$,

$$\boldsymbol{f}^{\mathrm{g}} + \boldsymbol{f}^{\mathrm{e}} + \boldsymbol{f}^{\mathrm{d}} + \boldsymbol{f}^{\mathrm{c}} = 0, \tag{A.19}$$

where

$$\boldsymbol{f}^{\mathrm{g}} = -\frac{\partial}{\partial r_i}\boldsymbol{m}\cdot\boldsymbol{H}^{\mathrm{g}}, \tag{A.20}$$

$$\boldsymbol{f}^{\mathrm{e}} = -\frac{\partial}{\partial r_i}\boldsymbol{m}\cdot\boldsymbol{H}^{\mathrm{e}}, \tag{A.21}$$

$$\boldsymbol{f}^{\mathrm{d}} = -\frac{\partial}{\partial r_i}\boldsymbol{m}\cdot\boldsymbol{H}^{\mathrm{d}}, \tag{A.22}$$

$$\boldsymbol{f}^{\mathrm{c}} = -\frac{\partial}{\partial r_i}\boldsymbol{m}\cdot\boldsymbol{H}^{\mathrm{c}}. \tag{A.23}$$

We first focus on the gyroscopic force density $\boldsymbol{f}^{\mathrm{g}}$, which is corresponding to the gyroscopic equivalent field $\boldsymbol{H}^{\mathrm{g}}$. Because we have

$$\begin{aligned}\frac{\partial \boldsymbol{m}}{\partial t} =& -(\boldsymbol{v}\cdot\nabla)\boldsymbol{m} = -\left(v_x\frac{\partial}{\partial x}+v_y\frac{\partial}{\partial y}\right)\boldsymbol{m} \\ =& -\left(v_x\frac{\partial m_x}{\partial x}+v_y\frac{\partial m_x}{\partial y}\right)\hat{x}-\left(v_x\frac{\partial m_y}{\partial x}+v_y\frac{\partial m_y}{\partial y}\right)\hat{y}-\left(v_x\frac{\partial m_z}{\partial x}+v_y\frac{\partial m_z}{\partial y}\right)\hat{z},\end{aligned} \tag{A.24}$$

and

$$\boldsymbol{H}^{\mathrm{g}} = -\boldsymbol{m}\times\frac{\partial \boldsymbol{m}}{\partial t} = -\begin{vmatrix}\hat{x} & \hat{y} & \hat{z}\\ m_x & m_y & m_z\\ \frac{\partial m_x}{\partial t} & \frac{\partial m_y}{\partial t} & \frac{\partial m_z}{\partial t}\end{vmatrix} = H_x^{\mathrm{g}}\hat{x}+H_y^{\mathrm{g}}\hat{y}+H_z^{\mathrm{g}}\hat{z}. \tag{A.25}$$

We could get

$$\begin{aligned}H_x^{\mathrm{g}} =& -\left[m_y\left(\frac{\partial \boldsymbol{m}}{\partial t}\right)_z - m_z\left(\frac{\partial \boldsymbol{m}}{\partial t}\right)_y\right] \\ =& v_x m_y\frac{\partial m_z}{\partial x}+v_y m_y\frac{\partial m_z}{\partial y}-v_x m_z\frac{\partial m_y}{\partial x}-v_y m_z\frac{\partial m_y}{\partial y},\end{aligned} \tag{A.26}$$

$$\begin{aligned}H_y^{\mathrm{g}} =& -\left[m_z\left(\frac{\partial \boldsymbol{m}}{\partial t}\right)_x - m_x\left(\frac{\partial \boldsymbol{m}}{\partial t}\right)_z\right] \\ =& v_x m_z\frac{\partial m_x}{\partial x}+v_y m_z\frac{\partial m_x}{\partial y}-v_x m_x\frac{\partial m_z}{\partial x}-v_y m_x\frac{\partial m_z}{\partial y},\end{aligned} \tag{A.27}$$

$$\begin{aligned}H_z^{\mathrm{g}} =& -\left[m_x\left(\frac{\partial \boldsymbol{m}}{\partial t}\right)_y - m_y\left(\frac{\partial \boldsymbol{m}}{\partial t}\right)_x\right] \\ =& v_x m_x\frac{\partial m_y}{\partial x}+v_y m_x\frac{\partial m_y}{\partial y}-v_x m_y\frac{\partial m_x}{\partial x}-v_y m_y\frac{\partial m_x}{\partial y}.\end{aligned} \tag{A.28}$$

And then, We could have

$$
\begin{aligned}
f_x^{\mathrm{g}} =& -\left(H_x^{\mathrm{g}}\frac{\partial m_x}{\partial x}+H_y^{\mathrm{g}}\frac{\partial m_y}{\partial x}+H_z^{\mathrm{g}}\frac{\partial m_z}{\partial x}\right) \qquad \text{(A.29)}\\
=& -\left(v_x m_y\frac{\partial m_z}{\partial x}+v_y m_y\frac{\partial m_z}{\partial y}-v_x m_z\frac{\partial m_y}{\partial x}-v_y m_z\frac{\partial m_y}{\partial y}\right)\frac{\partial m_x}{\partial x}\\
&-\left(v_x m_z\frac{\partial m_x}{\partial x}+v_y m_z\frac{\partial m_x}{\partial y}-v_x m_x\frac{\partial m_z}{\partial x}-v_y m_x\frac{\partial m_z}{\partial y}\right)\frac{\partial m_y}{\partial x}\\
&-\left(v_x m_x\frac{\partial m_y}{\partial x}+v_y m_x\frac{\partial m_y}{\partial y}-v_x m_y\frac{\partial m_x}{\partial x}-v_y m_y\frac{\partial m_x}{\partial y}\right)\frac{\partial m_z}{\partial x}\\
=& -v_y m_y\frac{\partial m_z}{\partial y}\frac{\partial m_x}{\partial x}+v_y m_z\frac{\partial m_y}{\partial y}\frac{\partial m_x}{\partial x}\\
&-v_y m_z\frac{\partial m_x}{\partial y}\frac{\partial m_y}{\partial x}+v_y m_x\frac{\partial m_z}{\partial y}\frac{\partial m_y}{\partial x}\\
&-v_y m_x\frac{\partial m_y}{\partial y}\frac{\partial m_z}{\partial x}+v_y m_y\frac{\partial m_x}{\partial y}\frac{\partial m_z}{\partial x}\\
=& v_y\boldsymbol{m}\cdot\left(\frac{\partial \boldsymbol{m}}{\partial x}\times\frac{\partial \boldsymbol{m}}{\partial y}\right),\\
f_y^{\mathrm{g}} =& -\left(H_x^{\mathrm{g}}\frac{\partial m_x}{\partial y}+H_y^{\mathrm{g}}\frac{\partial m_y}{\partial y}+H_z^{\mathrm{g}}\frac{\partial m_z}{\partial y}\right) \qquad \text{(A.30)}\\
=& -\left(v_x m_y\frac{\partial m_z}{\partial x}+v_y m_y\frac{\partial m_z}{\partial y}-v_x m_z\frac{\partial m_y}{\partial x}-v_y m_z\frac{\partial m_y}{\partial y}\right)\frac{\partial m_x}{\partial y}\\
&-\left(v_x m_z\frac{\partial m_x}{\partial x}+v_y m_z\frac{\partial m_x}{\partial y}-v_x m_x\frac{\partial m_z}{\partial x}-v_y m_x\frac{\partial m_z}{\partial y}\right)\frac{\partial m_y}{\partial y}\\
&-\left(v_x m_x\frac{\partial m_y}{\partial x}+v_y m_x\frac{\partial m_y}{\partial y}-v_x m_y\frac{\partial m_x}{\partial x}-v_y m_y\frac{\partial m_x}{\partial y}\right)\frac{\partial m_z}{\partial y}\\
=& -v_x m_y\frac{\partial m_z}{\partial x}\frac{\partial m_x}{\partial y}+v_x m_z\frac{\partial m_y}{\partial x}\frac{\partial m_x}{\partial y}\\
&-v_x m_z\frac{\partial m_x}{\partial x}\frac{\partial m_y}{\partial y}+v_x m_x\frac{\partial m_z}{\partial x}\frac{\partial m_y}{\partial y}\\
&-v_x m_x\frac{\partial m_y}{\partial x}\frac{\partial m_z}{\partial y}+v_x m_y\frac{\partial m_x}{\partial x}\frac{\partial m_z}{\partial y}\\
=& -v_x\boldsymbol{m}\cdot\left(\frac{\partial \boldsymbol{m}}{\partial x}\times\frac{\partial \boldsymbol{m}}{\partial y}\right),\\
f_z^{\mathrm{g}} =& -\left(H_x^{\mathrm{g}}\frac{\partial m_x}{\partial z}+H_y^{\mathrm{g}}\frac{\partial m_y}{\partial z}+H_z^{\mathrm{g}}\frac{\partial m_z}{\partial z}\right)=0. \qquad \text{(A.31)}
\end{aligned}
$$

The gyroscopic force density can be written as

$$
\begin{aligned}
\boldsymbol{f}^{\mathrm{g}} =& \left(v_y\boldsymbol{m}\cdot\left(\frac{\partial \boldsymbol{m}}{\partial x}\times\frac{\partial \boldsymbol{m}}{\partial y}\right),-v_x\boldsymbol{m}\cdot\left(\frac{\partial \boldsymbol{m}}{\partial x}\times\frac{\partial \boldsymbol{m}}{\partial y}\right),0\right) \qquad \text{(A.32)}\\
=& \boldsymbol{g}\times\boldsymbol{v},
\end{aligned}
$$

with the gyrocoupling vector density $\boldsymbol{g} = \left(0, 0, -\frac{\partial \boldsymbol{m}}{\partial x} \times \frac{\partial \boldsymbol{m}}{\partial y}\right)$.

For the effective equivalent field $\boldsymbol{H}^e$, its integral vanishes due to the translational invariance [4].

$$\boldsymbol{f}^{\mathrm{e}} = 0. \tag{A.33}$$

The dissipative equivalent field term is

$$\boldsymbol{H}^{\mathrm{d}} = \alpha \boldsymbol{m} \times (\boldsymbol{m} \times \frac{\partial \boldsymbol{m}}{\partial t}) = -\alpha \frac{\partial \boldsymbol{m}}{\partial t} \tag{A.34}$$

$$= \alpha \left[\left(v_x \frac{\partial m_x}{\partial x} + v_y \frac{\partial m_x}{\partial y} \right) \hat{x} + \left(v_x \frac{\partial m_y}{\partial x} + v_y \frac{\partial m_y}{\partial y} \right) \hat{y} + \left(v_x \frac{\partial m_z}{\partial x} + v_y \frac{\partial m_z}{\partial y} \right) \hat{z} \right], \tag{A.35}$$

with $\boldsymbol{m} \perp \frac{\partial \boldsymbol{m}}{\partial t}$ which can be seen from Eq. A.9. We also could get

$$H_x^{\mathrm{d}} = \alpha \left(v_x \frac{\partial m_x}{\partial x} + v_y \frac{\partial m_x}{\partial y} \right), \tag{A.36}$$

$$H_y^{\mathrm{d}} = \alpha \left(v_x \frac{\partial m_y}{\partial x} + v_y \frac{\partial m_y}{\partial y} \right), \tag{A.37}$$

$$H_z^{\mathrm{d}} = \alpha \left(v_x \frac{\partial m_z}{\partial x} + v_y \frac{\partial m_z}{\partial y} \right), \tag{A.38}$$

and

$$
\begin{aligned}
f_x^{\mathrm{d}} =& -\frac{\partial}{\partial x}\boldsymbol{m}\cdot\boldsymbol{H}^{\mathrm{d}} && \text{(A.39)}\\
=& -\left(H_x^{\mathrm{d}}\frac{\partial m_x}{\partial x}+H_y^{\mathrm{d}}\frac{\partial m_y}{\partial x}+H_z^{\mathrm{d}}\frac{\partial m_z}{\partial x}\right)\\
=& -\alpha\frac{\partial m_x}{\partial x}\left(v_x\frac{\partial m_x}{\partial x}+v_y\frac{\partial m_x}{\partial y}\right)-\alpha\frac{\partial m_y}{\partial x}\left(v_x\frac{\partial m_y}{\partial x}+v_y\frac{\partial m_y}{\partial y}\right)\\
&-\alpha\frac{\partial m_z}{\partial x}\left(v_x\frac{\partial m_z}{\partial x}+v_y\frac{\partial m_z}{\partial y}\right)\\
=& -\alpha\left(v_x\frac{\partial\boldsymbol{m}}{\partial x}\cdot\frac{\partial\boldsymbol{m}}{\partial x}+v_y\frac{\partial\boldsymbol{m}}{\partial x}\cdot\frac{\partial\boldsymbol{m}}{\partial y}\right),\\
f_y^{\mathrm{d}} =& -\frac{\partial}{\partial y}\boldsymbol{m}\cdot\boldsymbol{H}^{\mathrm{d}} && \text{(A.40)}\\
=& -\left(H_x^{\mathrm{d}}\frac{\partial m_x}{\partial y}+H_y^{\mathrm{d}}\frac{\partial m_y}{\partial y}+H_z^{\mathrm{d}}\frac{\partial m_z}{\partial y}\right)\\
=& -\alpha\frac{\partial m_x}{\partial y}\left(v_x\frac{\partial m_x}{\partial x}+v_y\frac{\partial m_x}{\partial y}\right)-\alpha\frac{\partial m_y}{\partial y}\left(v_x\frac{\partial m_y}{\partial x}+v_y\frac{\partial m_y}{\partial y}\right)\\
&-\alpha\frac{\partial m_z}{\partial y}\left(v_x\frac{\partial m_z}{\partial x}+v_y\frac{\partial m_z}{\partial y}\right)\\
=& -\alpha\left(v_x\frac{\partial\boldsymbol{m}}{\partial x}\cdot\frac{\partial\boldsymbol{m}}{\partial y}+v_y\frac{\partial\boldsymbol{m}}{\partial y}\cdot\frac{\partial\boldsymbol{m}}{\partial y}\right),\\
f_z^{\mathrm{d}} =& -\left(H_x^{\mathrm{d}}\frac{\partial m_x}{\partial z}+H_y^{\mathrm{d}}\frac{\partial m_y}{\partial z}+H_z^{\mathrm{d}}\frac{\partial m_z}{\partial z}\right)=0. && \text{(A.41)}
\end{aligned}
$$

The dissipative force density could be written as

$$\boldsymbol{f}^{\mathrm{d}}=-\alpha\boldsymbol{d}\cdot\boldsymbol{v}, \tag{A.42}$$

where the dissipative force tensor density tensor $\boldsymbol{d}=\begin{pmatrix}d_{xx} & d_{xy}\\ d_{yx} & d_{yy}\end{pmatrix}$ with $d_{xx}=\frac{\partial\boldsymbol{m}}{\partial x}\cdot\frac{\partial\boldsymbol{m}}{\partial x}$, $d_{yy}=\frac{\partial\boldsymbol{m}}{\partial y}\cdot\frac{\partial\boldsymbol{m}}{\partial y}$, and $d_{xy}=d_{yx}=\frac{\partial\boldsymbol{m}}{\partial x}\cdot\frac{\partial\boldsymbol{m}}{\partial y}$.

The equivalent field related to the driving current

$$
\begin{aligned}
\boldsymbol{H}^{\mathrm{c}} =& \frac{\tau_{\mathrm{SH}}}{j_{\mathrm{e}}}\boldsymbol{m}\times\{\boldsymbol{m}\times[\boldsymbol{m}\times(\hat{z}\times\boldsymbol{j}_{\mathrm{e}})]\} && \text{(A.43)}\\
=& \frac{\tau_{\mathrm{SH}}}{j_{\mathrm{e}}}\left[j_x m_z\hat{x}+j_y m_z\hat{y}-\left(j_x m_x+j_y m_y\right)\hat{z}\right], && \text{(A.44)}
\end{aligned}
$$

we could get

$$
\begin{aligned}
H_x^{\mathrm{c}} &= \frac{\tau_{\mathrm{SH}}}{j_{\mathrm{e}}}j_x m_z\hat{x}, && \text{(A.45)}\\
H_y^{\mathrm{c}} &= \frac{\tau_{\mathrm{SH}}}{j_{\mathrm{e}}}j_y m_z\hat{y}, && \text{(A.46)}\\
H_z^{\mathrm{c}} &= -\frac{\tau_{\mathrm{SH}}}{j_{\mathrm{e}}}\left(j_x m_x+j_y m_y\right)\hat{z}. && \text{(A.47)}
\end{aligned}
$$

and

$$
\begin{aligned}
f_x^{\mathrm{c}} &= -\frac{\partial}{\partial x}\boldsymbol{m}\cdot\boldsymbol{H}^{\mathrm{c}} \qquad \text{(A.48)}\\
&= -\left(H_x^{\mathrm{c}}\frac{\partial m_x}{\partial x}+H_y^{\mathrm{c}}\frac{\partial m_y}{\partial x}+H_z^{\mathrm{c}}\frac{\partial m_z}{\partial x}\right)\\
&= -\frac{\tau_{\mathrm{SH}}}{j_{\mathrm{e}}}\left(j_x m_z\frac{\partial m_x}{\partial x}+j_y m_z\frac{\partial m_y}{\partial x}-j_x m_x\frac{\partial m_z}{\partial x}-j_y m_y\frac{\partial m_z}{\partial x}\right)\\
&= -\frac{\tau_{\mathrm{SH}}}{j_{\mathrm{e}}}\left[j_x\left(m_z\frac{\partial m_x}{\partial x}-m_x\frac{\partial m_z}{\partial x}\right)+j_y\left(m_z\frac{\partial m_y}{\partial x}-m_y\frac{\partial m_z}{\partial x}\right)\right]\\
&= -\frac{\tau_{\mathrm{SH}}}{j_{\mathrm{e}}}\left[-j_x\left(\frac{\partial\boldsymbol{m}}{\partial x}\times\boldsymbol{m}\right)_y+j_y\left(\frac{\partial\boldsymbol{m}}{\partial x}\times\boldsymbol{m}\right)_x\right],\\
f_y^{\mathrm{c}} &= -\frac{\partial}{\partial y}\boldsymbol{m}\cdot\boldsymbol{H}^{\mathrm{c}} \qquad \text{(A.49)}\\
&= -\left(H_x^{\mathrm{c}}\frac{\partial m_x}{\partial y}+H_y^{\mathrm{c}}\frac{\partial m_y}{\partial y}+H_z^{\mathrm{c}}\frac{\partial m_z}{\partial y}\right)\\
&= -\frac{\tau_{\mathrm{SH}}}{j_{\mathrm{e}}}\left(j_x m_z\frac{\partial m_x}{\partial y}+j_y m_z\frac{\partial m_y}{\partial x}-j_x m_x\frac{\partial m_z}{\partial y}-j_y m_y\frac{\partial m_z}{\partial y}\right)\\
&= -\frac{\tau_{\mathrm{SH}}}{j_{\mathrm{e}}}\left[j_x\left(m_z\frac{\partial m_x}{\partial y}-m_x\frac{\partial m_z}{\partial y}\right)+j_y\left(m_z\frac{\partial m_y}{\partial y}-m_y\frac{\partial m_z}{\partial y}\right)\right]\\
&= -\frac{\tau_{\mathrm{SH}}}{j_{\mathrm{e}}}\left[-j_x\left(\frac{\partial\boldsymbol{m}}{\partial y}\times\boldsymbol{m}\right)_y+j_y\left(\frac{\partial\boldsymbol{m}}{\partial y}\times\boldsymbol{m}\right)_x\right],\\
f_z^{\mathrm{c}} &= -\frac{\partial}{\partial z}\boldsymbol{m}\cdot\boldsymbol{H}^{\mathrm{c}}=0. \qquad \text{(A.50)}
\end{aligned}
$$

The driving force density can be expressed as

$$\boldsymbol{f}^{\mathrm{c}} = -\frac{\tau_{\mathrm{SH}}}{j_{\mathrm{e}}}\boldsymbol{i}\cdot\boldsymbol{j}_{\mathrm{e}}, \qquad \text{(A.51)}$$

where the driving force tensor density tensor $\boldsymbol{i}=\begin{pmatrix}-i_{xy} & i_{xx}\\ -i_{yy} & i_{yx}\end{pmatrix}$ with $i_{xy}=\left(\frac{\partial\boldsymbol{m}}{\partial x}\times\boldsymbol{m}\right)_y$, $i_{xx}=\left(\frac{\partial\boldsymbol{m}}{\partial x}\times\boldsymbol{m}\right)_x$, $i_{yy}=\left(\frac{\partial\boldsymbol{m}}{\partial y}\times\boldsymbol{m}\right)_y$, and $i_{yx}=\left(\frac{\partial\boldsymbol{m}}{\partial y}\times\boldsymbol{m}\right)_x$.

Integrating Eq. A.19 over the area including the magnetic skyrmion, we can get the steady motion equation,

$$\boldsymbol{G}\times\boldsymbol{v}-\alpha\boldsymbol{\mathcal{D}}\cdot\boldsymbol{v}-4\pi\boldsymbol{\mathcal{B}}\cdot\boldsymbol{j}_{\mathrm{e}}=0. \qquad \text{(A.52)}$$

The first term of Eq. A.52 is the Magnus force term with the gyromagnetic coupling vector

$$
\begin{aligned}
\boldsymbol{G} &= \iint \boldsymbol{g}\,dx\,dy \qquad \text{(A.53)}\\
&= (0,0,-4\pi Q),
\end{aligned}
$$

where

$$Q = \frac{1}{4\pi} \iint \frac{\partial \boldsymbol{m}}{\partial x} \times \frac{\partial \boldsymbol{m}}{\partial y} \, dx \, dy. \tag{A.54}$$

The second term is of Eq. A.52 is the dissipative force term with the dissipative tensor

$$\boldsymbol{\mathcal{D}} = 4\pi \begin{pmatrix} \mathcal{D}_{xx} & \mathcal{D}_{xy} \\ \mathcal{D}_{yx} & \mathcal{D}_{yy} \end{pmatrix}, \tag{A.55}$$

where

$$\mathcal{D}_{xx} = \frac{1}{4\pi} \iint \frac{\partial \boldsymbol{m}}{\partial x} \cdot \frac{\partial \boldsymbol{m}}{\partial x} \, dx \, dy, \tag{A.56}$$

$$\mathcal{D}_{yy} = \frac{1}{4\pi} \iint \frac{\partial \boldsymbol{m}}{\partial y} \cdot \frac{\partial \boldsymbol{m}}{\partial y} \, dx \, dy, \tag{A.57}$$

$$\mathcal{D}_{xy} = \frac{1}{4\pi} \iint \frac{\partial \boldsymbol{m}}{\partial x} \cdot \frac{\partial \boldsymbol{m}}{\partial y} \, dx \, dy, \tag{A.58}$$

$$\mathcal{D}_{yx} = \frac{1}{4\pi} \iint \frac{\partial \boldsymbol{m}}{\partial y} \cdot \frac{\partial \boldsymbol{m}}{\partial x} \, dx \, dy. \tag{A.59}$$

The third term of Eq. A.52 is the driving force term with the tensor

$$\boldsymbol{\mathcal{B}} = \frac{\tau_{\mathrm{SH}}}{j_{\mathrm{e}}} \begin{pmatrix} -I_{xy} & I_{xx} \\ -I_{yy} & I_{yx} \end{pmatrix}, \tag{A.60}$$

where

$$I_{xx} = \frac{1}{4\pi} \iint \left(\frac{\partial \boldsymbol{m}}{\partial x} \times \boldsymbol{m} \right)_x \, dx \, dy, \tag{A.61}$$

$$I_{yy} = \frac{1}{4\pi} \iint \left(\frac{\partial \boldsymbol{m}}{\partial y} \times \boldsymbol{m} \right)_y \, dx \, dy, \tag{A.62}$$

$$I_{xy} = \frac{1}{4\pi} \iint \left(\frac{\partial \boldsymbol{m}}{\partial x} \times \boldsymbol{m} \right)_y \, dx \, dy, \tag{A.63}$$

$$I_{yx} = \frac{1}{4\pi} \iint \left(\frac{\partial \boldsymbol{m}}{\partial y} \times \boldsymbol{m} \right)_x \, dx \, dy. \tag{A.64}$$

The motion equation, Eq. A.52, can be rewritten into the following form

$$\begin{pmatrix} 4\pi Q v_y \\ -4\pi Q v_x \end{pmatrix} - 4\pi\alpha \begin{pmatrix} \mathcal{D}_{xx} & \mathcal{D}_{xy} \\ \mathcal{D}_{yx} & \mathcal{D}_{yy} \end{pmatrix} \begin{pmatrix} v_x \\ v_y \end{pmatrix} - 4\pi \frac{\tau_{\mathrm{SH}}}{j_{\mathrm{e}}} \begin{pmatrix} -I_{xy} & I_{xx} \\ -I_{yy} & I_{yx} \end{pmatrix} \begin{pmatrix} j_x \\ j_y \end{pmatrix} = 0. \tag{A.65}$$

For the isolated magnetic skyrmion in this article, we always have

$$\mathcal{D}_{xx} = \mathcal{D}_{yy} = \mathcal{D}, \mathcal{D}_{xy} = \mathcal{D}_{yx} = 0, \tag{A.66}$$

and

$$I_{xx} = I_{yy} = 0, I_{xy} = -I_{yx} = I. \tag{A.67}$$

Finally, we could get the velocity of the isolated magnetic skyrmion,

$$v_x = \frac{\tau_{\mathrm{SH}} I}{j_{\mathrm{e}}} \frac{\alpha \mathcal{D} j_x + Q j_y}{Q^2 + \alpha^2 \mathcal{D}^2}, \tag{A.68}$$

$$v_y = \frac{\tau_{\mathrm{SH}} I}{j_{\mathrm{e}}} \frac{\alpha \mathcal{D} j_y - Q j_x}{Q^2 + \alpha^2 \mathcal{D}^2}. \tag{A.69}$$

and the value of I and $\mathcal{D}$ in this article are also positive. Hence, for electron current flow j_{e} along the x direction ($j_y = 0$), the motion of isolated skyrmion can be described with

$$v_x = \frac{\tau_{\mathrm{SH}} I}{j_{\mathrm{e}}} \frac{\alpha \mathcal{D} j_x}{Q^2 + \alpha^2 \mathcal{D}^2}, \tag{A.70}$$

$$v_y = -\frac{\tau_{\mathrm{SH}} I}{j_{\mathrm{e}}} \frac{Q j_x}{Q^2 + \alpha^2 \mathcal{D}^2}. \tag{A.71}$$

The ratio of in-plane velocity components to be written as

$$\frac{v_y}{v_x} = -\frac{Q}{\alpha \mathcal{D}}. \tag{A.72}$$

In the nanotrack, when the skyrmion is driven by the spin current, the skyrmion will have a transverse displacement. When the net force of driving force and repulsion force from the edge are zero in the transverse direction, the skyrmion will moves in straight line. The Thiele equation for the motion of skyrmion in the nanotrack can be rewritten as

$$\boldsymbol{G} \times \boldsymbol{v} - \alpha \boldsymbol{\mathcal{D}} \cdot \boldsymbol{v} - 4\pi \boldsymbol{\mathcal{B}} \cdot \boldsymbol{j}_{\mathrm{e}} + \boldsymbol{F} = 0. \tag{A.73}$$

For the steady motion of skyrmion, we have $\boldsymbol{j_e} = (j_x, 0), F_x = 0, v_y = 0$ [5, 6]. Then we find

$$v_x = \frac{\tau_{\mathrm{SH}} I}{\alpha \mathcal{D}}, v_y = 0. \tag{A.74}$$

A.2 Thiele equation for Zhang-Li torques

The LLG equation for the skyrmion motion driven by the Zhang-Li torques can be written as

$$\frac{d\boldsymbol{m}}{dt} = -\gamma_0 \boldsymbol{m} \times \boldsymbol{h}_{\mathrm{eff}} + \alpha(\boldsymbol{m} \times \frac{d\boldsymbol{m}}{dt}) + \frac{\tau_{\mathrm{AD}}}{j_{\mathrm{c}}}(\boldsymbol{j}_{\mathrm{c}} \cdot \nabla)\boldsymbol{m} - \beta \frac{\tau_{\mathrm{AD}}}{j_{\mathrm{c}}}[\boldsymbol{m} \times (\boldsymbol{j}_{\mathrm{c}} \cdot \nabla)\boldsymbol{m}], \tag{A.75}$$

$$\frac{d\boldsymbol{m}}{dt} = -\gamma_0 \boldsymbol{m} \times \boldsymbol{h}_{\mathrm{eff}} + \alpha(\boldsymbol{m} \times \frac{d\boldsymbol{m}}{dt}) - \frac{\tau_{\mathrm{AD}}}{j_{\mathrm{e}}}(\boldsymbol{j}_{\mathrm{e}} \cdot \nabla)\boldsymbol{m} + \beta \frac{\tau_{\mathrm{AD}}}{j_{\mathrm{e}}}[\boldsymbol{m} \times (\boldsymbol{j}_{\mathrm{e}} \cdot \nabla)\boldsymbol{m}], \tag{A.76}$$

where $\tau_{\mathrm{AD}} = \left|\frac{\gamma_0 \hbar}{2\mu_0 e}\right| \cdot \frac{j_{\mathrm{c}} P}{b M_{\mathrm{S}}}$, β represents the strength of the non-adiabatic STT relative to the strength of the adiabatic STT, and P is the spin polarization rate of the current.

We rewrite the Eq. A.76 into the following form.

$$0 = -\frac{d\boldsymbol{m}}{dt} - \gamma_0 \boldsymbol{m} \times \boldsymbol{h}_{\text{eff}} + \alpha(\boldsymbol{m} \times \frac{d\boldsymbol{m}}{dt}) - \frac{\tau_{\text{AD}}}{j_{\text{e}}}(\boldsymbol{j}_{\text{e}} \cdot \nabla)\boldsymbol{m} + \beta \frac{\tau_{\text{AD}}}{j_{\text{e}}}[\boldsymbol{m} \times (\boldsymbol{j}_{\text{e}} \cdot \nabla)\boldsymbol{m}], \quad \text{(A.77)}$$

and treat all terms as equivalent fields by considering the cross product of all terms of Eq. (A.77) by $\boldsymbol{m}$,

$$\boldsymbol{H}^{\text{g}} + \boldsymbol{H}^{\text{e}} + \boldsymbol{H}^{\text{d}} + \boldsymbol{H}^{\text{cAD}} + \boldsymbol{H}^{\text{cnAD}} = 0. \quad \text{(A.78)}$$

where

$$\boldsymbol{H}^{\text{g}} = -\boldsymbol{m} \times \frac{\partial \boldsymbol{m}}{\partial t}, \quad \text{(A.79)}$$

$$\boldsymbol{H}^{\text{e}} = -\gamma_0 \boldsymbol{m} \times (\boldsymbol{m} \times \boldsymbol{h}_{\text{eff}}), \quad \text{(A.80)}$$

$$\boldsymbol{H}^{\text{d}} = \alpha \boldsymbol{m} \times (\boldsymbol{m} \times \frac{\partial \boldsymbol{m}}{\partial t}), \quad \text{(A.81)}$$

$$\boldsymbol{H}^{\text{cAD}} = -\frac{\tau_{\text{AD}}}{j_{\text{e}}} \boldsymbol{m} \times [(\boldsymbol{j}_{\text{e}} \cdot \nabla)\boldsymbol{m}], \quad \text{(A.82)}$$

$$\boldsymbol{H}^{\text{cnAD}} = \beta \frac{\tau_{\text{AD}}}{j_{\text{e}}} \boldsymbol{m} \times [\boldsymbol{m} \times (\boldsymbol{j}_{\text{e}} \cdot \nabla)\boldsymbol{m}], \quad \text{(A.83)}$$

where $\boldsymbol{H}^{\text{g}}$ is the gyroscopic equivalent field, $\boldsymbol{H}^{\text{e}}$ is the effective equivalent field, $\boldsymbol{H}^{\text{d}}$ is the dissipative equivalent field, $\boldsymbol{H}^{\text{cAD}}$ and $\boldsymbol{H}^{\text{cnAD}}$ are the equivalent fields related to the driving current. Compared with Eq. A.15, Eq. A.16, and Eq. A.17, the gyroscopic, effective, and dissipative equivalent fields have the same form as their counterparts in the case of CPP geometry. So, here we only focus on the different terms, $\boldsymbol{H}^{\text{cAD}}$ and $\boldsymbol{H}^{\text{cnAD}}$.

The driving force density can be translated from the corresponding equivalent field with the operation of $-\frac{\partial}{\partial r_i}\boldsymbol{m} \cdot \boldsymbol{H}$,

$$\boldsymbol{f}^{\text{cAD}} = -\frac{\partial}{\partial r_i} \boldsymbol{m} \cdot \boldsymbol{H}^{\text{cAD}}, \quad \text{(A.84)}$$

and

$$\boldsymbol{f}^{\text{cnAD}} = -\frac{\partial}{\partial r_i} \boldsymbol{m} \cdot \boldsymbol{H}^{\text{cnAD}}. \quad \text{(A.85)}$$

We could get

$$f_x^{\text{cAD}} = -\frac{\partial}{\partial x}\boldsymbol{m} \cdot \boldsymbol{H}^{\text{cAD}} = -\frac{\tau_{\text{AD}}}{j_{\text{e}}} j_y \boldsymbol{m} \cdot \left(\frac{\partial \boldsymbol{m}}{\partial x} \times \frac{\partial \boldsymbol{m}}{\partial y} \right), \quad \text{(A.86)}$$

$$f_y^{\text{cAD}} = -\frac{\partial}{\partial y}\boldsymbol{m} \cdot \boldsymbol{H}^{\text{cAD}} = \frac{\tau_{\text{AD}}}{j_{\text{e}}} j_x \boldsymbol{m} \cdot \left(\frac{\partial \boldsymbol{m}}{\partial x} \times \frac{\partial \boldsymbol{m}}{\partial y} \right), \quad \text{(A.87)}$$

$$f_y^{\text{cAD}} = -\frac{\partial}{\partial z}\boldsymbol{m} \cdot \boldsymbol{H}^{\text{cAD}} = 0. \quad \text{(A.88)}$$

f^{cAD} can be rewritten as

$$\begin{aligned} f^{\mathrm{cAD}} &= \left(-\frac{\tau_{\mathrm{AD}}}{j_{\mathrm{e}}} j_y \boldsymbol{m} \cdot \left(\frac{\partial \boldsymbol{m}}{\partial x} \times \frac{\partial \boldsymbol{m}}{\partial y} \right), \frac{\tau_{\mathrm{AD}}}{j_{\mathrm{e}}} j_x \boldsymbol{m} \cdot \left(\frac{\partial \boldsymbol{m}}{\partial x} \times \frac{\partial \boldsymbol{m}}{\partial y} \right), 0 \right) \\ &= - \boldsymbol{g} \times \boldsymbol{v}^{\mathrm{s}}, \end{aligned} \tag{A.89}$$

with the gyrocoupling vector density $\boldsymbol{g} = \left(0, 0, -\frac{\partial \boldsymbol{m}}{\partial x} \times \frac{\partial \boldsymbol{m}}{\partial y}\right)$ and the velocity of the conduction electrons $\boldsymbol{v}^{\mathrm{s}} = \frac{\tau_{\mathrm{AD}}}{j_{\mathrm{e}}}(j_x, j_y, 0)$.

The driving force density related to the non-adiabatic term is

$$\begin{aligned} f_x^{\mathrm{cnAD}} =& - \frac{\partial}{\partial x} \boldsymbol{m} \cdot \boldsymbol{H}^{\mathrm{cnAD}} \\ =& \beta \frac{\tau_{\mathrm{AD}}}{j_{\mathrm{e}}} \left[j_x \left(\frac{\partial \boldsymbol{m}}{\partial x} \cdot \frac{\partial \boldsymbol{m}}{\partial x} \right) + j_y \left(\frac{\partial \boldsymbol{m}}{\partial x} \cdot \frac{\partial \boldsymbol{m}}{\partial y} \right) \right] \end{aligned} \tag{A.90}$$

$$\begin{aligned} f_y^{\mathrm{cnAD}} =& - \frac{\partial}{\partial y} \boldsymbol{m} \cdot \boldsymbol{H}^{\mathrm{cnAD}} \\ =& \beta \frac{\tau_{\mathrm{AD}}}{j_{\mathrm{e}}} \left[j_x \left(\frac{\partial \boldsymbol{m}}{\partial x} \cdot \frac{\partial \boldsymbol{m}}{\partial y} \right) + j_y \left(\frac{\partial \boldsymbol{m}}{\partial y} \cdot \frac{\partial \boldsymbol{m}}{\partial y} \right) \right], \end{aligned} \tag{A.91}$$

$$\begin{aligned} f_y^{\mathrm{cnAD}} =& - \frac{\partial}{\partial z} \boldsymbol{m} \cdot \boldsymbol{H}^{\mathrm{cnAD}} \\ =& 0. \end{aligned} \tag{A.92}$$

f^{cnAD} can be rewritten as

$$f^{\mathrm{cnAD}} = \beta \boldsymbol{d} \cdot \boldsymbol{v}^{\mathrm{s}}. \tag{A.93}$$

Integrating the force density over the area including the magnetic skyrmion, the motion equation can be rewritten into the following form

$$\boldsymbol{G} \times (\boldsymbol{v} - \boldsymbol{v}^{\mathrm{s}}) + \boldsymbol{\mathcal{D}} (\beta \boldsymbol{v}^{\mathrm{s}} - \alpha \boldsymbol{v}) = 0. \tag{A.94}$$

The velocity can be found as

$$v_x = \frac{\tau_{\mathrm{AD}}}{j_{\mathrm{e}}} \frac{(-\beta Q \mathcal{D}_{yx} - Q^2 + \alpha\beta \mathcal{D}_{xy}\mathcal{D}_{yx} - \alpha\beta \mathcal{D}_{xx}\mathcal{D}_{yy} + \alpha Q \mathcal{D}_{xy}) j_x + (\alpha - \beta) Q \mathcal{D}_{yy} j_y}{\alpha^2 (\mathcal{D}_{xy}\mathcal{D}_{yx} - \mathcal{D}_{xx}\mathcal{D}_{yy}) + \alpha Q (\mathcal{D}_{xy} - \mathcal{D}_{yx}) - Q^2}, \tag{A.95}$$

$$v_y = \frac{\tau_{\mathrm{AD}}}{j_{\mathrm{e}}} \frac{(-\alpha + \beta) Q \mathcal{D}_{xx} j_x + (\alpha\beta \mathcal{D}_{xy}\mathcal{D}_{yx} - \alpha\beta \mathcal{D}_{xx}\mathcal{D}_{yy} - \alpha Q \mathcal{D}_{yx} + \beta Q \mathcal{D}_{xy} - Q^2) j_y}{\alpha^2 (\mathcal{D}_{xy}\mathcal{D}_{yx} - \mathcal{D}_{xx}\mathcal{D}_{yy}) + \alpha Q (\mathcal{D}_{xy} - \mathcal{D}_{yx}) - Q^2}. \tag{A.96}$$

For the isolated magnetic skyrmion in this article, we always have Eq. A.66, thus, the velocities Eq. A.95 and Eq. A.96 can be simplified as

$$v_x = \frac{\tau_{\mathrm{AD}}}{j_{\mathrm{e}}} \frac{(\alpha\beta \mathcal{D}^2 + Q^2) j_x + (-\alpha + \beta) \mathcal{D} Q j_y}{\alpha^2 \mathcal{D}^2 + Q^2}, \tag{A.97}$$

$$v_y = \frac{\tau_{\mathrm{AD}}}{j_{\mathrm{e}}} \frac{(\alpha - \beta) \mathcal{D} Q j_x + (\alpha\beta \mathcal{D}^2 + Q^2) j_y}{\alpha^2 \mathcal{D}^2 + Q^2}. \tag{A.98}$$

For electron current flow along the x direction, $\boldsymbol{j_e} = (j_x, 0)$, the motion of isolated skyrmion can be described with

$$v_x = \tau_{\mathrm{AD}} \frac{(\alpha\beta\mathcal{D}^2 + Q^2)}{\alpha^2\mathcal{D}^2 + Q^2}, \tag{A.99}$$

$$v_y = \tau_{\mathrm{AD}} \frac{(\alpha - \beta)\mathcal{D}Q}{\alpha^2\mathcal{D}^2 + Q^2}. \tag{A.100}$$

In the nanotrack, the skyrmion experiences the driving force and the force from edge. Then, the Thiele equation for the steady motion of skyrmion becomes

$$\boldsymbol{G} \times (\boldsymbol{v} - \boldsymbol{v}^{\mathrm{s}}) + \boldsymbol{\mathcal{D}} (\beta\boldsymbol{v}^{\mathrm{s}} - \alpha\boldsymbol{v}) + \boldsymbol{F} = 0. \tag{A.101}$$

For the steady motion of skyrmion in the nanotrack, we have $\boldsymbol{j_e} = (j_x, 0), F_x = 0$, and $v_y = 0$ [5, 6]. Then we obtain

$$v_x = \frac{\beta\tau_{\mathrm{AD}}}{\alpha}, v_y = 0. \tag{A.102}$$

BIBLIOGRAPHY

[1] A. A. Thiele, Steady-state motion of magnetic domains. Phys. Rev. Lett. **30**, 230–233 (1973).

[2] R. Tomasello, E. Martinez, R. Zivieri, L. Torres, M. Carpentieri, and G. Finocchio, A strategy for the design of skyrmion racetrack memories. Sci. Rep. **4**, 6784 (2014).

[3] L. Liu, C.-F. Pai, Y. Li, H. W. Tseng, D. C. Ralph, and R. A. Buhrman, Spin-torque switching with the giant spin Hall effect of Tantalum. Science **336**, 555–558 (2012).

[4] K. Everschor, M. Garst, R. A. Duine, and A. Rosch, Current-induced rotational torques in the skyrmion lattice phase of chiral magnets. Phys. Rev. B **84**, 064401 (2011).

[5] J. Sampaio, V. Cros, S. Rohart, A. Thiaville, and A. Fert, Nucleation, stability and current-induced motion of isolated magnetic skyrmions in nanostructures. Nat. Nanotechnol. **8**, 839–844 (2013).

[6] J. Iwasaki, W. Koshibae, and N. Nagaosa, Colossal spin transfer torque effect on skyrmion along the edge. Nano Lett. **14**, 4432–4437 (2014).